8-9-2014

SYNTHESIS, CHARACTERIZATION AND EVALUATION OF IR-BASED BIMETALLIC CATALYSTS

You Jung Song
University of South Carolina - Columbia

SYNTHESIS, CHARACTERIZATION AND EVALUATION OF IR-BASED BIMETALLIC CATALYSTS

by

You Jung Song

Bachelor of Engineering
Soongsil University, 2007

Master of Science
Soongsil University, 2009

Submitted in Partial Fulfillment of the Requirements

For the Degree of Doctor of Philosophy in

Chemical Engineering

College of Engineering and Computing

University of South Carolina

2014

Accepted by:

Christopher T. Williams, Major Professor

John R. Monnier, Committee Member

James A. Ritter, Committee Member

Donna A. Chen, Committee Member

Lacy Ford, Vice Provost and Dean of Graduate Studies

DEDICATION

This work is dedicated to my hudsband, who always helped and encouraged me thru my career giving me strengths and insight to achieve anything that I pursue…

사랑하는 남편에게 바칩니다.

ACKNOWLEDGEMENTS

First of all, I want to thank my advisor, Dr. Christopher T. Williams, for his unconditional assistance, advices and understanding through my doctoral research. He made my Ph.D. student life easier and more enjoyable, by not only helping me with his excellence guidance but also allowing me to attempt my own ideas. Thank you Dr. Williams, it has been very pleasure to work with you and now I can keep doing the research due to this delightful experience.

Special thanks to committee members, Dr. John R. Monnier, James A. Ritter, and Donna A. Chen, for sharing their knowledge and wisdom in catalysis as well as their insightful comments and suggestions during achievement of this work. You have contributions to this studty in a variety of ways.

I acknowledge the financial support provided to me during my PhD studies from Toyota Motor Engineering and Manufacturing North America, Inc. and National Science Foundation. I also acknowledge University of South Carolina Electron Microscopy Center for instrument use, scientific and technical assistance, especially the assistance of Dr. Douglas A. Blom. I also thank Dr. Shuguo Ma with XPS facility and his support. I am also most grateful to my group members, classmates, and Korean associate students.

I would like to express my sincere gratitude to my dear family, specially my mom, Youngki Goo, my dad, Jaeseok Song and my one and only sister, Yumi Song who never stop loving me and providing cares. They always have great faith in me no matter what I do so that I can pursue and obtain my goals in America even though such a long distance

separates us. In addition, I want to dedicate a special recognition to my very best friend or my hudsband, Sungtak Kim, for his unconditional love and for being always with me and support me since we first met 11 years ago. I admire his sacrifice that he came across the Pacific only for me when I was skeptically wondering the PhD life in South Carolina. He shared all my emotions encountered during this tough journey. Thank you Sungtak, you have assisted me in innumerable ways. Those a few words I write here cannot extent the value of his contribution. And last but not least I send gratitude separately to my son, Ryan (Hyunseung), for a little bundle of joy, energy and happiness he brought to our house that helped me to release and forget the stress of school at home.

ABSTRACT

This dissertation considers effective bimetallic preparation for supported Ir-based bimetallic catalysts and their catalytic activity. Since bimetallic catalysts exhibit significantly different catalytic and chemical properties than their corresponding monometallic components by providing enhanced selectivity, stability and /or activity, many monometallic catalysts in industrial processes have been replaced by bimetallic catalysts. However, conventional synthetic methods used to produce monometallic and bimetallic catalysts often result in wide particle size distributions and non-uniform materials which can be difficult to characterize on a fundamental level. Two alternate preparation methods, dendrimer templating and electroless deposition, are developed and compared with conventional incipient wetness method. In dendrimer templating method, poly(amidoamine) (PAMAM) dendrimers are used to form and stabilize cluster and nanoparticles in solution generating dendrimer metal nanocomposites (DMN) precursors. On the other hand, suitable reducing agent and metal ion source are selected for electroless deposition method which allows the ability to tailor the catalyst surface sites upon which the secondary metal is deposited. In the present work, the effectiveness of using two distinct method as well as conventional method to prepare Al_2O_3 supported Ir-Au, Ir-Ag catalysts is reported.

Ir-Au/Al_2O_3 catalysts were prepared utilizing the DMN approach by four different synthetic routes and allowed for comparison with the conventional counterparts. These

catalysts showed different metallic dispersions with various particle sizes and distributions, depending on the preparation method. These properties influence the catalytic performance, dendrimer-derived catalyst with higher dispersion and narrow particle size distribution resulted in enhanced activity toward CO oxidation and higher selectivity towards N_2O and a better intrinsic catalytic turnover frequency for reduction of NO by CO and NO decomposition.

On the other hand, a series of alumina supported Ag-Ir and Au-Ir bimetallic catalysts having controlled and incremental coverages of Ag or Au, have been successfully prepared in an optimized electroless deposition bath. The structural and electronic properties of the catalysts were characterized using hydrogen chemisorption, atomic absorption spectroscopy, Fourier transform infrared spectroscopy, and X-ray photoelectron spectroscopy. The results suggest that Ag and Au metal was deposited on all types of Ir surface sites in a non-discriminatory fashion. However, kinetic studies of CO oxidation revealed different result for Ag-Ir and Au-Ir bimetallic system. That is, higher coverages of Au resulted in lower turnover frequencies (TOFs) indicating that no bimetallic effect between Au and Ir for this reaction. In contrast, the highest TOF was obtained at the half point in Ag-Ir bimetallic catalysts where the Ir-Ag pair sites are maximized. This clearly suggests a bifunctional effect, where the Ag provides a non-competitive source of adsorbed oxygen for reaction with CO adsorbed on Ir. Consistent reaction order studies were obtained. On the other hand, enhanced catalytic activities were found toward NO-CO reaction over both ED-derived bimetallic Au-Ir as well as Ag-Ir catalysts. This can be explained by a probable bifunctional effect, but more kinetic studies need to be done to fully understand the mechanism for this.

TABLE OF CONTENTS

LIST OF TABLES

LIST OF FIGURES

LIST OF SYMBOLS

C=C double bonds between two carbons

$\overline{D}$ D_{VSMD}, volume-surface mean diameter, measured by STEM

D_{ave} average diameter from STEM

D_{Ir} Iridium dispersion

$D_{p,i}$ measured diameter from STEM images

D_{VSMD} volume-surface mean diameter, measured by STEM

e electrons

E_a activation energy

θ_{Ag} coverages of Ag

θ_{Au} coverages of Au

$\theta_{expt'l}$ experimental metal coverage, determined from chemisorption analysis

θ_{mono} theoretical monodisperse metal coverage

$\theta_{CO(Ag)}$ coverage of CO molecule on Ag

$\theta_{O(Ag)}$ coverage of atomic oxygen on Ag

$\theta_{CO(Ir)}$ coverage of CO molecule on Ir

$\theta_{O(Ir)}$ coverage of atomic oxygen on Ir

K ratio of adsorption and desorption rate

k reaction rate constant

M any of the viable ED metals

N_i number of particles

ν_{CO}	characteristic CO vibration, measured from FTIR
ν_{NO}	characteristic NO vibration, measured from FTIR
P_{CO}	pressure of CO
P_{O2}	pressure of O_2
R	reducing agent
r_{CO_2}	reaction rate of CO_2 formation
T_{50}	temperature at 50% CO conversion
wt.%	percentages of metal weight, obtained by elemental analysis
z	valence

List of Abbreviations

AA ..... Atomic Absorption

AAS ..... Atomic Absorption Spectroscopy

BE ..... Binding energy

CD ..... Conventional-derived

DD ..... Dendrimer-derived

DFT ..... Density functional theory

DMAB ..... Dimethylamine borane

DMN ..... Dendrimer-Metal Nanocomposite

ED ..... Electroless Deposition

E-R mechanism ..... Eley-Rideal mechanism

EDS ..... Energy Dispersive Spectroscopy

EPR ..... Electron Paramagnetic Resonance

FT-IR ..... Fourier Transform Infra-Red Spectroscopy

FWHM ..... Full width at half maximum

G4OH ..... Fourth generation hydroxyl-terminated poly(amido)amine dendrimer

G4-NH_2 ..... Generation four amine-terminated

G5-OH ..... Generation five hydroxyl-terminated

HAADF ..... High angle annular dark-field

IW ..... Incipient Wetness

L-H formalism ..... Langmuir-Hinshelwood formalism

MCT-B ..... Mercury-cadmium-telluride B

ML ..... Monolayer

MS ..... Mass spectrometer

PAMAM dendrimer ..... Poly-(amidoamine) dendrimer

PPI dendrimer ..... Poly(iminopropane-1,3-diyl) dendrimer

PROX ..... Preferential oxidation of CO

PZC ..... Point of zero charge

RA ..... Reducing Agent

Redox ..... Reduction-oxidation

RT ..... Room temperature

SBD ..... Starburst dendrimer

SEA ..... Strong electrostatic adsorption

STEM ..... Scanning transmission electron microscopy

TOFs ..... Turnover frequencies

TPD ..... Temperature-programmed desorption

UHP ..... Ultra high pressure

UHV ..... Ultra high vacuum

VSMD ..... Volume-surface mean diameter

XANES ..... X-ray Absorption Near Edge Structure

XPS ..... X-ray photoelectron spectroscopy

XRD ..... X-ray Diffraction

CHAPTER 1

INTRODUCTION

1.1 OVERVIEW

Heterogeneous catalysis is critical to chemical technology, facilitating innumerable chemical reactions. During the catalytic process, chemical bonds are broken and new chemical bonds are formed repeatedly, usually without a significant change of the catalyst. In the absence of the catalyst, this chemical transformation would either not occur or would take place with lower efficiencies or slower rates. Therefore, many catalysis researchers have been committed to the development and improvement of heterogeneous catalysts for hydrogenation, dehydrogenation, isomerization, and polymerization reactions. These catalytic reactions all played a key role in the development of the industrial revolution and have impacted our society and lifestyle over the past several decades. As we live in the 21st century, we would have difficulty imagining our world without the fruits of heterogeneous catalysis, because it has an impact on nearly every part of our daily lives, ranging from the production of gasoline to pharmaceuticals to plastics [1, 2]. The needs for better catalysts will only increase as environmental and economic concerns motivate the development of more efficient processes.

Among heterogeneous catalysts, transition metals are widely used since they possess unique properties that enhance activity and selectivity in chemical reactions. Such metals are usually maintained on a support, which is normally a high surface area material such as alumina, silica or carbon. Consequently, the support provides a very large area over which the expensive metal can be distributed, thus allowing maximum exposure of the active metal surface. In industry, these supported catalysts are often prepared either by wet impregnation or incipient wetness impregnation methods. However, these conventional synthetic techniques do not effectively control the distribution or homogeneity of metals on the substrate in many cases. In addition to less than optimal performance, such non-uniform materials can also be difficult to characterize [3]. One goal in catalyst synthesis, therefore, is to exert more control over delivery of metal nanoparticles to supports. In order to obtain uniform materials, a variety of synthetic techniques have been developed over the years, including the use of ion exchange method [4], colloidal routs with various stabilizers [5] or organometallic cluster complexes [6], to name a few. One very promising synthetic method that has been explored recently is the use dendrimer-metal nanocomposite (DMN) precursors on route to supported metal catalysts [7]. This relatively new approach is interesting due to the possibility to control resulting metal particle size and composition. As another alternate electroless deposition (ED) method, which is based on a well established method of coating films, is also intriguing. As compared to traditional methods such as impregnation, vacuum deposition, and sputtering, ED may be an attractive future commercial synthesis technique that provides with its simplicity of operation and better control.

Supported Ir catalysts are outstanding candidates for a variety of catalytic reactions due to their stability, activity and selectivity under reaction conditions [8-11]. For example, Ir catalyst have been shown to be capable of stereo selective hydrogenation of C=C bonds [12]. Nevertheless, compared to other platinum group metals, Ir metal has been less explored although it is situated among the same 5f orbital metals as Pt. In addition, there is very little information about supported Ir catalyst synthesis using the DMN approach or ED method. In this study, it is proposed to study synthesis and characterization of dendrimer-derived and electrolessly-deposited Ir mono- and bi-metallic catalysts as opposed to conventionally-derived one. Thus, a family of dendrimer-derived or electrolessly-deposited Ir-based catalysts has been prepared to illustrate synthetic method effects on bimetallic structure and correlate physical and/or chemical properties of the bimetallic catalysts with their kinetic behavior for NO reduction and CO oxidation and direct NO decomposition.

1.2 BACKGROUND AND LITERATURE REVIEW

1.2.1 PREPARATION OF BIMETALLIC CATALYSTS

In the 1940's, scientists began to experiment with the combination of various metals in one catalytic system [13]. These poly-metallic catalysts have been implemented industrially and have had major impact on petroleum refining. Generally, research has shown that bimetallic catalysts exhibit significantly different catalytic and chemical properties than their corresponding monometallic components by providing enhanced selectivity, stability and /or activity [14, 15]. Owing to these desirable attributes, many

monometallic catalysts in industrial processes have been replaced by bimetallic or poly-metallic catalysts [14, 15].

Many different methodologies have been developed to prepare bimetallic catalysts. Two of the most widely used industrial procedures are successive impregnation of different metal salts (two metal salts are successively deposited), and coimpregnation (two metal salts are simultaneously deposited) followed by reduction on the support. Unfortunately, these methods typically result in the formation of both monometallic particles of each of the two metals, and bimetallic catalyst particles of varying compositions of the two metallic components [4]. This complex mixture usually brings not only poor catalytic performance but it also makes any correlations between catalyst activity, catalyst characterization, and catalyst composition virtually impossible. Thus, an alternate method of preparation is required.

One alternative is the ion exchange method for preparation of zeolite supported metals, which rely on support influences and properties to control metal placement. The framework of zeolite contains an Al^{3+} atom surrounded by four oxygen atoms, which result in an excess negative charge that is neutralized by cations such as Na^{+}. In this ion exchange method the cations associated with the Al groups are exchanged for ligated metallic ions such as $[Pt(NH_3)_4]^{2+}$, for example. The exchanged material is then calcined to remove the ligands (NH_3), and finally the material is exposed to flowing hydrogen for metal reduction. This procedure has been used for the preparation of bimetallic Ag-Pt catalysts where the Pt/NaY zeolites were prepared and exposed to a room temperature, aqueous solution containing $AgNO_3$, which was ion exchanged to yield the final bimetallic catalyst [4]. Successive ion exchange of a second metal salt solution is used to

introduce the second metallic component of the bimetallic system and the bimetallic catalysts prepared in this manner have shown promising results and have been implemented in several industrial processes [4]. However, this methodology does not guarantee that the two metals will be intimately associated with each other. In addition, the calcinations step may induce several undesired effects such as autoreduction, which can cause particle agglomeration [4].

Several other preparation methods have been developed whereby the metal placement is more precisely controlled. Many of these methods are based on the use of colloids, which are suspended solids, because their small size and high dispersion provide notable advantages. However, it is necessary to stabilize the suspension to prevent the undesired agglomeration of these unstable nanoparticles. This may be done using electrostatic and/or steric stabilizers or ligands. Once the stabilized, a dispersed suspension is attained, and the metal particles can be reduced by various methods including chemical reduction, thermal decomposition, and electrochemical methods. To convert to a more conventional, heterogeneous format for metallic catalysts, the metal particles are often deposited on a support using impregnation or grafting, although the deposition process often results in a less active catalytic material [5]. The preparation of bimetallic catalysts via colloidal methodologies proceeds in the same manner wherein the metals may be reduced simultaneously or successively. Unfortunately this preparation method has sometimes resulted in suspensions having particles larger than 10nm and irreproducible catalytic properties.

Organometallic precursors have also been investigated for their ability to simultaneously act as a template and a stabilizing agent for nanoparticles. In principle,

they allow clusters to be supported while maintaining their metal-metal bond. First, the organometallic precursor, which contains the desired metals, is contacted with a given support. This supported monometallic cluster can then be exposed to another cluster containing the secondary metal. By proper selection of ligands, it is possible to have direct interaction between the two clusters, leading, in principle, to the formation of a bimetallic catalyst after the ligands are removed by various thermal treatments. Although these methods do provide metal precursors with defined structures and stoichiometries, the deposition process and thermal removal of ligands may cause the metals to segregate and lose the intimate contact desired in the preparation of bimetallic catalysts. Additionally, organometallic derived catalysts often lose their high dispersion under reaction conditions due to the unstable nature of the particles. Thus, the catalysts prepared from bimetallic clusters do not offer obvious advantages in application [6]. Nevertheless, it was noted that these materials are still very probative from an academic perspective [6].

Metal species may also be stabilized and templated using dendrimers. Dendrimers [16] are monodisperse, hyperbranched spherical organic macromolecules that emanate from a central core with repetitive branching units, allowing for controllable size. While possessing a very dense exterior, they contain less dense interiors that can be ideal for encapsulation of metal nanoparticles. One of the most successful applications along these lines has been the synthesis of metal nanoparticles using poly-(amidoamine) (PAMAM) dendrimers. Originally pioneered by Crooks et al. [17], the approach takes advantage of the fact that transition metal ions (e.g., Pt^{2+}, Pd^{2+}, Cu^{2+}) can coordinate with the interior tertiary amine and secondary amide functional groups of the dendrimer. The interior void spaces are then used for stabilization and creation of metal clusters or nanoparticles upon

reduction treatment. These dendrimer-metal nanocomposites (DMNs) are stable for extended periods of time and can exhibit interesting catalytic properties [18]. The dendrimer can exert control over size and (in the case of multiple metal ions) composition of resulting nanoparticles or clusters, which can allow for tuning of catalytic properties.

Unfortunately this method does not work well for ions such as Ag^+ which only weakly complex to the dendrimer. As such, metal-displacement methodologies have been developed in which Cu nanoparticles are deposited via direct reduction and then exposed to Ag^+. Due to its more positive half-reaction, Ag^+ oxidizes the Cu and becomes reduced. By altering the pH or the Ag^+ concentration and allowing some of the Cu to remain in its reduced form, bimetallic dendrimer encapsulated nanoparticles can be formulated [18]. A similar method has been used for the preparation of Au-Pt nanoparticles. In this case the Cu encapsulated nanoparticles were prepared via direct reduction using G5-OH PAMAM (generation five hydroxyl-terminated poly(amidoamine)) dendrimers. The dendrimer-encapsulated Cu nanoparticles were then exposed to a solution of K_2PtCl_4 and $HAuCl_4$, which oxidized the Cu and resulted in small "intimately mixed" bimetallic Pt-Au nanparticles [19]. There are now many investigations exploring the use of DMNs as precursors to synthesize supported catalysts, and narrow metal particle size distributions have been observed for different transition metals such as Pt [20-25], Pd [25], Au [19, 26], Ru [27, 28], Pt-Au [19], and Pd-Au [26] catalysts.

Recently, another series of preparation methods based on reduction-oxidation (redox) reactions have neen developed to prepare bimetallic catalysts. Unlike the other techniques previously described, these methods rely on redox chemical reactions to control the placement of the secondary metal. Consequently, there is no need to remove

excess materials through calcination or heat treatments. Furthermore, the redox methodologies hold a great deal of promise since they allow the ability to tailor the sites upon which the secondary metal is deposited [4]. In the catalytic reduction methodologies, such as electroless deposition (ED), the primary metal activates a reducing agent, which then reduces the secondary metal from solution. Different reducing agents may be used, although the choice of reducing agent influences the type of sites upon which the second metal will be deposited. Thus, this process also provides a means of tuning the catalyst so that certain sites can be selectively blocked. This scheme will be discussed in detail in section 1.2.3.

1.2.2 Dendrimer-Metal Nanocomposites (DMN) for Catalyst Synthesis

For a number of reasons, metal nanoparticles synthesized by the dendrimer route have great potential to be used as catalysts. First, dendrimers can exert control over the size and composition of metal particles (in the case of multiple metal ions) by choosing the proper generation of dendrimer solution and mixing it with suitable amounts of metal ion solutions. Second, dendrimers can prevent the metal nanoparticles from agglomeration, which leads to larger particles and lower metal surface area. However, it is important that the polymer does not passivate the catalytic sites, thus allowing the reactive substrates to penetrate through the dendrimer and access the metal surfaces. Finally, in the case of heterogeneous catalysis, dendrimer can be a useful delivery device for immobilizing metal nanoparticles onto various supports. Therefore it is not surprising that several studies in recent years have examined the utility of these materials for catalysis.

1.2.2.1 Dendrimer Description

The concept of a dendritic molecule was first proposed about 30 years ago, but only until recently is there more and more interest in their applications [16, 29]. These hyper-branched, monodisperse, spherical organic materials have three common geographical features: a core, repetitive branches and terminal groups. These features make the dendrimer a very versatile material since structure and chemical properties of dendrimer can be controlled through their variation. For example, dendrimers terminated with hydrophilic functional groups are soluble in polar solvents such as water and low-molecular-weight alcohols [30]. The density of the external functional groups increases with generation, allowing control of access to dendrimer interiors [31]. The divergent and convergent approaches are two ways to synthesize dendrimers. In the former method, the growth of dendrimer comes from the core to the exterior, including a serial repetition of chemical reactions as shown in Figure 1.1.

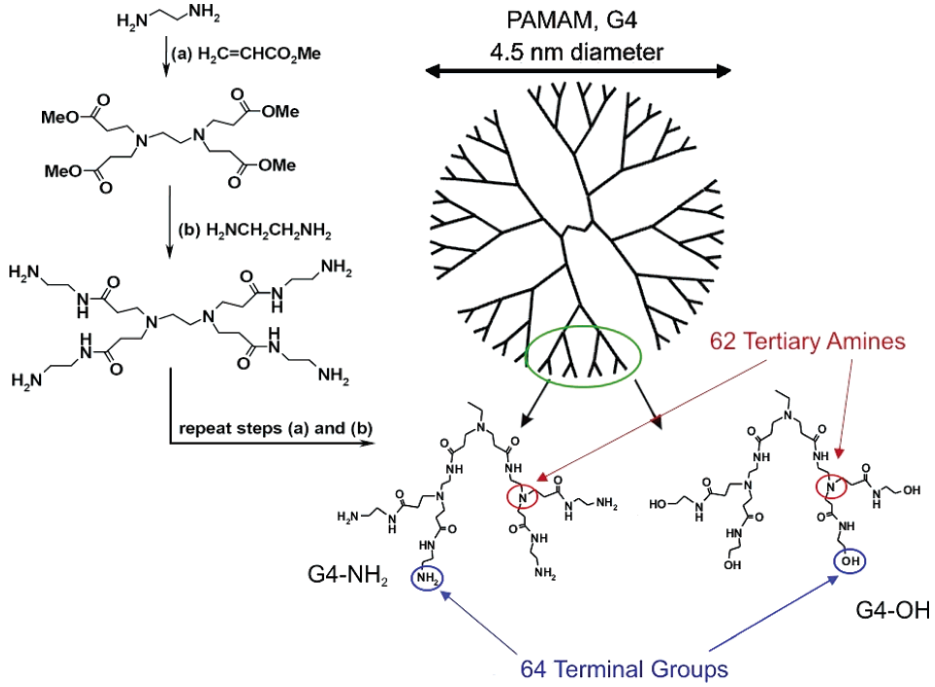

Figure 1.1 Amine-terminated PAMAM dendrimer synthesis [31]

Different terminal groups can be introduced onto the dendrimer outer shell by using different monomers in the last synthesis step or by modifying the terminal groups of primary amine terminal groups [31]. The latter method builds from the periphery to the core. This involves a cycle reaction as well, but in this case each step is used to synthesize individual dendrimer branches (dendrons). So far, fewer materials have been successfully synthesized using the convergent method, and very high generation dendrimers (>10) cannot be made this way. Two of the most successful products from the divergent approach are poly(amidoamine) (PAMAM) and poly(iminopropane-1,3-diyl) (PPI) dendrimers. Table 1.1 contains physical characteristics of PAMAM dendrimers as a function of generation. The exterior of a high (≥4) generation dendrimer is very dense while its interior is relatively hollow and the size, density, and number of functional groups of dendrimers depend only on the generation. Hydroxyl-terminated poly(amidoamine) (PAMAM-OH) dendrimers have polar tertiary amines and secondary amides in their interior. This type of dendrimer has been used because pH control is not as necessary (as it is for amine terminated dendrimer), allowing metal ions to complex in

Table 1.1 Physical characteristics of PAMAM dendrimers [31]

Generation	number of surface groups	number of tertiary amines	molecular weight		diameter[a] (nm)
			NH_2 terminal group	OH terminal group	
0	4	2	517	521	1.5
1	8	6	1430	1438	2.2
2	16	14	3256	3272	2.9
3	32	30	6909	6940	3.6
4	64	62	14215	14277	4.5
5	128	126	28826	28951	5.4
6	256	254	58048	58298	6.7
7	512	510	116493	116993	8.1
8	1024	1022	233383	234382	9.7

[a] Molecular dimensions determined by size exclusion chromatography.

their interiors [31].

1.2.2.2 MONOMETALLIC DMNS

Dendrimers can be used as host molecules, with the interior hollow pocket serving as containers that can hold metal and semiconductor nanoparticles. The possibility of encapsulating guest molecules in dendrimer hosts was first discovered by Maciejewski in 1982 [32], and has developed as the major application of dendrimers ever since. In one of the earliest investigations of dendrimer-metal interactions, Ottaviani et al. [33] studied copper and manganese complexation with full generation poly(amidoamines) starburst dendrimer (SBD) using electron paramagnetic resonance (EPR) spectroscopy. The complexation studies were carried out with Cu^{2+} and Mn (II) as function of temperature, pH, dendrimer generation and aging of the samples. They found at pH greater than 3.5, surface amino groups of SBDs prevented interaction with Mn(II), but allowed Cu^{2+} complexation. When pH values were between 4 and 5, Cu^{2+} ions were found to be coordinated to two surface NH_2 groups and two internal NR_3 groups, giving Cu coordinated to 4 Nitrogen ($Cu\text{-}N_4$). The complexes showed higher mobility at higher pH, with Cu^{2+} moving to the interiors of the SBDs structures. These interactions between dendrimer and copper metal ions were quite strong and stable so that the complete decomposition of SBDs was found after 60 days of preparation for pH >5.5.

The concept of the template-synthesis strategy to prepare metal nanoclusters within the dendrimers was successfully proved by Crooks and co-workers [34]. They prepared different size Cu clusters by encapsulating Cu^{2+} into the interior of PAMAM starburst dendrimer by reduction. The Cu clusters were found to be stable when they are inside the dendrimer, despite their small sizes of less than 1.8 nm. They reported that

Cu^{2+} bonding with dendrimer is pH dependent as well, because H^+ and Cu^{2+} compete for tertiary amines sites. One of their major findings was that the ability to prepare metal nanoclusters inside the dendrimer strongly depends on the chemical composition of the dendrimer.

They also synthesized noble metal nanoparticles such as Pt and Pd with high monodispersity and controlled size using PAMAM dendrimer [35, 36]. As shown Figure 1.2, the synthesis process is very straightforward. After preloading proper metal ions into a dendrimer template by mixing them together and stirred for an extended period of time, and then chemically reducing them, the dendrimer-encapsulated metal nanoparticles are formed. These metal nanoparticles can be used as catalysts with or without the presence of dendrimer templates. Hydroxyl-terminated PAMAM dendrimers are found to prevent agglomeration of the nanoclustes since they are confined within the interior. Pt particles had roughly spherical shape with an average diameter of 1.6 nm (G4-OH(Pt_{60})) and 1.4 nm (G4-OH(Pt_{40})) depending on the metal to dendrimer ratio. They found that clusters size is related to the dendrimer generation and the number of ions preloaded into the

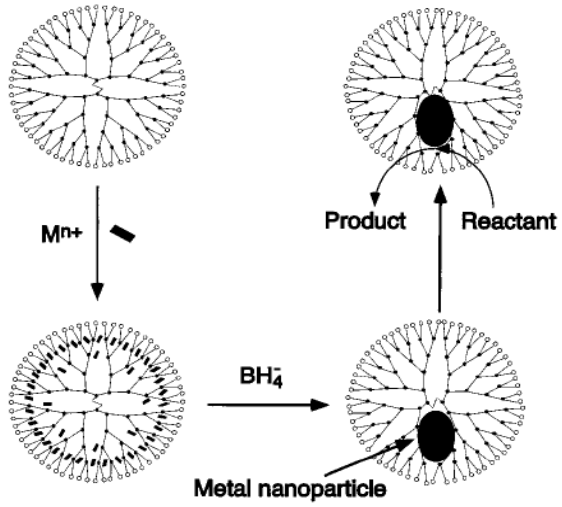

Figure 1.2 Synthesis route for dendrimer-encapsulated metal nanoparticles [18]

dendrimer interior prior to reduction.

For the transition metal ions that cannot coordinate with the interior amine groups of dendrimers (e.g. Ag^{+}) via either covalent bonds or by forming strong complexes, an alternative way was proposed by Crooks and co-workers. These displacement reactions were accomplished by in-situ exchange resulting from differences in electrochemical potentials [37]. The more noble metal ions can be reduced to form metal nanoparticles through an intra-dendrimer exchange reaction. This concept was applied to obtain Pt, Pd, Ag, and Au nanoparticles using Cu^{2+} as the first displaced ion since the standard potential for their half-reactions are more positive than Cu^{2+}/Cu. Ag nanoparticles were obtained by primary displacement of Cu nanoparticles, but Au, Pt, and Pd were obtained either by primary or secondary displacement as shown in Figure 1.3.

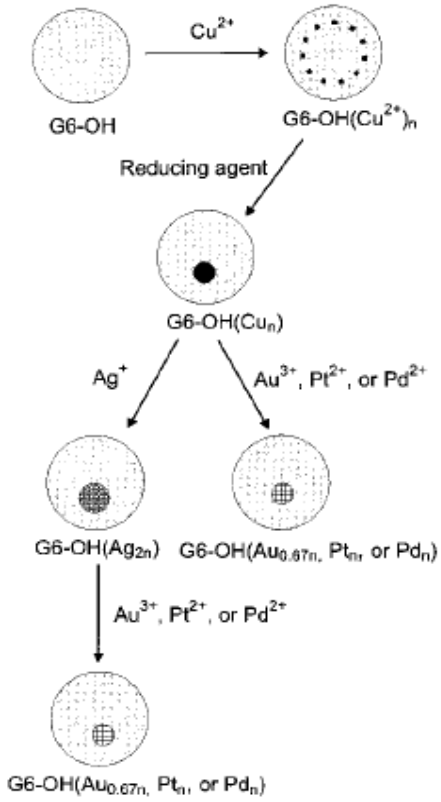

Figure 1.3 Scheme for displacement reactions [37]

There are some other groups who used similar ways to synthesize dendrimer-encapsulated metal nanoparticles. Theoretically, by changing the generation of dendrimer, the terminal function groups, the kids of metal ion, and the dendrimer/metal ion ratio, almost any kind of dendrimer-encapsulated metal nanoparticles can be synthesized. Balogh et al. prepared Cu nanoclusters by mixing PAMAM G4 and copper (II) acetate solution together, followed by reduction with aqueous hydrazine solution [38]. The copper domains dispersed within dendrimer were confirmed by UV-vis spectroscopy and the estimated Cu nanoclusters were much smaller than the dendrimer. Esumi and co-workers synthesized Pt nanoparticles in ethyl acetate solvent using different generations of PAMAM dendrimer with methyl ester terminal groups [39]. The characterization was carried out using FT-IR and UV-vis spectroscopies to investigate the interaction between Pt^{2+} ions and dendrimers and it was found that a ligand substitution reaction occurred from Cl^- to oxygen or nitrogen of the dendrimer. They also investigated interaction between Au and PAMAM dendrimers of different generations (G0-G5) with using UV-irradiation method to reduce Au^{3+} ions [40]. With increasing irradiation time, the existence of Au colloids was observed. Manna et al. [41] reported size-controlled Ag and Au nanoparticles with PAMAM G4 by using the same procedure of displacement reactions that Crooks group used.

1.2.2.3 BIMETALLIC DMNS

From the catalytic point of view, bimetallic nanoparticles are very attractive because they possess unique properties that are rather different from those of the

individual metals. Addition of a second metal is commonly used to improve the catalytic activity and/or selectivity of a certain reaction. In order to achieve bimetallic dendrimer-metal nanocomposites, three different synthetic methods can be used as shown in Figure 1.4 [17, 18].

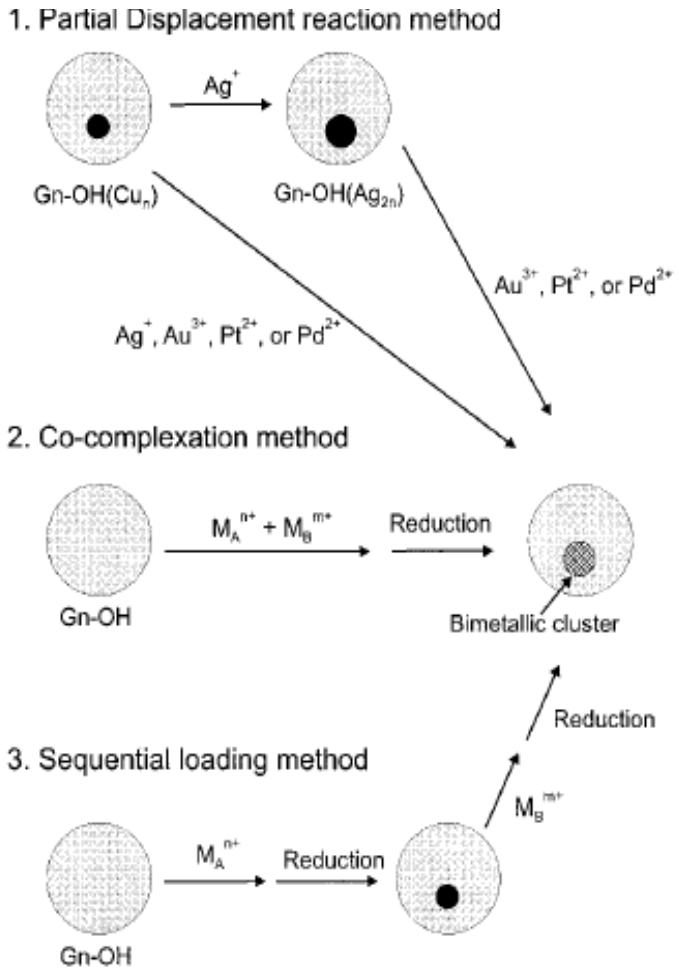

Figure 1.4 Dendrimer-encapsulated bimetallic nanoparticles [18]

The first tactic is the preparation of mixed-metal intradendrimer nanoparticles by partial displacement. This is accomplished following the total displacement reactions as the Crooks group proposed. However, in this case, less than stoichiometric amount of the

second metal is used in order to have partial replacement of the first. This is different from the other two techniques that the metals were added in stoichiometric quantity to complex fully with a particular dendrimer generation to obtain monometallic particles. The second approach is co-complexation of two different metal ions. In this method, two different metals ions are added to a dendrimer solution simultaneously followed by a single step of reduction. Lastly, bimetallic nanoparticles can also be obtained by the sequential loading method, in which single metal ions are added to a dendrimer solution one after the other separated by a step. In principle, these three methods for preparing bimetallic nanoparticles could be applied to also prepare trimetallics, although this has not been proved.

Although there are less reports showing the DMN approach for bimetallic nanoparticle preparation compared to those for monometallic DMNs, Crooks et al. [17, 18] have successfully prepared Pt-Pd DMN bimetallic nanoparticles using both the co-complexation and sequential methods. They used two different solutions of $PtCl_4^{2-}$ and $PdCl_4^{2-}$, and mixed them together with G6-OH followed by a single reduction step for the co-complexation method. This process was characterized via UV-Vis spectroscopy, where the complex mixture spectrum was the sum of the G6-OH/ $PtCl_4^{2-}$ and G6-OH /$PdCl_4^{2-}$ spectra. For the case of sequential method, the size of metal nanoparticles was examined by TEM during each step. It was found that an average particle diameter of Pt (G6-OH(Pt_{55})) that was reduced first exhibited 1.4 ± 0.2 nm. After subsequent addition of Pd followed by reduction yielded a final bimetallic particles size of 3.0 ± 1.0 nm. This was attributed to interdendrimer transfer of Pd atoms during the second reduction. They further investigated those Pd-Pt bimetallic catalysts via co-complexation approach using

PAMAM G4-OH dendrimer [42]. The total metal-to-dendrimer molar ratio was held at 40:1(e.g. G4-OH(Pd_x-Pt_{40-x}), where x varied from 0 to 40. TEM and X-ray energy dispersive spectroscopy (EDS) confirmed that bimetallic particles were present instead of physical mixture on monometallic particles. For DMNs containing 75% Pd and 25% Pt, the particles size were found to be 1.9 ± 0.4 nm and 2.1±0.6 nm in bright-field and high-angular dark-field mode of high resolution TEM, respectively. The effect of Pd-to-Pt molar ratio was examined for hydrogenation of allyl alcohol in water, where the turnover frequency was correlated to the molar ratios. The results suggest that this method can efficiently prepare monodisperse bimetallic catalyst under controllable conditions. Furthermore, they also synthesized and characterized other bimetallic dendrimer encapsulated particles such as Pd-Au [7].

Several different bimetallic DMNs were synthesized by some other groups. For instance, Chung and Rhee have synthesized and characterized Pd-Rh [43], Pd-Ag [44], and Pt-Pd [45] bimetallic DMNs. The first two bimetallics were prepared by co-complexation of the dendrimer-salt solutions, while Pd-Ag bimetallic DMNs were prepared mixing dendrimer with silver(I) bis(oxalate)palladate(II) complex to solve the intrinsic problems of the Pd-Ag system [44].

The use of dendrimer-encapsulated approach has also been used to prepare different combination of supported heterogeneous bimetallic catalysts. The Chandler group [19] has prepared supported bimetallic Pt-Au nanoparticles via the partial displacement reaction method as explained above. They found from TEM and EDS results that this preparation method yields intimately mixed bimetallic nanoparticles smaller than 3 nm. Scott et al. [26, 46] prepared titania supported Pd-Au bimetallic

catalyst via both co-complexation and sequential method. It was noticed that the metals can be placed in a core or shell position by using sequential loading method depending on the loading order. On the other hand, the co-complexation method is more likely to produce nanoscale metal alloys. They also found that this Pd-Au supported on titania catalyst exhibited a synergetic catalytic effect toward CO oxidation compared to supported monometallic catalysts.

Liu et al. [47] studied a series of silica-supported monometallic (Pt, Ru) and bimetallic (PtRu) catalysts that synthesized using both dendrimer–metal nanocomposites (DMNs) and metal salt precursors. Histograms obtained from electron microscopy reveal that the dendrimer-mediated synthesis yields smaller particle sizes and narrower particle size distributions compared with the conventional incipient wetness impregnation for the monometallic Ru and Pt–Ru. In addition, XRD patterns suggest that the co-complexation sample has the highest Ru content (33%) in its alloy phase, while conventional PtRu has the least Ru content (12%) in its alloy phase. In concert with these findings, O_2–H_2 titration shows that the cocomplexation catalyst has a relatively Ru-enriched surface, while conventional PtRu has a Pt-enriched surface.

Xie et al. [48] also investigated similar study with Pt-Cu DMNs. STEM analysis suggests that the G4OH dendrimer was capable of exerting significant control over particle formation and sintering on the catalyst support. Consequently, the sizes of the Pt and Pt–Cu nanoparticles in these catalysts indicate a smaller average particle size and narrower size distribution for the metal nanoparticles in the DD catalysts than in the CD catalysts. They also found that the differences in the IR spectra which can be related to

differences in the oxidation state, particle size, and relative Pt/Cu composition of the catalysts.

1.2.3 Electroless Deposition (ED) for Catalysts Synthesis

Electroless deposition (ED) became an industrial process after Brenner and Riddell's accidental discovery in 1946 of a stable ED solution that led to smooth, hard nickel deposits [49, 50]. Brenner and Riddell named the process 'electroless deposition' which is essentially an autocatalytic process whereby metal is deposited without the use of an external electrical current [49]. Unlike displacement and contact deposition, autocatalytic deposition allows deposition to continue after the primary metal is covered. Consequently, autocatalytic deposition can be used to formulate very thick coatings that generally exhibit desirable electrochemical properties such as low porosity and increased hardness [51]. One of the most appealing aspects of ED is the wide variety of metals that can be deposited. In fact, any metal that can be deposited using electrodeposition (use of an external current to promote reduction) can also be deposited via ED given the proper deposition conditions [49]. As a result, ED has been developed for a wide variety of metals including most Group VIII metal as well as Ag, Au, Cu, Cd, Cr, Sb, Sb, In, etc [52]. Furthermore, ED provides the ability to deposit this wide variety of metals on conductive, semi-conductive, and non-conductive materials, whereas electrodeposition is only practical on conductive materials [51, 53]. Initially, electoless deposition was used to provide coatings for decorative purposes, but with development of modern technologies, other innovative uses have been found [54]. In fact, materials formulated by ED have applications in the electronics, aerospace, and battery industries [49, 53].

Additionally, the “selective” nature of ED makes it appealing for the preparation of heterogeneous catalysts, since it could potentially lead to the production of large volumes of highly dispersed, supported bimetallic catalysts at relatively low costs.

1.2.3.1 ED BATH

As a promising candidate method for synthesis of bimetallic catalysts, fundamental understanding of the chemistry and physics of the ED method is quite important. To understand deposition kinetics, it is good to discuss the experimental parameters that usually describe the solution (often called the ED bath) in which deposition takes place.The bath is usually aqueous and is generally composed of a metal ion source, a reducing agent, a complexing agent, a stabilizing agent, and possibly an accelerant [53]. In order for catalytic electroless deposition to be achieved, a delicate balance must exist between these components such that a kinetically stable bath is attained. Otherwise, rather than depositing the metal at active catalytic sites, the metal will simply be thermally reduced and will precipitate from solution [49].

Metal source: The metal source is a basic ingredient for formulation of an electroless bath. It should be soluble in order to provide stable bath configurations. The nature of metal complex used will directly affect the quality of both deposition and deposit. A wide variety of metal sources (e.g., sulfates, phosphites, chlorides, cyanides, nitrates, acetates) are available. In addition to deposition characteristics and bath environment, the effect of impurities and by products on the final deposit plays a key role in metal source selection. Generally, chloride precursors are safe; however, they are very sensitive to bath

parameters such as pH of solution, reducing agent and activity of the substrate. In addition, chloride baths are capable of inducing corrosion on aluminium or ferrous substrates, which may lead to substrate dissolution. Moreover, residual chloride ions are often not desired in catalysis applications. In contrast, cyanide metal sources are well known to provide more stable electroless baths, although their toxic nature hinders extensive use in industry. The potential metal sources used for electroless plating of several metals are described in Table 1.2. The metal precursor will undergo various transformations during electroless deposition such as complexation and hydrolysis. For example the kinetics of nickel deposition is mainly dependent on the metal ion complexion process in aqueous solution. Hexaaquonickel ion $[Ni(H_2O)_4(OH)_2]^0$ forms from Ni^{+2} in a reversible process dependent on the concentration of metal ion and pH of the solution. So, a clear understanding of metal source and its aqueous phase complexation processes helps in choosing a suitable metal precursor to formulate a stable electroless system.

Table 1.2 Metal precursors for different metals [53]

Metal	Metal sources
Ag	$AgNO_3$, $KAg(CN)_2$, $NaAg(CN)_2$
Au	$HAuCl_4$, $KAu(CN)_2$, $Na_3Au(SO_3)_2$
Co	$CoSO_4$, $CoCl_2$
Ni	$NiSO_4$, $NiCl_2$, $Ni(H_2PO_2)_2$, $Ni(CH_3COO)_2$
Pd	$PdCl_2$, $Pd(NH_3)_4Cl_2$
Pt	$Na_2Pt(OH)_6$, $(NH_3)_2Pt(NO_2)_2$, H_2PtCl_6

Reducing agent: The reducing agent donates electrons to the metal that is being reduced. Typical reducing agents for ED include hypophosphite, formaldehyde, alkali borohydrides, dialkylamine borane, and hydrazine [55]. There are several factors that

influence which reducing agent is chosen. In order for the process to be catalytic, the standard redox potential of the reducing agent must be more negative than that of the metal that is being reduced. For example, sodium bypophosphite is a practical reducing agent for nickel since its redox potential is -0.5V while that of nickel is only -0.25V [53]. Furthermore, the order of reducing agent activation on metals should be considered for synthesis of true bimetallic catlysts. In other words, the reducing agent should prefer to activate on the primary metal rather than the second metal or substrate, so as to produce a bimetallic surface. Ohno et al [55] measured the catalytic activity of different metals (Au, Pt, Pd, Ag, Ni, Co and Cu) for commonly used reducing agents. The anodic potentials of these metals at constant current density for each reducing agent are compared. Figure 1.5 shows the order of reducing agent activation on metals for anodic reduction in electroless plating and these trends are very useful to formulate different electroless baths. For instance, hydrazine and borohydride are better choices for electroless gold or silver deposition on Pt, where as DMAB and formaldehyde are recommended for Pt deposition on Au.

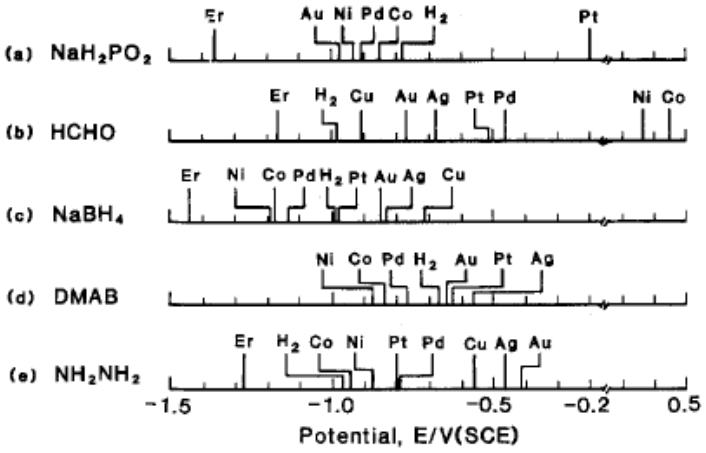

Figure 1.5 Catalytic activity of metals for anodic oxidation of different reactants, where Er: Oxidation-reduction potentials of reducing agents. [55]

Although the above chart recommends certain reducing agents for different combinations of metals, the overall ED kinetics of metals can also depend on the nobility of the metal and its resistance to both dissolution in the electroless bath, and excessive oxidation.

Bath Medium: An aqueous medium is preferred for most of the electroless deposition processes due to the availability of OH^- and H^+ ions that facilitate the electron exchange or transfer. Moreover, the aqueous medium affects the overall charge on the supports used such as in the case of alumina and silica, where a neutral support acquires different charge according to solution pH. The pH can easily be controlled in aqueous media, and so is a critical parameter to control electroless deposition processes. The other important parameter is the solubility of the metal complex, which greatly influences the stability of the electroless bath. Aqueous baths are suitable for most of the metal precursors used for electroless deposition of various metals.

Supported monometallic catalyst: Electroless deposition is possible on metallic and non metallic substrates. Typically, a monometallic supported catalyst is used as substrate for synthesis of bimetallic supported catalysts. The metal – support interactions of the primary monometallic catalyst are very vital for successful deposition of secondary metal. Because some electroless baths are run at temperatures near to 100 ℃ and highly acidic or basic environments, the support should hold the primary metal strong enough in such harsh conditions.

Additives: An electroless bath can be improved by introducing various agents that enhance the bath lifetime and induce desirable properties such as porosity, thickness of coating, and stronger support adhesion in the final deposit/coating. A single compound (even the metal source) can even play multiple roles (e.g., stabilizer, complexing agent, and depolarizer). These compounds are labeled according to the respective intended function in the electroless bath. The residual quantities of additives left behind in deposits can often deteriorate the quality of the final product.

1.2.3.2 ED THEORY

In the ED process, deposited secondary metal is selectively formed on catalytically active sites of the prmary metal by the chemical reduction of a metal salt from an aqueous solution. An example of the redox reactions occurring during ED may be seen in Figure 1.6 [53]. The figure depicts a substrate, which can be thought of as a catalytically-active site (typically a metal which may exist as a uniform coating or as isolated particles on a non-metallic support). The substrate is composed of anodic and catholic sections. In practice, however, the anode and cathode are adjacent sites on a metal surface. By convention, oxidation (loss of electrons) takes place on the anode and reduction (gaining electrons) occurs on the cathode [56]. In this case, hypophosphite ($H_2PO_2^-$) is the reducing agent that supplies electrons through the anodic reaction [49, 53]:

$$H_2PO_2^- + H_2O \rightarrow H_2PO_3^- + 2H^+ + 2e^- \qquad [1.1]$$

The electrons donated to the substrate then travel to the cathodic section where they are used for the nickel reduction reaction:

$$Ni^{2+} + 2e^- \rightarrow Ni \qquad [1.2]$$

In general these overall oxidation, and reduction reactions may be expressed as [52, 54]:

$$M^{z+} + R^{n-} \text{ (catalyst)} \rightarrow M^{0} + R^{z-n} \text{ (overall)} \qquad [1.3]$$

$$R^{n+} \rightarrow R^{n+z} + ze^{-} \text{ (oxidation)} \qquad [1.4]$$

$$M^{z+} + ze^{-} \rightarrow M^{0} \text{ (reduction)} \qquad [1.5]$$

Where R is the reducting agent, z is the valence, and M is any of the viable ED metals described previously. At steady state these oxidation and reduction reactions occur simultaneously such that no net current (movement of electrons) is generated [49]. At that point, the current being generated by the anodic reaction exactly equals the current from cathodic reaction. This current is directly related to the rate of the electroless deposition reactions [55].

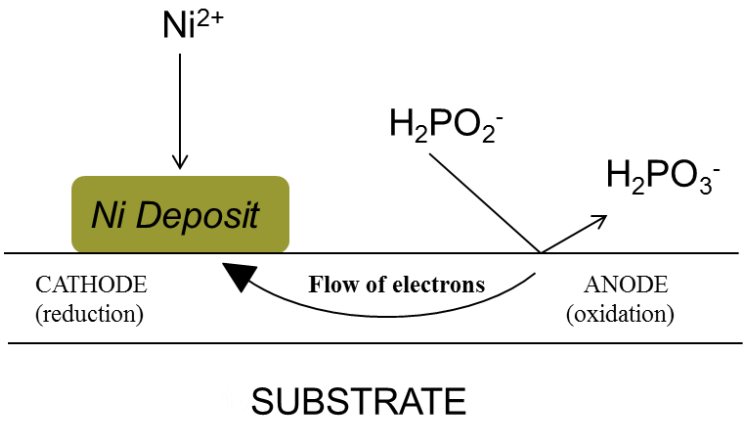

Figure 1.6 A schematic of the electroless deposition of nickel using hypophosphite as the reducing agent [53].

When the ED method is used for synthesis of bimetallic catalysts, it can be further distinguished according to whether the secondary metal deposits on a primary metal or substrate (i.e., catalytic deposition) or on to deposited secondary metal sites (auto-catalytic deposition) (see Figure1.7). Since both phenomena involve the reducing agent it

can be difficult to distinguish between catalytic and auto-catalytic processes. They can occur in conjunction or succession in electroless deposition depending on the activities of metals towards reductant oxidation. Nevertheless, ED starts always with catalytic deposition, where the primary metal substrate acts as catalyst. It is only after the surface is covered (or partially covered) by a monolayer of metal that the autocatalytic deposition begins.

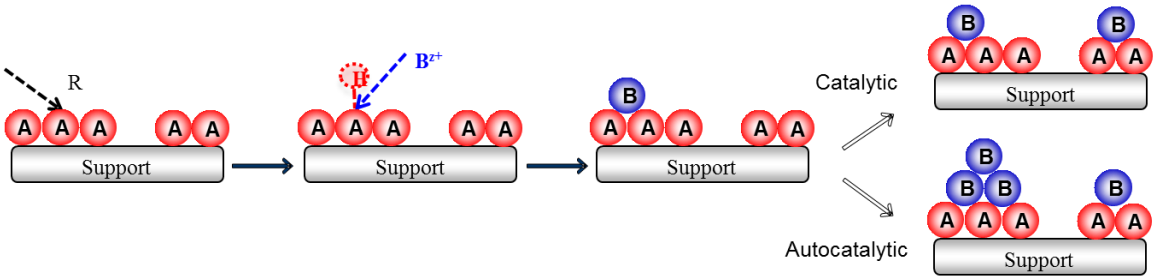

Figure 1.7 A schematic of the electroless deposition. Where R, A and B represents as reducing agent, primary metal and second metal, respectively.

1.2.3.3 ED OF SILVER AND GOLD

The two metals most commonly deposited using ED are Ni and Cu. However, as noted previously, many other metals may be deposited using ED [52]. Silver is particularly interesting for decorative purposes and for use in electronics, since it has highest electrical conductivity of all metals commonly used for electrical devices [57]. Electroless deposition of gold, like silver, has also been developed for both decorative and electronic applications [52, 57].

The following are some of the most commonly used metal ion sources, complexing agents, stabilizing agents, and reducing agents for silver and gold electroless plating.

Table 1.3 Commoly used metal sources and agents for Ag and Au ED bath [52, 57] .

	Ag ED bath	Au ED bath
Metal Ion Source	$AgNO_3$, $KAg(CN)_2$	$KAu(CN)_2$, $KAuCl_4$, $Na_3Au(SO_3)_2$
Complexing Agent	Cyanide, ammonia, organic acids, arabic gum, gelatin	Cyanide, sulfite, ethanolamine, citrate, chloride
Reducing Agent	Formaldehyde, hydrazine, glucose, Rochelle salt, sodium hypophosphite, sodium thiosulfate, dimethylamine borane, glyoxal	Formaldehyde, hydrazine, sodium hypophosphite, dimethylamine borane, KBH_4, hydroxylamine, cyanoborohydride
Stabilizing Agent	3-iodotyrosine, 3,5-diiodotyrosine, ammonia, Cu^{2+}, Ni^{2+}, cysteine, dimethyldithio carbamate	Nitrilotriacetic acid, mercaptosuccinic acid, dithizone, 2-mercapto-benzothiazole

CHAPTER 2

EXPERIMENTAL TECHNIQUES

2.1 LIST OF CHEMICAL MATERIALS

Fourth generation hydroxyl-terminated poly(amido)amine (PAMAM) dendrimer (G4OH) (10 wt% in methanol solution, Aldrich).

Gamma-delta-theta phase alumina (specific surface area =104 m^2/g, pore volume = 0.9 mL/g, provided by Toyota)

Gold chloride ($HAuCl_4$, Aldrich)

Hydrazine (35 wt.% N_2H_4 solution, Sigma-Aldrich)

Hydrochloric acid (HCl): EMD, 34-37%

Iridium trichloride ($IrCl_3 \cdot 3H_2O$, AlfaAesar)

Potassium dicyanoaurate ($KAu(CN)_2$, (68 wt.% Au), Sigma-Aldrich)

Potassium silver cyanide ($KAg(CN)_2$ (54 wt.% Ag), supplied by Technic, Inc.)

Silver nitrate ($AgNO_3$, $\geq$ 99%, Sigma-Aldrich)

Sodium boron hydride ($NaBH_4$, ReagentPlus: Sigma-Aldrich)

Sodium hydroxide (NaOH, EM pellets, 97% assay)

2.2 CATALYSTS PREPARATION

Alumina supported Ir, Au and Ag monometallic and Ir-based bimetallic catalysts (i.e., Ir-Au or Ir-Ag) were prepared using three different techniques: conventional incipient wetness (IW), dendrimer metal nanocomposites (DMN), and electroless

deposition (ED). A general description of these synthesis methods are provide here, while the specific details can be found in the Experimental Sections of Chapters 3-6.

2.2.1 Conventional Incipient Wetness

Conventional Ir, Au and Ag catalysts were made by incipient wetness method. A proper amount of metal precursor solution ($IrCl_3 \cdot 3H_2O$, $HAuCl_4$, and $AgNO_3$ as metal sources) was added dropwise to Al_2O_3 and the resulting slurry was dried in an oven at 60°C overnight before use. A proper pretreatment was conducted to activate the surface metal sites. In the case of conventional Ir-Au bimetallic catalysts, equal volumes of Ir and Au metal precursor solutions were mixed together and then added to the Al_2O_3.

2.2.2 Dendrimer Metal Nanocomposites

Since the dendrimer metal nanocoposite method does not work well for ions such as Ag^+ which only weakly complex to the dendrimer, only Ir, Au and Ir-Au catalysts were prepared by this method. For monometallic catalysts, a proper amount of metal precursor solution ($IrCl_3 \cdot 3H_2O$ and $HAuCl_4$) was added under N_2 purging to G4OH dendrimer solution to reach a molar ratio of metal to G4OH of 20:1. The mixed solution was stirred at room temperature with N_2 flowing to protect the metal ions from oxidation by dissolved O_2 and allow the complexation of metal ions with the functional groups in the G4OH dendrimer. The formation of dendrimer encapsulated metallic nanoparticles in solution was attempted by adding a 10-fold excess solution of $NaBH_4$ at room temperature. These dendrimer metal nanocomposites (DMNs) were then loaded onto alumina support by standard wet impregnation. The extra water was removed under

ambient conditions by evaporation of the stirring slurry for 3 days. For bimetallic Ir-Au DMNs, a sequential method was followed, whereby one metal was complexed with the dendrimer, followed by the second metal. For both monometallic and bimetallic catalysts, a proper pretreatment was conducted to thermally remove the dendrimer and activate the surface metal sites. The specific details are described in Chapters 3 and 4.

2.2.3 Electroless Deposition

To prepare Ag-Ir and Au-Ir bimetallic samples, the electroless deposition of Ag or Au on a conventionally prepared Ir/Al_2O_3 was conducted using an aqueous bath containing potassium silver cyanide, $KAg(CN)_2$, or potassium dicyanoaurate, $KAu(CN)_2$, respectively, as metal precursor sources. The initial metal ion concentration in the ED bath was varied depending on the targeted weight loadings of the second metal. Hydrazine was chosen as the reducing agent, and NaOH and/or HCl were used to adjust the pH of the ED bath. Once the optimized ED bath was prepared, a proper amount of primary Ir/Al_2O_3 catalyst was added into ED bath. All baths were then vigorously stirred to minimize any possible external mass transfer limitations. As the Ag or Au deposition was conducted at room temperature (RT), small aliquots of ED solution (<2 ml) were collected to monitor the concentrations of the second metal ion remaining in the bath during deposition. After the completion of ED, the slurry was filtered, washed, dried, and stored at ambient conditions. The catalysts were then subjected to a proper pretreatment to activate the surface metal sites. The specific details are described in Chapters 5 and 6.

2.3 CATALYSTS CHARACTERIZATION

2.3.1 SCANNING TRANSMISSION ELECTRON MICROSCOPY (STEM)

Scanning transmission electron microscopy (STEM) was conducted using a JEOL 2100F 200 kV FEG-STEM/TEM equipped with a CEOS Cs corrector system. High angle annular dark-field (HAADF) STEM images were acquired on a Fischione Model 3000 HAADF detector with a camera length such that the inner cut-off angle of the detector was 50 mrad. Holey-molybdenum coated Cu grids were dipped into finely powdered catalysts samples for examination under the microscope. Histograms of particle size distribution were obtained by measuring at least 300 randomly selected particles from at least 6 different micrographs for any sample analyzed.

2.3.2 ATOMIC ABSORPTION SPECTROSCOPY (AAS)

Atomic absorption spectroscopy was performed on a Perkin-Elmer 3300 and used to determine the elemental concentrations of Ir, Au and Ag. In addition, the weight percentages of metals in the final bimetallic catalysts were also determined by digesting 0.1 g of sample in aqua regia at 120 ℃ for 4 h and then diluting (~20 times) with DI water before analysis. A set of standards (known concentration of each specific element) was prepared to calibrate the instrument before the actual measurements were made.

2.3.3 H_2 CHEMISORPTION STUDIES

Hydrogen chemisorption measurements were performed on an automated AutoChem II 2920 from Micromeritics. For conventionally-derived and dendrimer-derived sample, approximately 0.1 g oxidized sample (350 ℃ for 30 min) was reduced *in-situ* in flowing H_2 (50 mL/min) at 400 ℃ for 1 hour followed by Ar(50 mL/min)

purging at the same temperature for 1 hour to remove any residual H_2. For electrolessly-deposited sample, approximately 0.1 g was reduced *in-situ* in flowing H_2 (50 mL/min) at 200 ℃ for 1 hour followed by Ar(50 mL/min) purging at the same temperature for 1 hour to remove any residual H_2.The chemisorption experiments were done using the pulse methodology by dosing a known volume of 10% H_2/Ar in 4 min intervals. H_2-chemisorbed on the samples was measured at 40 °C and atmospheric pressure and the metallic dispersion and particle size were determined.

2.3.4 FOURIER TRANSFORM INFRA-RED SPECTROSCOPY (FT-IR)

In situ FTIR spectra were recorded using a Nicolet Nexus 470 spectrometer equipped with a mercury-cadmium-telluride B (MCT-B) detector cooled by liquid nitrogen. FTIR spectra were collected in single beam absorbance mode with a resolution of 4 cm^{-1} at room temperature. Catalysts samples of approximately 30 mg were prepared as self-supporting pellets with a diameter of 12 mm. These samples were placed in a variable temperature gas flow transmission cell made of stainless steel. The cell has a length of 10 cm with two IR-transparent NaCl windows cooled with flowing water. The temperature of the cell was monitored by a thermocouple placed near to the catalyst sample. The heating was achieved using a heating element wrapped around the cell and an Omega CN76000 temperature controller.

In order to understand CO adsorption on the Ir-Au or Ir-Ag bimetallic catalysts, the molecular adsorption of CO onto the catalysts was examined after various treatment steps. These treatments include both an oxidation and reduction procedure. Catalyst pellets were placed inside the FTIR cell and first exposed to He flowing gas (~70 mL/min)

in order to remove any impurities. Subsequently, the catalysts were exposed to the desired gas and heated at 5 ℃/min from room temperature to a selected temperature where it was maintained at that temperature for the necessary time. After cooling to room temperature, the system was purged with He 15 min and a background spectrum was recorded. For CO adsorption, a 1% CO/He mixture was flowed through the catalyst for 15 min, followed by He for an additional 15 min to purge CO gas and remove weakly bonded CO species. The same procedure was used for adsorption of NO, except flowing 1% NO in He instead of CO gas mixture. All spectra were referenced to an initial background spectrum taken in He prior to CO or NO exposure.

The curve fitting of these FTIR spectra was conducted with different fitting models (e.g., Gaussian, Lorentzian, log-normal) to obtain the peak position, width, height, and area of the overlapping peaks. Initially, the individual peak parameters (i.e. position, full width at half maximum (FWHM), and height) were chosen based on visual inspection of the experimental spectrum for the Ir-CD sample. Then, the residual between the overall fit and raw spectrum was minimized by minimizing the square root of the sum of square errors in an iterative fashion. The peak deconvolution using spectral curve fitting was continued for other samples in the similar fashion. It was found that all the peaks were effectively modeled by Gaussian line shapes.

2.3.5 X-RAY PHOTOELECTRON SPECTROSCOPY (XPS)

X-ray photoelectron spectroscopy measurements were made on selected samples using a Kratos AXIS Ultra DLD XPS system with a monochromatic Al Kα source operated at 15 keV and 150W and a hemispherical energy analyzer. All oxidized samples

were reduced at 400 ℃, the same temperature used for all other characterization methods, for experimental consistency. After pretreatment, the samples were transferred into the UHV chamber for XPS analysis without exposure to air. The XPS spectra were fitted to a Shirley-Linear background using XPSPEAK software version 4.1. The deconvolution was accomplished with Gaussian-Lorentzian band shapes. Appropriate peak positions, FWHM's and area constraints were used for peak splitting of 4f electron. The FWHM was maintained constant at ~2.0 eV for Ir 4f and ~1.3 eV for Au 4f electrons. The shifts reported are accurate to within ±0.1 eV. The Al(2p) binding energy (BE) was used as a reference and was compared to the literature value of 74.4 eV. The same difference (charging correction) in eV was applied to all other XPS peaks to give corrected BE's of Ir(4f), Au(4f), Ag(3d) and O(1s) electrons for both monometallic and bimetallic systems.

2.4 CATALYSTS EVALUATION

2.4.1 CO OXIDATION

The catalytic oxidation of CO was performed in a quartz single-pass fixed-bed microreactor at atmospheric pressure, a space velocity of 100,000 $mL \cdot g^{-1}h^{-1}$, and temperatures between 25 and 400 ℃.

- With NDIR analyzer (For dendrimer-derived Ir-Au bimetallic sample)

The reaction feed contained 1000 ppm of CO and 500 ppm of O_2 balanced with He. The inlet and outlet of the reactor were analyzed with an on-line single beam NDIR analyzer (Ultramat 23, Siemens) capable of detecting CO with a limit of 1 ppm. Prior to the catalytic measurements, the samples were treated in a flowing10% O_2 in He mixture

or H_2 as the temperature was ramped at 5 ℃/min and then held at the desired value for 2 h. No measurable conversion of CO was observed in the absence of a catalyst.

- With MS analyzer (For electrolessly-deposited Ag-Ir and Au-Ir bimetallic sample)

The reaction feed contained 4000 ppm of CO and 2000 ppm of O_2, with balance He. The outlet of the reactor was monitored by means of a quadrupole mass spectrometer (Inficon, Transpector 2 gas analysis system, MS) equipped with a fast response inlet/leak valve system. All lines between the reactor outlet and the inlet of the MS, including also the latter, were held at 120 ℃. Prior to the catalytic measurements, the ED-derived samples were reduced in situ in flowing H_2 at 200 ℃ for 1 h. A flow of He gas was used for 30 min at the same temperature to purge residual H_2 from the system, followed by system cooling to room temperature. Steady state for the reaction was considered achieved for a given temperature when the mass intensities for reactant and product species were constant with time. Mass numbers (*m/z*) of 4, 18, 28, 32 and 44 represent He, H_2O, CO (the CO peak was corrected for the m/z = 28 peak resulting from CO_2 fragmentation), O_2 and CO_2, respectively. No measurable conversion of CO was observed in the absence of a catalyst.

For the calculation of turnover frequencies (TOFs) for the CO oxidation reaction, reaction rates calculated from the CO light-off curve and metal dispersion converted from H_2 chemisorption data (or O_2 chemisorption at 170 ℃ for the Ag/Al_2O_3 sample) were considered for each catalyst.

2.4.2 NO-CO REACTION AND DIRECT NO DECOMPOSITION

The catalytic evaluation for the NO-CO and direct NO decomposition reactions were performed in a fixed-bed quartz reactor at atmospheric pressure using space velocities of 100,000 and 5,000 $mL \cdot g^{-1}h^{-1}$, respectively. The temperature range was 25-600 ℃ with a ramp of 5 ℃/min. For the NO-CO reaction, 60 mg of sample was loaded and the reaction feed contained 2000 ppm of NO and 2000 ppm of CO balanced with He. Direct NO decomposition was carried out with 200 mg of sample and the feed contained 2000 ppm of NO balanced with He. For temperature-programmed desorption of NO (NO-TPD), 50 sccm of 1% NO/He was used at room temperature for 30min, followed by He purge for another 30min, and then NO-TPD was recorded in He gas. The outlet of the reactor was monitored by means of a quadrupole mass spectrometer (MS) equipped with a fast response inlet capillary/leak valve system. All lines between the outlet of reactor and the inlet capillary of the MS, including also the latter, were held at 120 ℃. Prior to the catalytic measurements, the oxidized samples were reduced in situ in flowing H_2 at 400 ℃ for 1 h. A flow of He gas was used for 30 min at the same temperature to purge the residual H_2 from the system, followed by system cooling to room temperature. Steady state for the reaction was considered achieved for a given temperature when the mass intensities for reactant and product species were constant with time. Mass numbers (*m/z*) of 2, 15, 18, 28, 30, 32, 44 and 46 represents H_2, NO, H_2O, N_2(CO), NO(NO_2), O_2, N_2O(CO_2) and NO_2, respectively.

For the calculation of turnover frequencies (TOFs) for the reactions over each catalyst, reaction rates calculated from the light-off curves at differential conversions (i.e., less than 20%) and metal dispersion derived from chemisorption data were used.

CHAPTER 3

PREPARATION, CHARACTERIZATION OF DENDRIMER-DERIVED BIMETALLIC Ir-Au/Al_2O_3 CATALYSTS FOR CO OXIDATION

In this chapter, the synthesis of alumina supported Ir-Au bimetallic catalysts using the dendrimer metal nanocomposite (DMN) approach is reported. The surfaces and nanostructures of four bimetallic DMN-derived samples with similar Ir and Au loading and composition were correlated with their activity for CO oxidation. Results were compared to a catalyst prepared by conventional incipient wetness impregnation of metal salts. Scanning transmission electron microscopy and H_2 chemisorption data reveal that these catalysts have different metallic dispersions with various particle sizes and distributions, depending on the preparation method. Moreover, in situ transmission Fourier transform infrared spectroscopy of CO adsorption allowed for identification of exposed metal surface area in the catalyst. DMN-derived catalysts were tested for CO oxidation, with turnover frequencies calculated in order to determine the intrinsic activity of the samples. Single-pass fixed-bed microreactor measurements show that the activity, measured under identical conditions, differ significantly for these catalysts and are correlated with the catalyst preparation method and with the Au role in the bimetallic catalysts. This points to a distinct Au effect and a direct participation of the Au in the reaction.

3.1 INTRODUCTION

Transition metal-based heterogeneous catalysts are frequently employed in numerous industrial reactions, as well as environmental applications such as automotive catalytic converters and alternative energy areas including fuel cells and biomass conversion. In industry, these supported bimetallic catalysts are often prepared either by wet impregnation or incipient wetness impregnation methods. However, these conventional synthetic techniques do not effectively control the distribution or homogeneity of metals on the substrate in many cases. In addition to less than optimal performance, such nonuniform materials can also be difficult to characterize. In order to obtain uniform materials, several synthetic techniques have been developed over the years including the use of polymers, surfactants, well-defined organometallic cluster complexes, size-selected metal clusters and ionic liquids [5, 6].

One method that has received considerable attention in recent years is the use of dendrimer-metal nanocomposites (DMNs) as precursors [7]. Dendrimers [16] are monodisperse, hyperbranched spherical polymers that emanate from a central core with repetitive branching units, allowing for controllable size. While possessing a very dense exterior, they contain less dense interiors that can be ideal for encapsulation of metal nanoparticles. One of the most successful applications along these lines has been the synthesis of metal nanoparticles using poly-(amidoamine) (PAMAM) dendrimers. Originally pioneered by Crooks et al. [17], the approach takes advantage of the fact that transition metal ions (e.g., Pt^{2+}, Pd^{2+}, Cu^{2+}) can coordinate with the interior tertiary amine and secondary amide functional groups of the dendrimer. The interior void spaces are then used for stabilization and creation of metal clusters or nanoparticles upon reduction

treatment. These dendrimer-metal nanocomposites are stable for extended periods of time and can exhibit interesting catalytic properties [18]. The dendrimer can exert control over size and (in the case of multiple metal ions) composition of resulting nanoparticles or clusters, which can allow for tuning of catalytic properties. There are now many investigations exploring the use of DMNs as precursors to synthesize supported catalysts, and narrow metal particle size distributions have been observed for different transition metals such as Pt, Pd, Au, Ru, Cu, Ir, Pt-Pd, Pt-Au, Pd-Au, Ir-Pd, and Ag-Au catalysts [20-22, 27, 28, 58-62]. However, there is as of yet no information about supported Ir-Au bimetallic catalyst synthesis using the DMNs approach.

The oxidation of CO, although one of the simplest catalytic reactions known [63-67], is important for mitigation of harmful industrial and automotive exhausts [68] and for purification of H_2 feeds for fuel cells [69]. Numerous basic and applied investigations over a variety of catalysts have been performed, and the (relative) simplicity of CO oxidation makes it an ideal probe reaction for surface science investigations [64-67]. This reaction on platinum group metals has been studied extensively, with the majority of investigations having been performed on either supported Pt, Pd or Rh [70-75]. Recently, oxide supported Au nanoparticles have also attracted considerable attention for the reaction of CO oxidation [76] due to their high catalytic activity at low temperatures [77]. Iridium, however, is less explored in this reaction although it is situated among the same 5f orbital metals as Pt and Au. Therefore, in this investigation we examine the catalytic performance of Ir-Au bimetallic catalysts for the CO oxidation reaction. Moreover, because the catalytic performances of gold catalysts are strongly dependent on the size of

the gold particles [78, 79], the nature of the supports and the preparation conditions, the highly dispersed nanoparticles afforded by the DMN approach are desirable.

In this study, a family of dendrimer-derived Ir-Au catalysts has been prepared to illustrate dendrimer-templating effects on bimetallic structure and correlate physical and/or chemical properties of the bimetallic catalysts with their kinetic behavior for CO oxidation. Especially, the role of Au in changing the catalysis of Ir for CO oxidation was focused on. It was found that dendrimer-derived bimetallic catalyst exhibited different metal nanoparticle sizes and distributions associated with different preparation routes and also differ from conventionally prepared samples. In addition, the most highly dispersed Ir-Au bimetallic catalyst was obtained using a dendrimer templating sequential method, resulting in an enhanced activity for CO oxidation.

3.2 EXPERIMENTAL

Fourth generation hydroxyl-terminated poly(amido)amine (PAMAM) dendrimer (G4OH) (10 wt% in methanol solution) was obtained from Aldrich. Prior to use, an aqueous solution was made by evaporating methanol with flowing N_2 and diluting the residue to 1.7×10^{-4} M with deionized water. $IrCl_3\cdot3H_2O$ (AlfaAesar), $HAuCl_4$ (Aldrich) and $NaBH_4$ (granules, 99.995%, Aldrich) were used as received. Deionized water (18 MΩ•cm Milli-Q) was used to prepare all the aqueous solutions. A gamma-delta-theta phase alumina (specific surface area =104 m^2/g, pore volume = 0.9 mL/g) was provided by Toyota. CO, O_2(UHP), He (UHP) and H_2(UHP) were supplied by Airstar.

The synthesis of dendrimer-metal nanocomposites was adapted from the literature [17, 19], and has been published previously [27]. A proper amount of 8.0×10^{-3} M

$IrCl_3 \cdot 3H_2O$ precursor solution was added under the N_2 purging to G4OH dendrimer solution with the concentration of 1.7×10^{-4} M to reach a molar ratio of Ir^{3+} to G4OH of 20:1. The mixed solution was stirred for 7 days at room temperature with N_2 flowing to protect the Ir^{3+} ions from oxidation by dissolved O_2 and allow the complexation of Ir^{3+} ions with the functional groups in G4OH dendrimer. The formation of dendrimer encapsulated metallic Ir nanoparticles in solution was attempted by adding a 10-fold excess solution of $NaBH_4$ at room temperature. The supported catalyst was made by standard wet impregnation of the reduced dendrimer-Ir nanocomposite onto Al_2O_3, to a nominal Ir loading of 1.0 wt % (Ir-DD). The extra water was removed under ambient conditions by evaporation of the stirring slurry for 3 days. The same procedure was used to make dendrimer-Au monometallic nanocomposites except allowing complexation time of 2 minutes, with the corresponding supported catalyst having a nominal Au loading of 1.0 wt% (Au-DD).

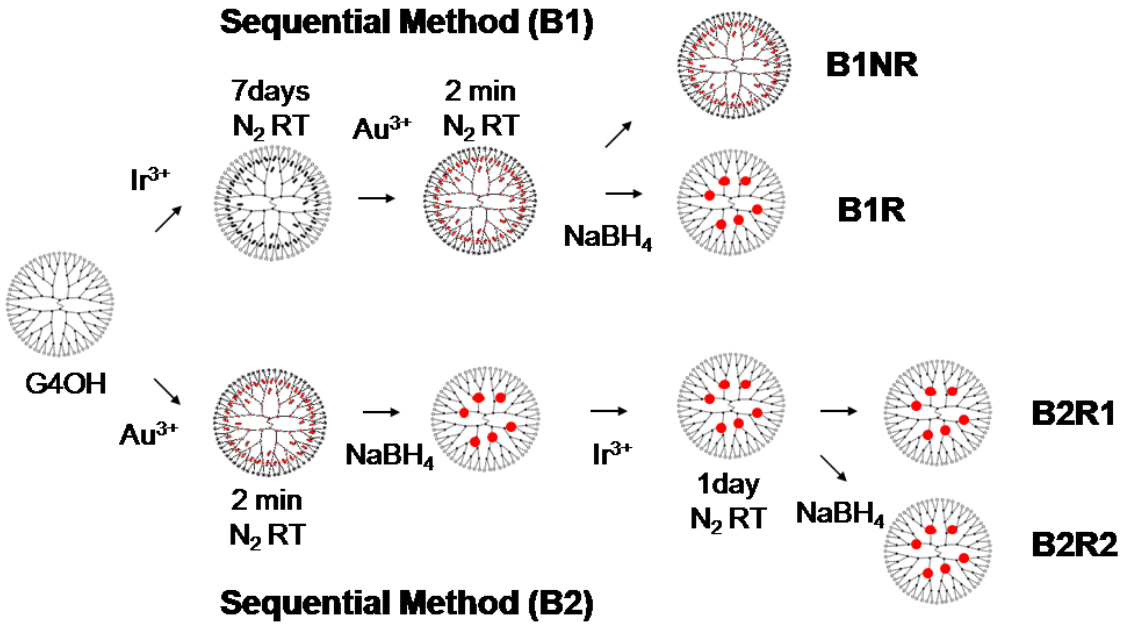

Figure 3.1. Schematic of Ir-Au DMN precursor synthetic routes.

In order to examine the effect of Au on the structure of bimetallic catalysts, two synthesis routes were used to produce bimetallic Ir-Au DMNs, as shown in Figure 3.1. In the sequential method (B1) the Ir metal precursor solution was first mixed with the dendrimer solution, and then allowed to complex for 7 days under N_2 purging. Then, Au metal precursor solution was added, whereupon further complexation occurred (on the order of minutes). This resulting solution was either reduced using $NaBH_4$ (B1R), or used as is (B1NR). Finally the bimetal-dendrimer complex was loaded onto an Al_2O_3 support by wet impregnation. In contrast, the sequential method (B2) involved first mixing Au metal precursor solution with dendrimer solution for 2 minutes, followed by reduction with $NaBH_4$ after complexation was completed. Then, the Ir metal precursor solution was added. The resulting solution was allowed to complex for 1 day under N_2 purging (B2R1), and subsequently reduced once again with $NaBH_4$ (B2R2). This was again followed by impregnation of the bimetal-dendrimer complex onto an Al_2O_3 support. For both methods, the target ratio of each type of metal atom to dendrimer was 20 to 1, thus making a total metal atom loading of 40 atoms per dendrimer. The dendrimer-Ir-Au bimetallic nanocomposites made by both B1 and B2 sequential methods were impregnated onto alumina as described above, with the nominal loading of 1.0 wt% Ir and 1.0 wt% Au.

Conventional Ir and Au catalysts were made by incipient wetness (IW) method (Ir-CD and Au-CD). A proper amount of 5.78×10^{-2} M of $IrCl_3\cdot3H_2O$ precursor solution was added dropwise to Al_2O_3 and the resulting slurry was dried in an oven at 80°C for overnight before use. A conventional Au catalyst was made with exactly the same protocol. In the case of conventional Ir-Au bimetallic catalyst, equal volumes of 11.6×10^{-2} M of $IrCl_3\cdot3H_2O$ and $HAuCl_4$ precursor solutions were mixed together and then added

to the Al_2O_3. The nominal metal loadings of all the conventional catalysts were the same as their DMN-derived analogues.

All catalysts studied were activated under flowing O_2 treatment at 350°C for 30min and H_2 treatment at 400°C for 1 hour with a slow temperature ramp rate of 5°C /min followed by cooling to room temperature. This activation protocol was adapted for consistency from a previous study [62], which showed that G4OH dendrimer template could be sufficiently decomposed on an γ-Al_2O_3 support to expose the metal nanoparticles.

3.3 RESULT AND DISCUSSION

3.3.1 PARTICLE SIZE, DISTRIBUTION AND COMPOSITION

STEM and AA measurements were performed to measure the particle size distributions and compositions of the catalysts after activation using both treatment protocols. Figure 3.2 and Figure 3.3 show STEM images of the Ir, Au monometallic and five bimetallic 1.0 wt.% Ir-1.0 wt.% Au catalysts synthesized by the a) conventional CD b) B1R c) B1NR d) B2R1 and e) B2R2 methods, respectively. Their corresponding particle size distributions with average diameter (D_{ave}) and a volume-surface mean diameter (D_{VSMD}) are presented in the histograms next to the STEM images. Although the same amount of Ir and Au were loaded on alumina support in every case, it was noticed that the morphology of these catalysts varies depending on the synthetic method employed. The conventional catalyst (Ir-Au-CD, Fig. 3.3a) has an asymmetric distribution with most (91 %) of the particles between 0.5-2 nm and the remaining 9% of particles spread out between 2-6 nm creating a broad particle size distribution. Similarly,

a majority of the particles in Ir-Au-B1R (Fig. 3.3b), Au-Ir-B2R1 (Fig. 3.3d) and Au-Ir-B2R2 (Fig. 3.3e) catalysts were smaller than 2 nm (~70% of particles), with the remaining particles scattered over a wide range. In contrast, in the Ir-Au-B1NR catalyst (Fig. 3.3c), a very narrow particle size distribution with a more symmetric distribution was observed and no particles larger than 3 nm were observed.

It is apparent that the conventional Ir-Au catalyst(Ir-Au-CD) has a larger volume-surface mean diameter (3.1 ± 0.8 nm) with lower H_2 dispersion (10%) and broader size distribution than the dendrimer-derived Ir-Au-B1NR catalyst with VSMD of 1.6 ± 0.1 nm and 43% H_2 dispersion, as listed in Table 3.1. This implies that G4OH PAMAM dendrimer exerts control over particle formation. However, despite using dendrimer templating approach, bimetallic catalysts synthesized by the B1R, B2R1 and B2R2

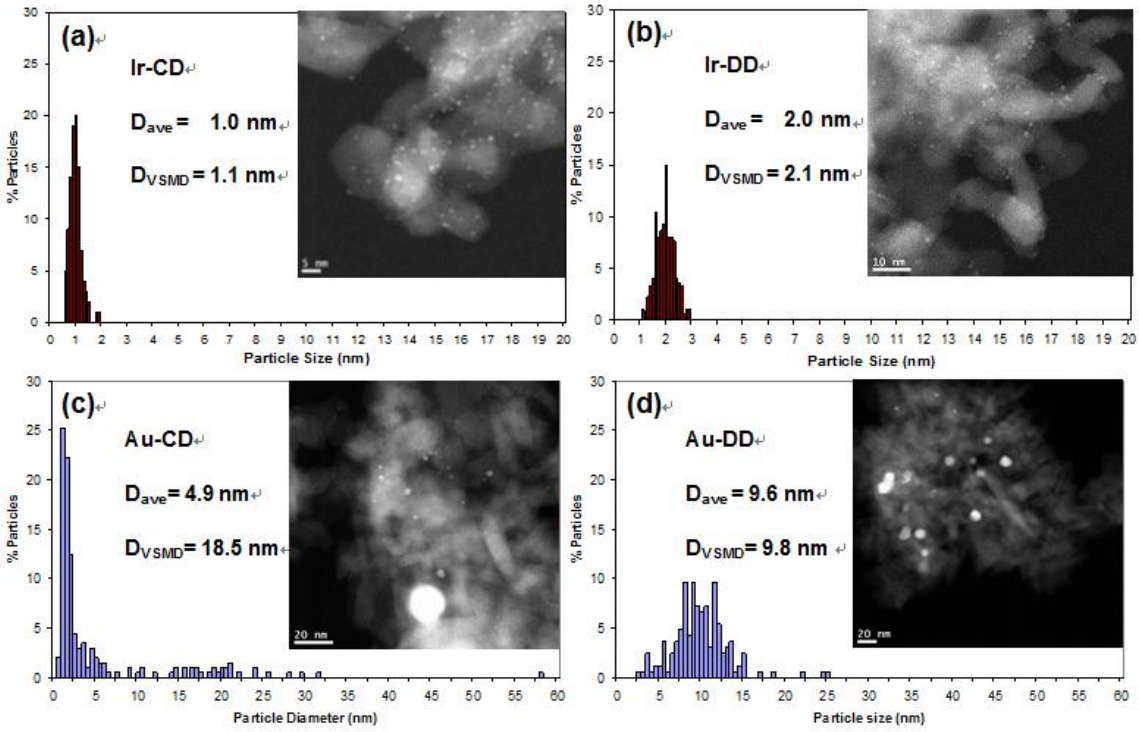

Figure 3.2. STEM images and histograms of Ir/Al_2O_3 and Au/Al_2O_3 monometallic catalysts (a) Ir-CD, (b) Ir-DD, (c) Au-CD and (d) Au-DD.

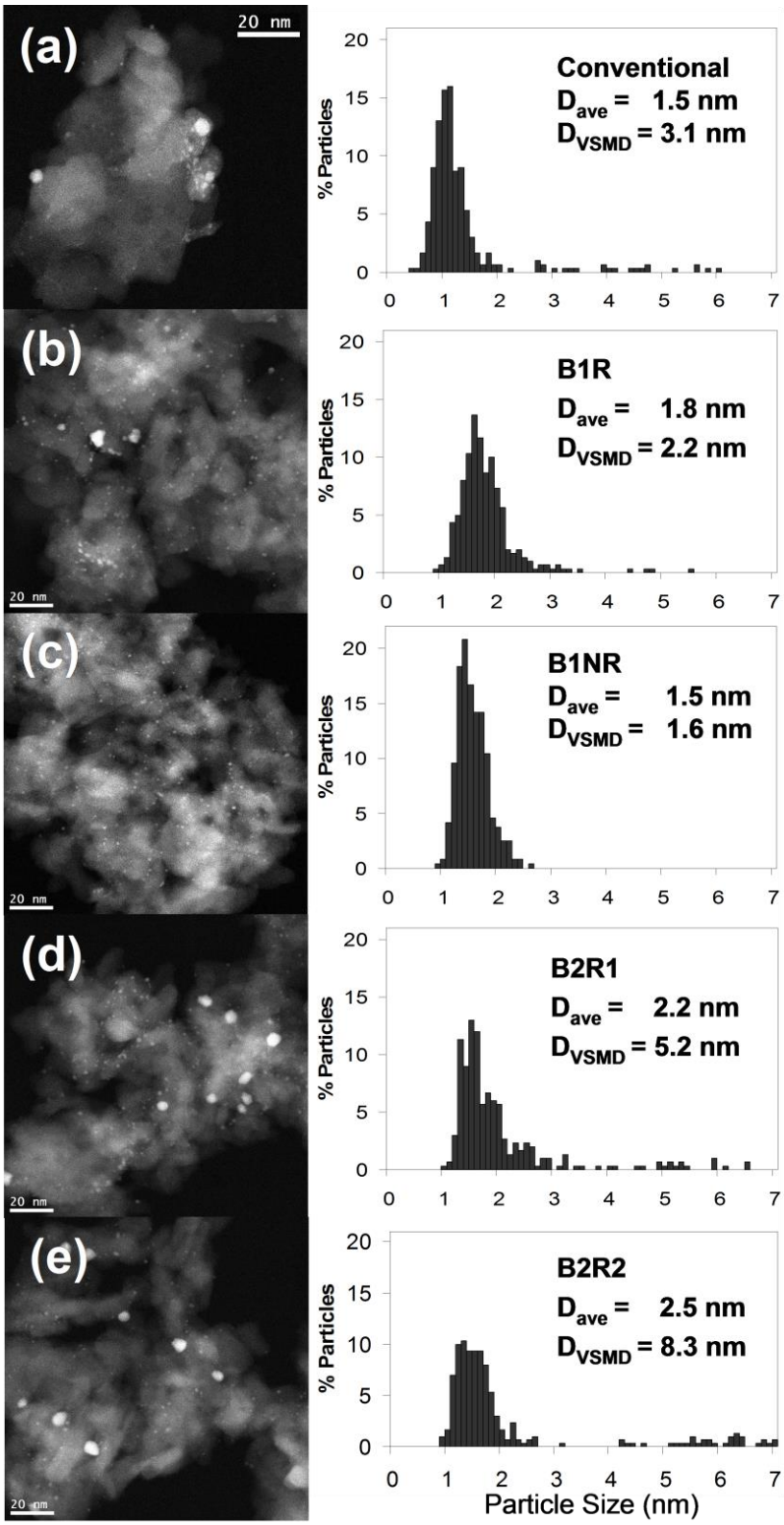

Figure 3.3. STEM images and histograms of Ir-Au/Al_2O_3 bimetallic catalysts (a) CD, (b) B1R, (c) B1NR, (d) B2R1 and (e) B2R2.

methods exhibit a larger average and volume-surface mean diameter with lower dispersion than Ir-Au-B1NR catalysts. It seems that the total number of times that reducing agent is introduced during the synthesis process affects particle size. The reason for this is not clear. However, Biella et al. reported that the effect of the presence of a reducing agent such as $NaBH_4$ on the dimension and size distribution of gold particles is very high. An increase in Au particle size was correlated directly to increased amounts of $NaBH_4$ [80]. In particular, they obtained larger particles, probably through an aggregation mechanism, when $NaBH_4$ was added in large quantities in one step as opposed to gradual addition. Schaal et al. also demonstrated a substantial decrease in metal dispersion for Ag/SiO_2 catalyst with increasing concentration of reducing agents such as formaldehyde, dimethylamine borane, or hydrazine [81]. The particle size distribution showed that exposure of reducing agent resulted in an increase in average particle size and an overall broadening of the particle size distribution.

As shown in Table 3.1, when dendrimer precursors are used to prepare 1.0 wt.% Ir monometallic catalyst (Ir-DD), the result is a catalyst with a larger volume-surface mean diameter (2.1 ± 0.1 nm) than conventional Ir (Ir-CD) that is 1.1 ± 0.1 nm. Nevertheless, both methods produce supported Ir particles with a very narrow distribution. On the other hand, as has been observed previously for other metals such as ruthenium and rhodium [27, 82], DMN precursors do appear to play a role in controlling the sintering/agglomeration processes of Au nanoparticles over alumina, thus influencing the particle size and distribution. Thus, dendrimer-derived Au (Au-DD) has a much smaller volume-surface mean diameter (9.8 ± 0.9 nm) than Au-CD catalyst (18.5 ± 1.6 nm). Nevertheless, sintering of alumina supported Au nanoclusters during the dendrimer

thermal removal step was substantially larger than that observed for Ir particles on the same support [83].

Table 3.1 Metal particle size, dispersions, actual metal loading and bulk composition

Catalysts[a]	STEM		H_2 Disper-sion[d] (%)	Metal Weight Loading[e]		Bulk Compositi-on[e]	
	Volume Surface Mean Diameter[b](nm)	Geometrical Dispersion[c] (%)		Ir (%)	Au (%)	Ir (%)	Au (%)
Ir-CD	1.1±0.1	91±6	74±7	1.0	–	100	–
Ir-DD	2.1±0.1	52±5	65±9	1.0	–	100	–
Ir-Au-CD	3.1±0.6	35±12	10±1	0.9	1.0	48	52
Ir-Au-B1R	2.2±0.4	50±13	16±5	1.0	1.0	48	52
Ir-Au-B1NR	1.6±0.1	68±6	43±3	1.0	1.0	50	50
Au-Ir-B2R1	5.2±1.1	21±7	20±8	1.0	0.8	57	43
Au-Ir-B2R2	8.3±2.0	13±5	17±6	1.0	0.8	54	46
Au-CD	18.5±1.6	6±1	–	–	0.9	–	100
Au-DD	9.8±0.9	12±2	–	–	0.7	–	100

[a]All catalysts were prepared by conventional-derived (CD) and dendrimer-derived (DD) method including B1R, B1NR, B2R1 and B2R2 (see Figure 1 for detail).

[b]Calculated using $\overline{D} = \sum_{i}^{N} N_i D_{p,i}^3 / \sum_{i}^{N} N_i D_{p,i}^2$, where N_i is number of particles and $D_{p,i}$ is the measured diameter from STEM images [84].

[c]Estimated by Volume Surface Mean Diameter values from STEM.

[d] Obtained by H_2 chemisorption analysis(H per Ir metal).

[e]Obtained by elemental analysis.

The sintering of supported metal clusters depends on the type of metal, and can explain the discrepancy in the role of starting metal in influencing final bimetallic average particle size. When Au metal was reduced first, then Ir metal precursor solution was added (i.e., B2 method), the final average particle size was relatively larger than for

the B1 method, which starts with Ir metal followed by Au metal precursor addition. The fact that Ir helps to control Au sintering seems to be in agreement with previous literature [76]. It was found that when Ir and Au were deposited sequentially on TiO_2 support, the bimetallic sample was more homogeneously deposited on the support and more stable against sintering than the codeposition method. Liu et al. [85] also showed by DFT calculations in the $Au/IrO_2/TiO_2$ system that the introduction of the dual-oxide support allows the presence of an active Au/IrO_2 interface that could increase the resistance to sintering of gold nanoparticles. They indicated that nucleation of Au typically occurs at O-vacancy sites and that the bonding of Au with IrO_2 is intrinsically stronger compared to other oxides. The results supported Haruta group's experimental finding [86] that Au preferentially grows on IrO_2 in an IrO_2-TiO_2 binary support resulting in an active catalyst having long-term stability.

Table 3.1 lists the estimated geometrical dispersion of metal (Au + Ir) from STEM (D_{VSMD}) and the Ir dispersion measured by H_2 chemisorption. The latter values were obtained by assuming that Au does not chemisorb H_2. By comparing these two values, the catalysts can be classified as follows. The first group (Ir-Au-CD, B1R) showed much lower H_2 dispersion compared to the geometrical dispersion. In these cases, the surface would appear to be enriched with Au, as indicated by the decreased CO adsorption observed in the FTIR spectra (cf. Figure 3.4). The second group includes the B2R1 or B2R2 samples, where the estimated dispersions based on STEM and H_2 chemisorption are very similar. This implies the surface would be enriched with Ir. Finally, the B1NR sample has the smallest particle size and tightest distribution, and a 50% higher geometrical dispersion compared to that estimated from H_2 chemisorption. It

therefore seems likely that B1NR contains reasonably uniform mixtures of Ir and Au, with some mixed Ir-Au on the surface based on the FTIR of CO adsorption (cf. Fig. 3.4). The actual metal loading and bulk composition were obtained via atomic absorption spectroscopy (AAS). As shown in Table 3. 1, the actual metal weight loading was similar to the nominal values and the average percentages of Ir present in the catalysts are similar to 50% average elemental composition, albeit with some scatter.

3.3.2 Infrared Spectra of Adsorbed CO

Spectra collected following the adsorption of CO at room temperature on the monometallic Ir and Au catalysts, and the five Ir-Au bimetallic samples, are shown in Figure 3.4.

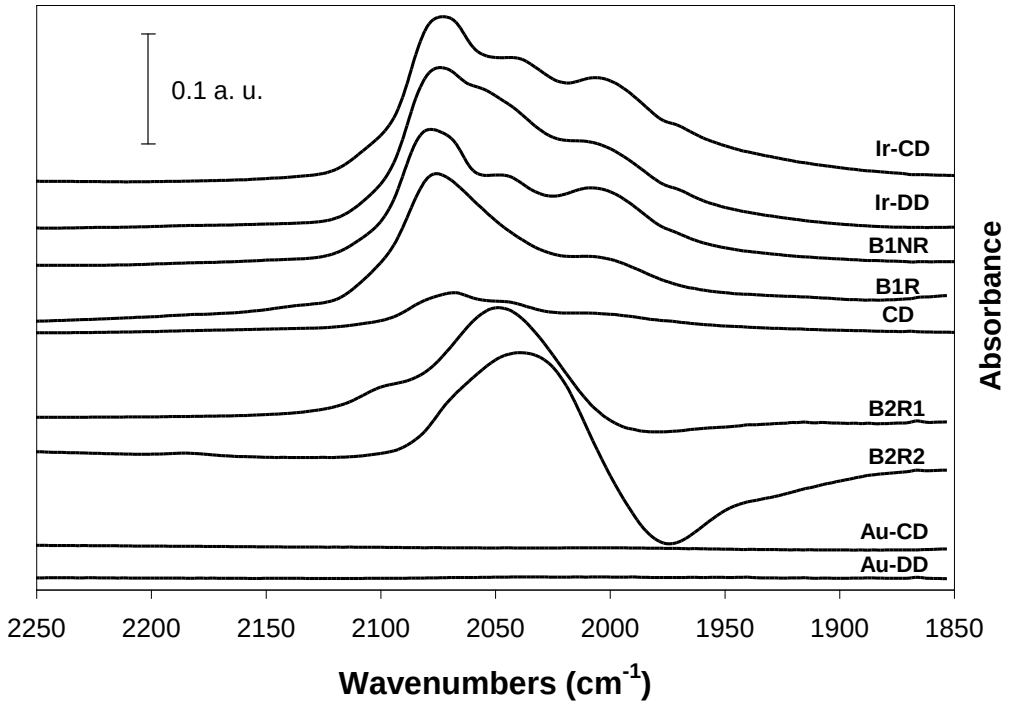

Figure 3.4. FTIR-CO adsorption of Ir/Al_2O_3, Au/Al_2O_3 and $Ir\text{-}Au/Al_2O_3$ bimetallic catalysts with different preparation method.

No characteristic ν_{CO} vibrations were observed in the spectra of the Au-CD and Au-DD samples, which had an average Au particle size of approximately 19 and 10 nm (Table 3. 1). This result is consistent with previous literature reports demonstrating that the adsorption of CO on Au depends on the particle size of the Au crystallites and is observed only on Au nanoparticles with sizes below 5 nm [87, 88].

When the conventional and dendrimer-derived Ir monometallic samples (Ir-CD and Ir-DD) were exposed to CO under similar conditions, three strong bands were observed at 2008,2040 and 2074 cm^{-1}. As a matter of fact, there are several peaks involved between 2000 and 2100 cm^{-1} and can generally be assigned to linearly adsorbed CO species on fully reduced Ir sites (2035, 2053cm^{-1}) or on partially oxidized Ir sites (2092cm^{-1}) or antisymmetric (2012cm^{-1}) or symmetric (2078 cm^{-1}) vibrations of adsorbed dicarbonyl species on Ir ions (see Figure 3.5 for detail). The assignment of these peaks in this small region is based on our previous published work [89] and the available literature [90-99].

Similar results were also obtained with the Ir-Au-B1NR, B1R and CD bimetallic (Ir-Au-CD) samples in terms of their peak positions. However, the intensities of the peaks varied depending on the catalysts. The peak intensities in the spectra for the Ir-Au-B1NR or B1R samples were almost the same as those for the Ir-DD sample. On the other hand, the spectra of Ir-Au-CD exhibited much weaker band intensities compared to the Ir monometallic or B1NR bimetallic samples. Such a depressed peak could be related to Ir active sites exposed to the surface. The H_2 chemisorption data show that after oxidation/reduction treatment, the Ir-Au-CD sample had a much lower dispersion when

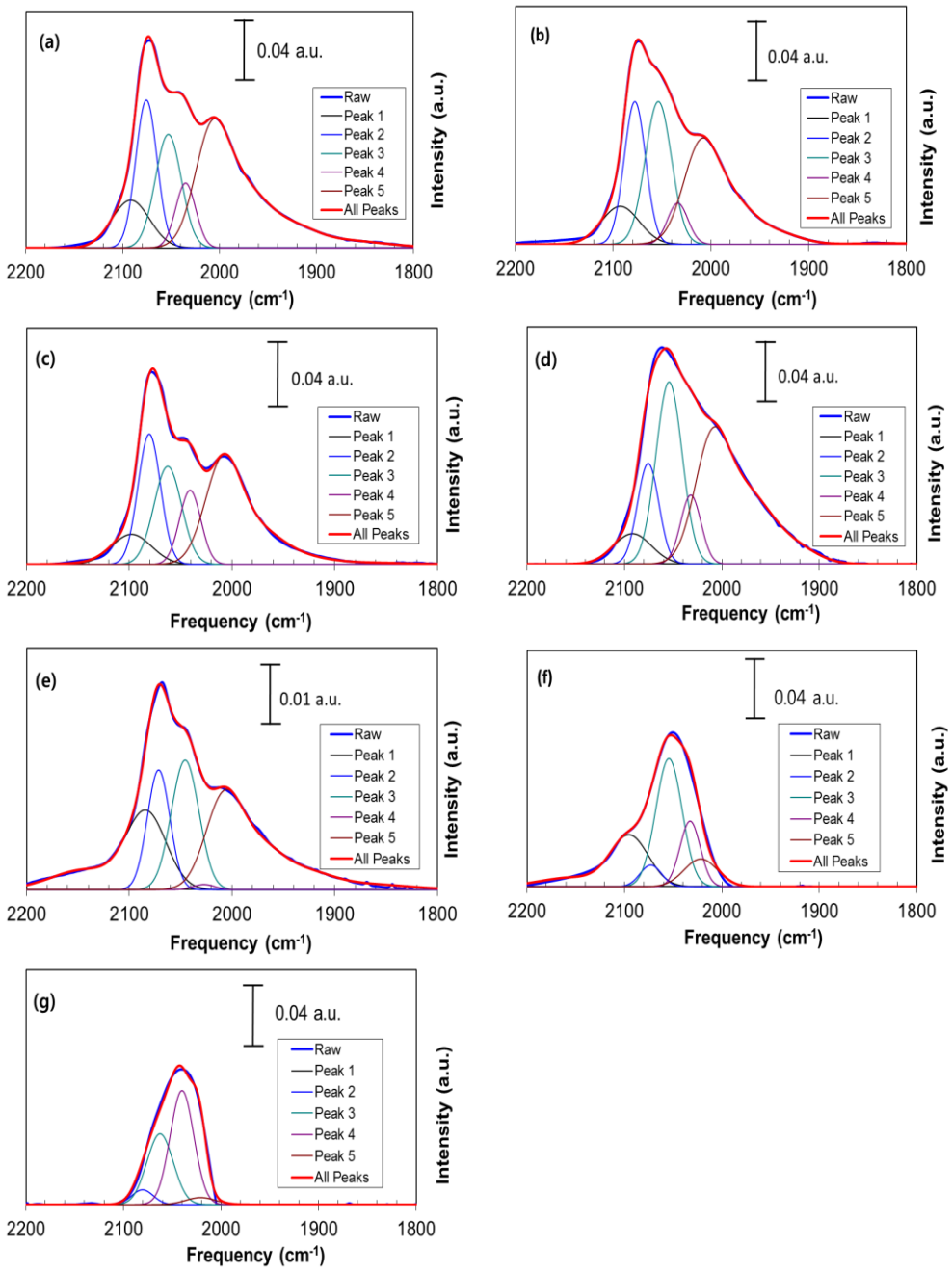

Figure 3.5. FTIR-CO adsorption and peak fitting of Ir/Al_2O_3 monometallic catalysts (a) Ir-CD, (b)Ir-DD and $Ir-Au/Al_2O_3$ bimetallic catalysts with different preparation method (c) B1NR, (d) B1R, (e) CD, (f) B2R1, (g) B2R2. (Linearly adsorbed CO species on partially oxidized Ir sites (Peak 1) or on fully reduced Ir sites (Peak 3, 4) or symmetric (Peak 2) or antisymmetric (Peak 5) vibrations of adsorbed dicarbonyl species on Ir ions.)

compared to Ir-CD (Table 3. 1). The dispersion decreased from 74% to 10%, indicating that the number of Ir active sites of the surface was significantly decreased by the presence of Au metal atoms.

When similar FTIR experiments were repeated with the Au-Ir-B2R1 and B2R2 samples, different peak shapes were obtained from the other three bimetallic samples. The peak maximums are located at 2050 cm^{-1} for B2R1and at 2040 cm^{-1} for B2R2, as opposed to the higher frequency (i.e., 2074 cm^{-1} in the case of conventional samples). These observed patterns clearly indicate that linearly adsorbed CO species on fully reduced Ir sites (2035, 2053cm^{-1}) are more dominant than adsorbed dicarbonyl species on Ir ions (2012, 2078 cm^{-1}). Specifically, the band at around 2078cm^{-1} is due to the symmetric dicarbonyl vibration and the ca. 2008 cm^{-1} band is due to the antisymmetric carbonyl vibration [92]. Generally these bands are found in highly dispersed Ir catalysts, where the gem dicarbonyl species adsorbs on small clusters or isolated Ir atoms that can accommodate the simultaneous adsorption of two CO molecules [93]. Thus, the different band appearance in the B2 samples appears to result from adsorption on larger metal particles in these samples, as confirmed by STEM measurements.

The negative peaks observed in the B2R1 and B2R2 samples are attributed to the gradual removal of adsorbed carbonyl containing dendrimer fragments upon exposure to carbon monoxide.

3.3.3 Catalytic Oxidation of CO

In order to evaluate the catalytic activity for a family of alumina supported Ir-Au catalysts, CO oxidation was chosen as a probe reaction. The light-off curves showing the

temperature dependence of CO oxidation over those Ir-Au bimetallic samples are shown in Figure 3.6. As references, Ir and Au monometallic catalysts were investigated (Figure 3.6a). Similar complete CO conversion behaviors were observed with conventional Ir (Ir-CD) and dendrimer-derived Ir (Ir-DD) catalysts at approximately 250 and 260 ℃, respectively, consistent with the similar structure of these two catalysts. The performance of Ir was much better than that achieved over conventional Au, which required 317 ℃ for complete CO conversion. However, it should be noted that Au-CD sample has much larger particle size than the Ir-CD or Ir-DD samples, and such a poor control of the particle size led to low activity toward CO oxidation. Anumber of reports have pointed to a high activity of iridium supported on Al_2O_3 [99], SnO_2, TiO_2 [100], and CeO_2 in CO oxidation [101].

Several previous works [102, 103] have also demonstrated that a secondary metal can improve the catalytic performance of Ir in the preferential oxidation of CO (PROX) reaction. For example, Nojima et al. [103] investigated the effect of Rh, Pd, Cr, Co, Ni, Cu, Fe and Sn on supported Ir catalyst for PROX reaction. In their report, Ir–Rh and Ir–Fe catalysts showed highest activity for CO selective oxidation because of the suppression of hydrogen adsorption and promotion of CO adsorption in a wide range of reaction temperatures.

Figure 3.6b shows the effect of Au on Ir catalysts for CO oxidation. The catalytic activity toward CO oxidation can be varied depending on the synthetic method employed. The highest activity was obtained for the Ir-Au-B1NR catalyst, based on the higher CO conversion over the entire reaction temperature region compared with other bimetallic catalysts. As shown in Table 3. 2, this B1NR sample also represents enhanced catalytic

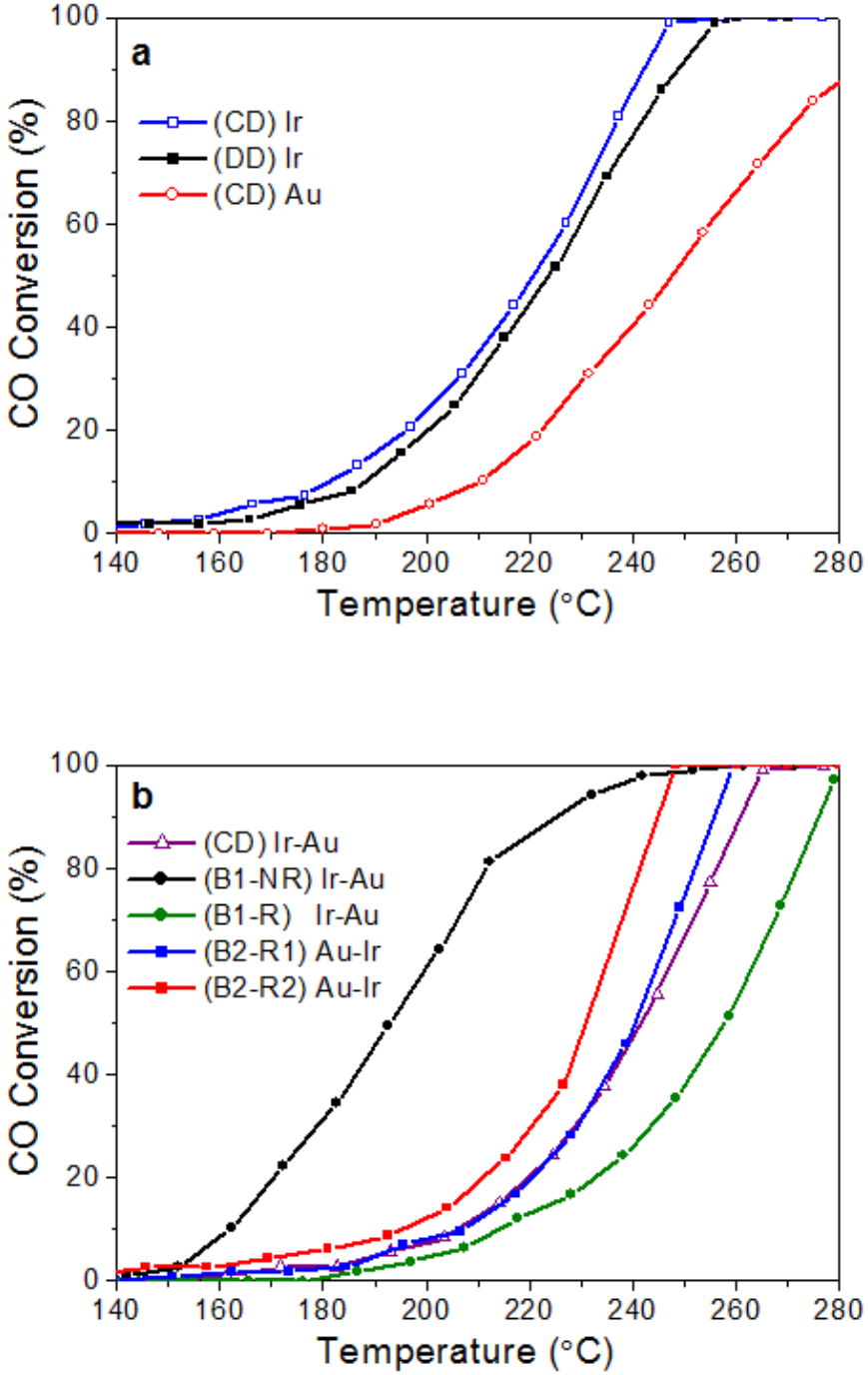

Figure 3.6. Light-off curves characterizing the oxidation of CO by O_2 as function of reaction temperature over (a) Ir/Al_2O_3, Au/Al_2O_3 monometallic and (b) $Ir\text{-}Au/Al_2O_3$ bimetallic catalysts prepared by CD, B1NR, B1R, B2R1 and B2R2 methods.

performance, achieving about 20% conversion of CO at 170 ℃, compared with Ir monometallic catalysts (Ir-CD or Ir-DD) that only show CO conversion of 4-6% at the same temperature. This suggests that the improvement seen for B1NR can be explained by the contributions of Au. However, it is clear that not every bimetallic Ir-Au catalyst showed enhanced performance compared with the monometallic catalyst and this would imply that the Au play a different role in each.

Table 3.2. CO oxidation conversion (%) and TOFs at 170 ℃ for all catalysts

Catalysts	CO conversion (%)	CO oxidation TOFs[a] (min^{-1})
Ir-CD	6.2	10±1
Ir-DD	4.2	8±2
Ir-Au-CD	2.3	28±4
Ir-Au-B1R	0.04	0.3±0.1
Ir-Au-B1NR	19.6	54±5
Au-Ir-B2R1	1.8	11±7
Au-Ir-B2R2	4.4	31±8

[a]Based on metallic dispersion obtained from H_2 chemisorption data.

To study the role of Au in catalytic activity and for better comparison between the catalysts, the intrinsic activities expressed in terms of turnover frequencies (TOFs) were calculated at a reaction temperature of 170 ℃ for the entire family of catalysts, as shown in Table 3.2 and Figure 3.7. This temperature was chosen for comparison since all of the CO conversions were found to be ca 20% or less. Both conventional and dendrimer-derived monometallic Ir catalysts (Ir-CD and Ir-DD) are similar in their activity for CO oxidation based on the TOF values of 10 and 8 min^{-1}, respectively, which suggests that they have similar structures. For Ir-Au bimetallic catalysts, it can be seen that bimetallic samples have generally better activities than Ir monometallic one, except the Ir-Au-B1R sample, which has a TOF of almost zero. As shown in Table 3.2, the B2R1 shows similar

TOF or slightly better activity compared with Ir monometallic samples (Ir-CD or Ir-DD). On the other hand, the B2R2 and the Ir-Au-CD bimetallic sample are about a factor of three more active than Ir monometallic samples. Finally, the Ir-Au bimetallic catalyst prepared by the B1NR method is the most active one among the five bimetallic catalysts examined based on the highest TOF value of 54 min^{-1}. The order of activity of the catalysts is in the following sequence:

B1NR (54 %) » B2R2 (31 %) ≈ CD (28 %) › B2R1 (11 %) ≈ Ir-DD (8 %) › B1R (0.3 %).

This order of activity indicates that the presence of Au plays generally a positive role in the catalytic activities for CO oxidation by varying the surface structure of catalyst and morphology.

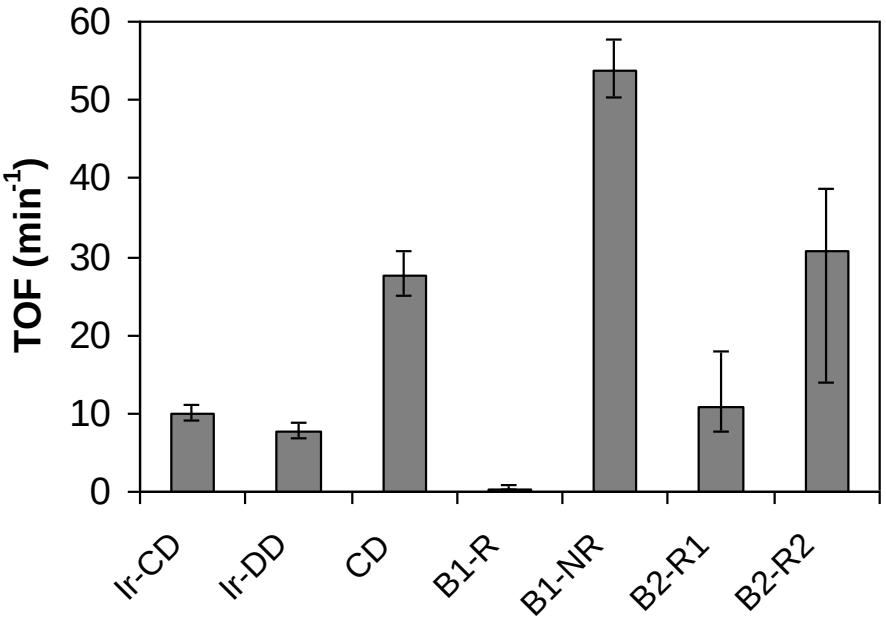

Figure 3.7. TOF of CO oxidation at 170 ℃ for Ir/Al_2O_3 monometallic and $Ir-Au/Al_2O_3$ bimetallic catalysts with different preparation method.

In the case of the conventional derived Ir-Au bimetallic sample (Ir-Au CD), the enhanced activity can be explained by geometric or ensemble effects [104, 105]. The FTIR data suggests that this catalyst appears to be surface enriched in Au since the signal is very low. This conclusion was also made from dispersion analysis, as described in Section 3.3.1. In this case, the dilution of Ir surface sites by Au probably results in the boost in its intrinsic activity. And therefore, the TOF of Ir-Au-CD appears to be about three times higher than Ir monometallic sample.

Although the TOF value of B2R2 sample is similar to the CD bimetallic sample (Ir-Au CD), the possible role of the Au in this B2R2 bimetallic catalyst would be different. This is because the FTIR result suggests quite different surface structure. In addition, unlike the Ir-Au-CD sample, surface enrichment of Ir in the B2 samples was suggested based on the geometrical and H_2 dispersion data. Thus, the enhanced activity for this B2R2 sample is likely attributed to an electronic effect of Au on Ir, rather than a geometric effect. On the other hand, B2R1 is less active than B2R2 based on the lower TOF and it is rather similar to the Ir monometallic sample (Ir-DD). This might be because of the difference in the oxidation state of Ir metal surface sites. By comparing the FTIR spectra of B2R1 and B2R2, it can be noticed that the peak at around 2100 cm^{-1} is absent for B2R2. As described above, this peak can be assigned to linearly adsorbed CO species on partially oxidized Ir sites. This indicates that Ir metal oxide was more effectively reduced during the B2R2 procedure involving two reduction steps, while some of Ir metal oxide still remains for the B2R1 sample. Indeed, the only difference between these two samples in the preparation was the number of reducing agent steps applied.

Finally, B1NR showed the highest TOF among five bimetallic catalysts. It was also about five times more active than Ir monometallic sample. Such an improvement in its activity could be result from: a) bimetallic Ir-Au sites that have higher intrinsic activity caused by geometric or by electronic effect of Au on Ir b) contribution of Au metal sites that can be catalytically active when dispersed as small particles on an oxide support or c) a combination of the two hypotheses. It is easy to check out the first hypothesis by comparing the activities between Ir monometallic and Ir-Au-B1NR bimetallic from the calculated TOF. As shown in Figure 3.7, Au clearly plays a positive role in enhancing the intrinsic activity of Ir metal in B1NR sample, possibly due to the electronic effect. Based on the FTIR data, a comparable amount of CO species was adsorbed on this B1NR sample surface to that on the Ir monometallic sample. This suggests that the size of Ir surface domains is not affected by the presence of Au metal. This also implies that Au is in a highly dispersed state because we know that this catalyst is reasonably uniform mixtures of Ir and Au from the dispersion analysis as described above in Section 3. 3.1.

On the basis of these observations, it is argued that some portion of the metal particles formed in the Ir-Au-B1NR catalyst are likely bimetallic in nature. The close proximity of Ir and Au helps sustain Au in a highly dispersed state that is required to efficiently catalyze the CO oxidation reaction with higher conversion of CO at the same temperature. In this way, the second hypothesis would be in effect. Therefore, the enhanced catalytic activity of B1NR catalyst likely results from Au helping to enhance the intrinsic activity of Ir through an electronic effect combined with more activity resulting from the increased total number of active (i.e., Au) sites.

3.4 CONCLUSION

CO oxidation reactions were investigated in a family of Al_2O_3-supported Ir-Au bimetallic catalysts with various preparation methods. It was noticed that the catalytic activity toward CO oxidation over bimetallic catalysts can be varied depending on the synthetic procedure. A conventionally derived Ir-Au bimetallic sample (Ir-Au-CD) exhibit better intrinsic activity compared with the Ir monometallic catalyst (Ir-CD) due to the geometric effect of Au on Ir. In contrast, an electronic effect of Au appears to be a most important driver of the enhanced activity in the B2R2 catalyst. In the case of the most active B1NR catalyst, highly dispersed Au metal plays a key role in the higher catalytic activity, likely providing synergetic interactions between the metals and an increased total number of very active Au sites. The combination of these effects result in increased TOF. Overall, the results indicate that the proper addition of Au to Ir can boost the activity for CO oxidation. While the DMN methodology clearly provides a measure of control over eventual catalyst performance, other synthetic methods for preparation of Ir-based bimetallics are being pursued in our laboratory to provide more systematic exploration of these effects.

CHAPTER 4

KINETIC EVALUATION OF DIRECT NO DECOMPOSITION AND NO-CO REACTION OVER DENDRIMER-DERIVED BIMETALLIC IR-AU/AL_2O_3 CATALYSTS

This chapter presents the effect of Au on the catalytic performance of Ir metal towards NO reduction by CO and direct NO decomposition. It has been investigated over dendrimer-derived Ir-Au bimetallic catalyst. Results were also compared to a catalyst prepared by conventional incipient wetness impregnation of metal salts. Characterization of Ir-Au bimetallic samples using scanning transmission electron microscopy, H_2 chemisorption and temperature programmed desorption of NO reveals that highly dispersed Ir-Au particles can be obtained by dendrimer templating method. In-situ transmission Fourier transform infrared spectroscopy following adsorption of probe molecules (i.e., CO and NO) on the dendrimer-derived Ir-Au bimetallic sample indicated the presence of electron transfer from Ir to Au sites. In contrast, a geometric effect of Au on Ir was observed over the conventional-derived sample, consistent with X-ray photoelectron spectroscopy measurements. These properties influence the catalytic performance, with higher selectivity towards N_2O and a better intrinsic catalytic turnover frequency for reduction of NO by CO and NO decomposition observed for the dendrimer-derived sample. Overall, the results suggest that both NO-CO and NO decomposition reaction are structure-sensitive reactions.

4.1 INTRODUCTION

The exhaust gases from automobile engines and industrial plants contain mainly oxides of carbon (CO and CO_2) and nitrogen (NO_x), hydrocarbons (HC), sulphur dioxide (SO_2), particulates and soot. One of the most urgent problems is removal of NO_x, typically produced during high-temperature combustion, which contributes to formation of smog and ground-level ozone by reacting with hydrocarbons in the presence of sunlight. More stringent NO_x emission requirements are being issued every day, necessitating development of more effective catalytic NO_x abatement technologies. Direct NO decomposition to N_2 and O_2 (without an added reductant) is an attractive alternative to NO_x traps and selective catalytic reduction for this application [106]. Thermodynamically, NO_x is unstable and tends to decompose through reactions such as

$$NO \leftrightarrow \tfrac{1}{2} N_2 + \tfrac{1}{2} O_2 \quad \Delta G_f^0 = -86 \;\; KJ \;\; mol^{-1} \qquad [4.1]$$

The equilibrium concentration of nitric oxide in the air is high at elevated temperatures (for example, $2x10^4$ ppm at 2273 K), but decreases with the temperature (less than 200 ppm at T < 1273 K). Therefore, a direct decomposition reaction at moderate temperature should be an attractive method for NO_x abatement. However, the obstacle in using reaction (1) for the NO_x emission control involves finding a proper catalyst for decreasing its huge energy barrier (E_a = 364 kJ mol $^{-1}$) [107].

Supported Group VIII metals, such as Pt, Pd, Rh and Ir exhibit varying degrees of NO decomposition activity, albeit at high temperatures (600-800 ℃) [108-110]. Supported Pt and Pd exhibited good initial decomposition activity; however, they deactivate rapidly at low temperatures due to oxygen poisoning [108, 111]. Ir, on the

other hand, exhibits superior ability to convert NO under oxidizing conditions. Tauster and Murrell [112] were the first who studied NO reduction by CO with Ir catalysts. They showed that Ir is the only noble metal favoring the NO-CO over the CO-O_2 reaction in the presence of O_2. Absorbed oxygen on Ir was the predominant surface species and its reaction with gaseous CO generated free surface sites. These sites were available for the chemisorption of NO and O_2. Taylor and Schlatter [113], who studied NO reduction by CO in the presence of O_2 over alumina-supported Ir, Rh, Pt and Pd catalysts, confirmed these results. The high effectiveness of Ir compared to the other metals was attributed to its ability to adsorb NO dissociatively in the presence of excess O_2.

Recently, an increasing number of studies have shown the advantage of the use of bimetallic clusters, which often provide enhanced selectivity, stability, and/or activity, in catalysis [114-119]. Among them, Peng et al. and Wang et al. reported the benefit of the addition of other elements to the Pd active site through the formation of bimetallic clusters in the activity of CO oxidation [118, 119]. They especially focused on Au [118] and Ag [119] as additives, since these are elements with high resistance to oxidation might keep nearby Pd metal atoms in their metallic state. Here, the combination of Au or Ag with Ir would also be beneficial and therefore Au was selected as an additive and Ir-Au bimetallic clusters were examined for NO decomposition.

Different Ir-based catalysts have been recently prepared and tested [120-129], with most studies revealing that the effect of the size of Ir particles on the deNOx activity was crucial [125-129] and related [112, 113, 130] to the competitive reactions of CO with NO and CO with O_2. Activation of the Ir catalysts was achieved by high temperature pretreatments [122, 123, 131] or by in situ activation during catalytic tests [125, 126].

Both methods led to crystallite growth and a coexistence of Ir and IrO_2 [125, 128]. Thus, size control of Ir-based catalysts is needed to achieve optimal performance for the simultaneous reduction of NO and CO emissions.

In order to obtain size-controlled uniform materials, several synthetic techniques have been developed over the years including the use of polymers, surfactants, well-defined organometallic cluster complexes, size-selected metal clusters and ionic liquids. One recent method that has received considerable attention is the use of dendrimer-metal nanocomposites (DMNs) as precursors [7]. Dendrimers [16, 132] are monodisperse, hyperbranched spherical polymers that emanate from a central core with repetitive branching units, allowing for controllable size. While possessing a very dense exterior, they contain less dense interiors that can be ideal for encapsulation of metal nanoparticles. The use of dendrimers as templates/stabilizers for synthesis of nanoparticles is a relatively new but active field. There are now many investigations exploring the use of DMNs as precursors to synthesize supported catalysts, and narrow metal particle size distributions have been observed for different transition metals such as Pt, Pd, Au, Ru, Cu, Pt-Pd, Pt-Au, Pd-Au, and Ag-Au catalysts (see for example [17, 18, 28, 58-61, 133, 134]. Most recently, we found that dendrimer-derived Ir-Au bimetallic catalyst with higher dispersion compared to conventionally derived catalyst resulted in an enhanced activity for the CO oxidation reaction [135].

The scope of the present work is to characterize a series of Ir-Au catalysts in order to derive relations between physicochemical and catalytic properties for NO reduction and CO oxidation and for direct NO decomposition. It was found that dendrimer-derived bimetallic catalyst (Ir-Au-DD) exhibited highly dispersed metal nanoparticles and narrow

size distribution when compared with conventionally prepared sample (Ir-Au-CD). However, Ir-Au-DD showed similar activity for the NO-CO and direct NO decomposition reactions compared with Ir monometallic catalyst, whereas an enhanced activity was found on Ir-Au-CD.

4.2 EXPERIMENTAL

Fourth generation hydroxyl-terminated poly(amido)amine (PAMAM) dendrimer (G4OH) (10 wt% in methanol solution) was obtained from Aldrich. Prior to use, an aqueous solution was made by evaporating methanol with flowing N_2 and diluting the residue to 1.7×10^{-4} M with deionized water. $IrCl_3\cdot3H_2O$ (AlfaAesar), $HAuCl_4$ (Aldrich) and $NaBH_4$ (granules, 99.995%, Aldrich) were used as received. Deionized water (18 MΩ•cm Milli-Q) was used to prepare all the aqueous solutions. A gamma-delta-theta phase alumina (specific surface area =104 m^2/g, pore volume = 0.9 mL/g) was provided by Toyota. NO, CO, O_2 (UHP), He (UHP) and H_2 (UHP) were supplied by Airstar.

The synthesis of dendrimer-metal nanocomposites was adapted from the literature [19, 136-138] and has been published previously [139]. A proper amount of 8.0×10^{-3} M $IrCl_3\cdot3H_2O$ precursor solution was added under N_2 purging to G4OH dendrimer solution with the concentration of 1.7×10^{-4} M to reach a molar ratio of Ir^{3+} to G4OH of 20:1. The mixed solution was stirred for 7 days at room temperature with N_2 flowing to protect the Ir^{3+} ions from oxidation by dissolved O_2 and allow the complexation of Ir^{3+} ions with the functional groups in G4OH dendrimer. The formation of dendrimer encapsulated metallic Ir nanoparticles in solution was attempted by adding a 10-fold excess solution of $NaBH_4$

at room temperature. The supported catalyst was made by standard wet impregnation of the reduced dendrimer-Ir nanocomposite onto Al_2O_3, to a nominal Ir loading of 1.0 wt % (Ir-DD). The extra water was removed under ambient conditions by evaporation of the stirring slurry for 3 days. The same procedure was used to make dendrimer-Au monometallic nanocomposites except allowing complexation time of 2 minutes, with the corresponding supported catalyst having a nominal Au loading of 1.0 wt% (Au-DD).

The sequential method was followed for bimetallic Ir-Au DMNs, which involved first mixing Ir metal precursor solution with dendrimer solution for 7 days under N_2 purging. Then, Au metal precursor solution was added, whereupon complexation occurred (for a short period, order of minutes). In this case, the target ratio of each type of metal atom to dendrimer was 20 to 1, thus making a total metal atom loading of 40 atoms per dendrimer. Finally, these bimetal-dendrimer complex nanocomposites were impregnated onto alumina as described above, with the nominal loading of 1.0 wt% Ir and 1.0 wt% Au (Ir-Au-DD).

Conventional Ir and Au catalysts were made by incipient wetness method (Ir-CD and Au-CD). A proper amount of 5.78×10^{-2} M of $IrCl_3\cdot3H_2O$ precursor solution was added dropwise to Al_2O_3 and the resulting slurry was dried in an oven at 80°C for overnight before use. A conventional Au catalyst was made with exactly the same protocol. In the case of conventional Ir-Au bimetallic catalyst (Ir-Au-CD), equal volumes of 11.56×10^{-2} M of $IrCl_3\cdot3H_2O$ and $HAuCl_4$ precursor solutions were mixed together and then added to the Al_2O_3. The nominal metal loadings of all the conventional catalysts were the same as their DMN-derived analogues.

All catalysts studied were activated under flowing O_2 treatment at 350 °C for 30 min and H_2 treatment at 400 °C for 1 hour with a slow temperature ramp rate of 5 °C /min followed by cooling to room temperature. This activation protocol was adapted for consistency from a previous study [139] which showed that G4OH dendrimer template could be sufficiently decomposed on an γ-Al_2O_3 support to expose the metal nanoparticles.

4.3 RESULT AND DISCUSSION

4.3.1 PARTICLE SIZE, DISTRIBUTION AND COMPOSITION

The average particle sizes and metallic dispersions were determined by electron microscopy and H_2-chemisorption after activation using both treatment protocols (Table 4.1). STEM analysis and H_2-chemisorption data for alumina supported monometallic Ir and Au were reported before [135]. The Au monometallic catalysts exhibit a volume-to-surface mean diameter (VSMD) [84] that is much larger than the Ir monometallic catalysts (Table 4.1). The difference in average particle size between Ir and Au suggests that the latter has higher mobility on the alumina support than the former at the elevated oxidation and reduction temperatures used here. This in turn leads to more extensive sintering of Au nanoparticles. On the other hand, Ir-Au-CD and Ir-Au-DD bimetallic catalysts have smaller VSMDs than the Au monometallic catalysts (i.e., below 4 nm). Thus, it appears that the presence of Ir at these ratios prevents the sintering or agglomeration of Au. Atomic absorption spectroscopy analysis shows that there is no significant different between these two bimetallic catalysts in terms of the actual metal

weight loading on alumina support. The loadings are similar to the nominal values and expected Ir to Au ratio (within the error of the measurement).

Table 4.1. Metal particle size measured by STEM, dispersion by H_2 chemisorption, actual metal loading and bulk composition

Catalysts	Mean Diameter (nm)	Volume-to-surface Mean Diameter[a] (nm)	Dispersion [b] (%)	Metal Weight Loading[c]		Bulk Composition [c]	
				Ir (%)	Au (%)	Ir (%)	Au (%)
Ir-CD	1.0±0.2	1.1±0.1	74±7	1.0	–	100	–
Ir-DD	2.0±0.4	2.1±0.1	65±9	1.0	–	100	–
Ir-Au-CD	1.5±2.4	3.1±0.8	10±1	0.9	1.0	48	52
Ir-Au-DD	1.5±0.3	1.6±0.1	43±3	1.0	1.0	50	50
Au-CD	4.9±7.6	18.5±1.6	–	–	0.9	–	100
Au-DD	9.6±3.4	9.8±0.9	–	–	0.7	–	100

[a]Calculated using $\overline{D} = \sum_{i}^{N} N_i D_{p,i}^3 / \sum_{i}^{N} N_i D_{p,i}^2$, where N_i is number of particles and $D_{p,i}$ is the measured diameter from STEM images [84].

[b] Obtained by H_2 chemisorption analysis. (H per Ir metal).

[c]Obtained by elemental analysis.

However, it was noticed that the morphology of these two bimetallic catalysts varies with different methods as shown in Figure 4.1A and B. The conventional catalyst (Ir-Au-CD) has an asymmetric distribution with most (91 %) of the particles between 0.5-2 nm and the remaining 9 % of particles spread out between 2-6 nm creating a broad particle size distribution. In contrast, in the Ir-Au-DD catalyst, very narrow particle size distribution with a more symmetric distribution was observed and no particles larger than 3 nm were observed. It is apparent that the conventional Ir-Au catalyst has a larger

volume-surface mean diameter (3.1 ± 0.8 nm) with lower dispersion (10%) and broader size distribution than the dendrimer-derived Ir-Au catalysts with VSMD of 1.6 ± 0.1 nm and 43% dispersion, as listed in Table 4.1. This implies that G4OH PAMAM dendrimer exerts control over particle formation.

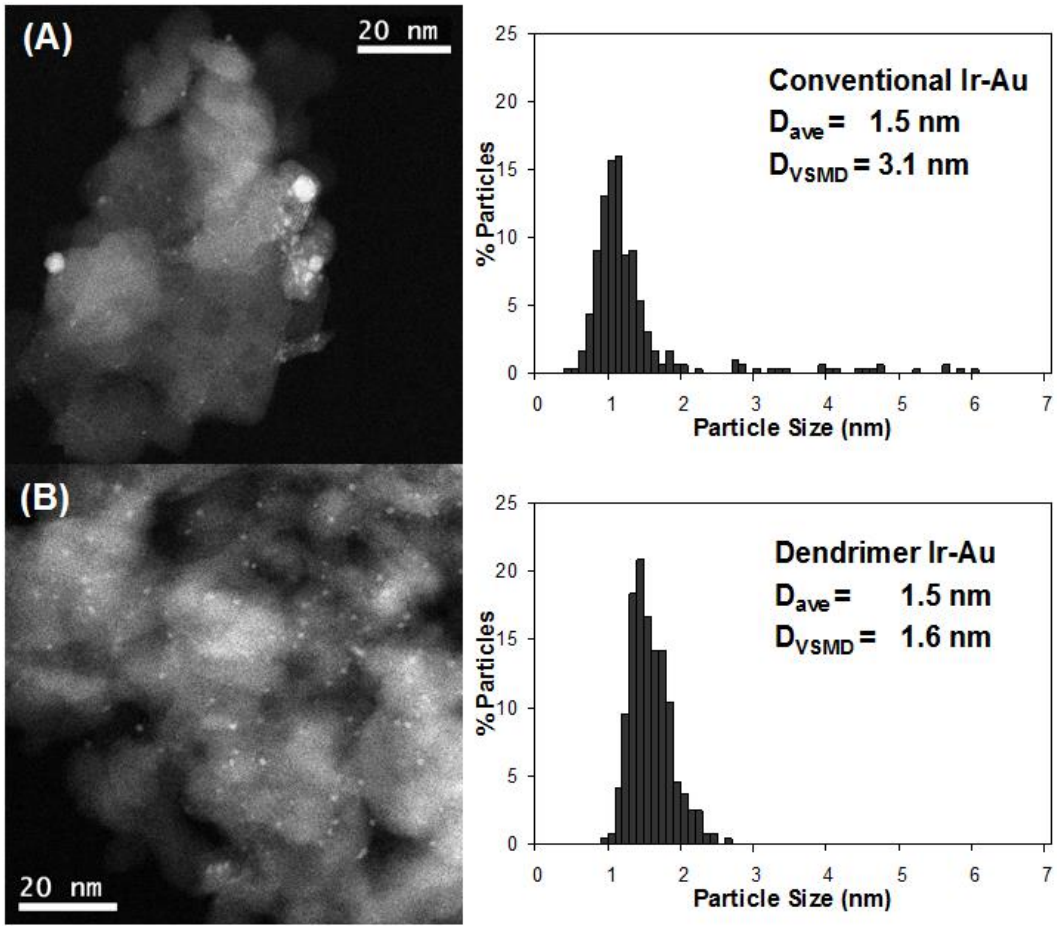

Figure 4.1. STEM images and size distributions for A) Ir-Au-CD and B) Ir-Au-DD.

Although there is relatively little effect on controlling particle sizes when dendrimer precursors are used to prepare 1.0 wt.% Ir monometallic catalyst, DMN precursors do appear to play a role in controlling the sintering/agglomeration processes of

Ir-Au bimetallic and Au monometallic nanoparticles over alumina, thus influencing particle size and size distribution. This has been observed previously for other metals such as ruthenium and rhodium [19, 82, 137].

Figure 4.2 shows the Ir 4*f* and Au 4*f* regions of the Ir-Au bimetallic samples that were investigated before and after NO decomposition reaction by XPS. All the spent bimetallic samples for NO decomposition reaction were re-reduced at 400 ℃ in the XPS main chamber for in situ sample pretreatment. The theoretical separations of the spin-orbit split components were 3.0 eV for Ir 4*f* and 3.7 eV for Au 4*f*. The full width at half maximum (FWHM) values of the 4*f* 7/2 and 4*f* 5/2 peaks were assumed to be identical. These fitting parameters were used in all the cases below for the metal peaks in spectra containing metal and/or oxide.

In Figure 4.2A, the dendrimer-derived sample shows a broader band envelope compared to the conventional-derived sample, with four peaks at binding energies of 61, 62, 64 and 65 eV. The broader envelope corresponds to the relatively higher binding energies of 62 and 65 eV, which are associated with IrO_2. This suggests that it is harder for the dendrimer-derived sample to be reduced than for the conventionally derived sample under the same pretreatment protocol. These oxidation peaks were gone for the spent catalysts of NO decomposition reaction after re-reduction step as shown in Figure 4.2C. More interestingly, the Au 4*f* region for the conventional-derived sample shows greatly increased signal compared with Ir 4*f* signal, while the Au 4*f* signal of Ir-Au-DD is similar to or a little smaller than Ir 4*f* in terms of their intensities. This implies that these two samples that were synthesized different ways have different surface composition

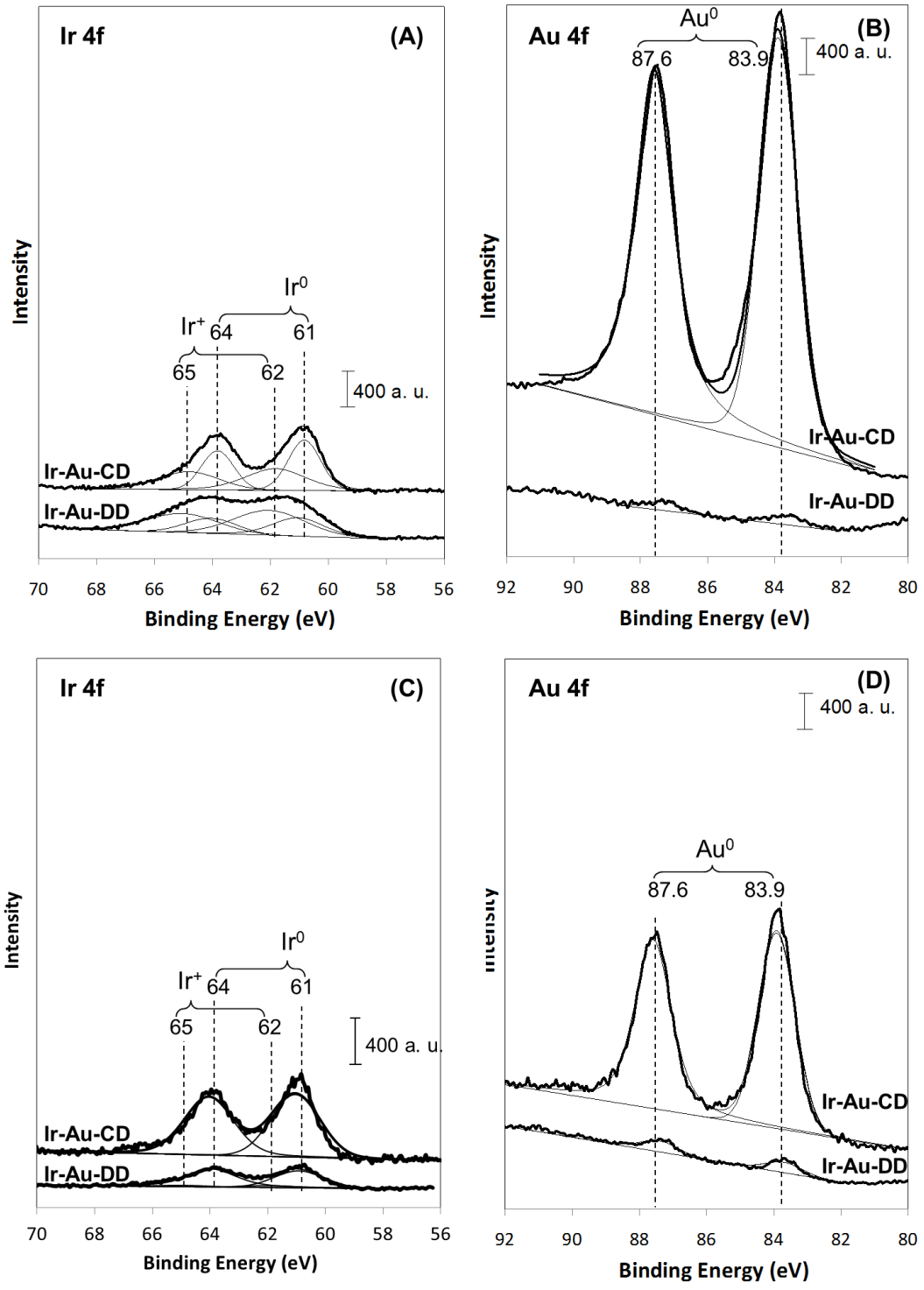

Figure 4.2. XPS data for oxidation state of Ir and Au on Ir-Au-CD and Ir-Au-DD before (A, B) and after (C, D) NO decomposition reaction.

even though the bulk composition are similar each other based on the AA analysis. This might indicate that in the case of Ir-Au-CD, the Au is enriched on the surface by agglomeration of Au over Ir. Such an agglomeration of Au also affects the dispersion of Ir-Au-CD sample and leads to much lower dispersion when compared to Ir-CD (Table 4.1). Thus, the number of Ir active sites of the surface was significantly decreased by the presence of Au metal atoms. On the other hand, for Ir-Au-DD, it seems to have relatively well mixed surface of Ir and Au. Thus, this difference would be expected to affect the performance of the catalyst in the reactions.

4.3.2 Infrared Spectra of Adsorbed NO and CO

Infrared spectra collected following the adsorption of NO and CO at room temperature on the Ir monometallic and the Ir-Au bimetallic samples are shown in Figure 4.3. In our previous work, we found that there are no characteristic ν_{NO} vibrations or ν_{CO} vibrations in the spectra of the Au-CD and Au-DD samples, which had an average Au particle size of approximately 19 and 10 nm (Table 1) [135]. This result is consistent with previous literature reports demonstrating that the adsorption of CO on Au depends on the particle size of the Au crystallites and is observed only on Au nanoparticles with sizes below 5 nm [140-142].

When the conventional and dendrimer-derived Ir monometallic samples were exposed to NO under similar conditions (Figure 4.3A), three strong bands were observed at 1829, 1887 and 1956 cm^{-1} which can be assigned as linearly adsorbed NO on fully reduced Ir sites or on oxidized Ir sites, as listed in Table 4.2 [126, 143, 144]. In the same way, three strong bands were observed at 2008, 2040 and 2074 cm^{-1} for the CO adsorption on two Ir monometallic samples (Figure 4.3B). However, there are several

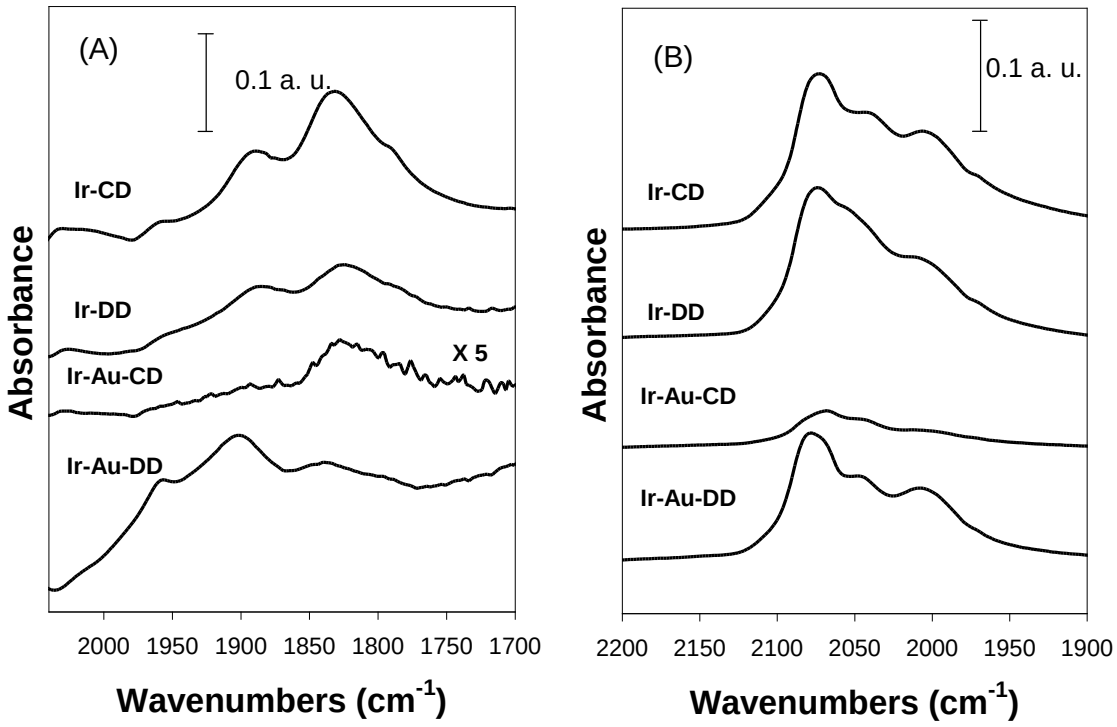

Figure 4.3. FTIR results for A) NO adsorption and B) CO adsorption on Ir monometallic and Ir-Au bimetallic catalysts.

Table 4.2. NO and CO adsorption wavenumber (cm^{-1}) of all catalysts

Catalysts		Linealy adsorbed NO		Linealy adsorbed CO	
		Ir^0–NO	Ir^+–NO	Ir^0–CO	Ir^+–CO
Conventional-Derived	Ir-CD	1829,1887	1956	2035,2053	2092
	Ir-Au-CD	1821,1880	1949	2027,2046	2083
Dendrimer-Derived	Ir-DD	1828,1885	1954	2034,2054	2093
	Ir-Au-DD	1844,1899	1963	2041,2063	2098

peaks involved between 2000 and 2100 cm^{-1} and can generally be assigned to linearly adsorbed CO species on fully reduced Ir sites (2035, 2053cm^{-1}) or on partially oxidized Ir sites (2092cm^{-1}) or antisymmetric (2012cm^{-1}) or symmetric (2078 cm^{-1}) vibrations of adsorbed dicarbonyl species on Ir ions (see Figure 4.4 for detail). The assignment of these

peaks in this small region is based on our previous published work [136] and the available literature [93, 94, 97, 98, 143, 145-149].

In order to investigate the effect of Au on both conventional and dendrimer-derived bimetallic samples, the same FTIR experiment was carried out and the results are listed in Table 4.2 after the curve fitting. For the conventional bimetallic sample, it was clearly noticed that the intensity of spectra for both NO and CO adsorption were considerably depressed compared to the Ir monometallic sample. Also, a comparison of the spectrum characterizing the Ir-Au-CD sample with the one obtained for Ir-CD indicates that in this case the ν_{NO} and ν_{CO} bands were shifted to the lower wavenumbers by 7-8 cm^{-1}. Such a shift could be related to a variety of different reasons. The dispersion of metal for example, can play a role as it was observed earlier [94, 147, 148]. Indeed, the STEM data show that after oxidation/reduction treatment the Ir-Au-CD sample had a larger average metal particle size when compared to Ir-CD (Table 4.1). However, in this case, a blue shift in the ν_{CO} would be expected due to the increased coordination number of the surface Ir atoms in large particles, leading to the reduction of back-donation of electrons into the antibonding molecular orbitals of CO [93], which contradicts our observations. Another possible explanation could be related to a geometric effect, caused by a dilution of Ir surface sites by Au. If such dilution was to take place, the decreased dipole-dipole coupling between adsorbed CO molecules would result in a red shift in the ν_{CO}, consistent with our observations as well as the decreased peak intensities. The general behavior of NO during the adsorption on metal surfaces and the formation of M–NO bonds can be interpreted using the same arguments as proposed for the adsorption of

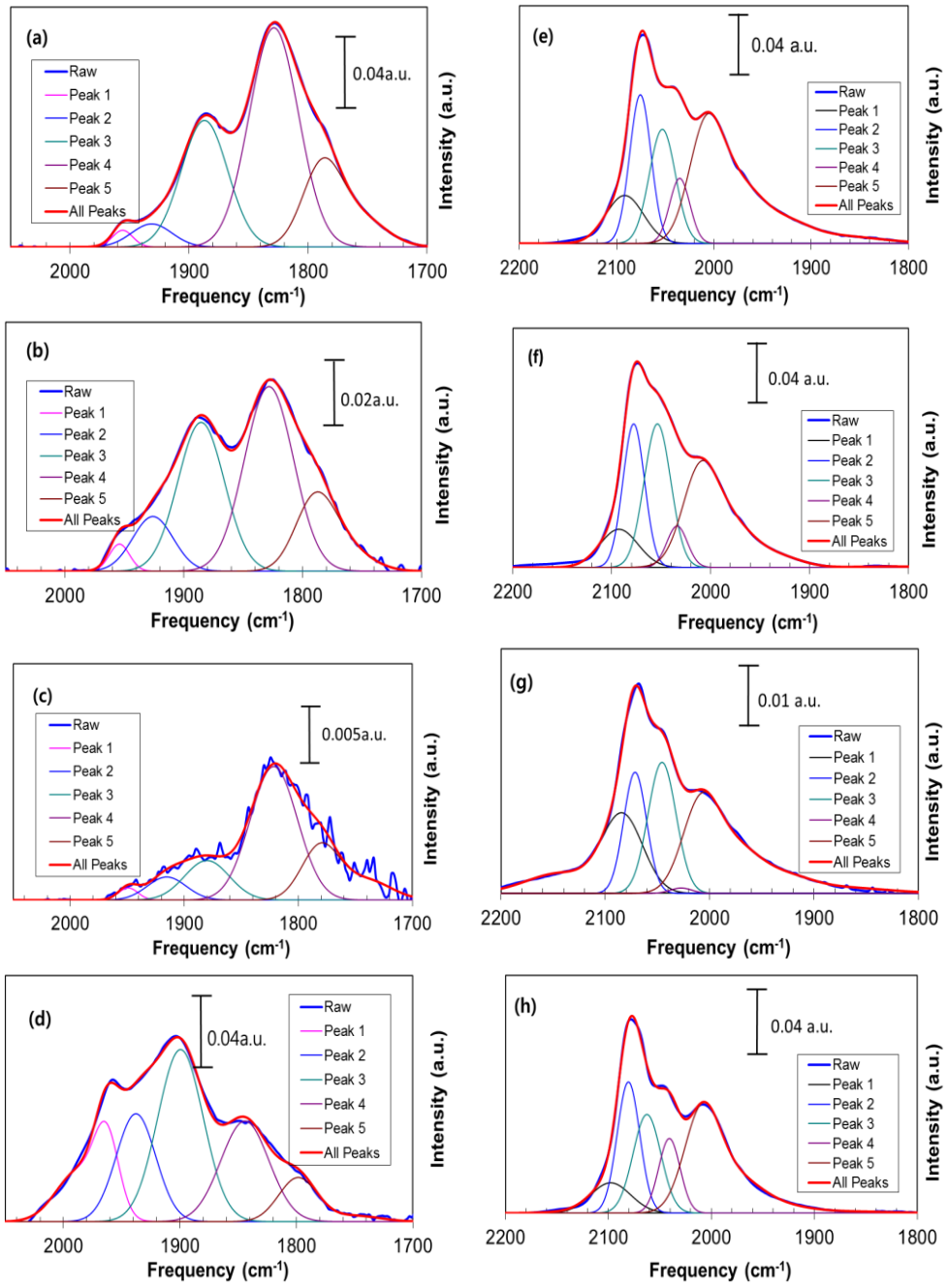

Figure 4.4. FTIR-NO adsorption and peak fitting for (a) Ir-CD, (b) Ir-DD (c) Ir-Au-CD, (d) Ir-Au-DD and FTIR-CO adsorption and peak fitting for (e) Ir-CD, (f) Ir-DD (g) Ir-Au-CD, (h) Ir-Au-DD . (Linearly adsorbed NO or CO species on partially oxidized Ir sites (Peak 1) or on fully reduced Ir sites (Peak 3, 4) or symmetric (Peak 2) or antisymmetric (Peak 5) vibrations of adsorbed dicarbonyl species on Ir ions.)

CO [150]. This is because the similar distribution of electrons in CO and NO allows the use of both molecules to probe metal surfaces. Moreover, because NO has an extra electron occupying the $\pi*$ antibonding molecular orbital, it can be more sensitive to the electronic state of the adsorbate; in this orbital, even slight changes in the electron density noticeably change the frequency of the ν_{NO} vibrations [150]. The dilution of Ir surface sites by Au in the Ir-Au-CD sample can also explain the surface enrichment of Au that was observed in the XPS analysis.

When similar FTIR experiments were repeated with the dendrimer-derived bimetallic samples, on the other hand, there were no significant changes in the band strength in the spectra of NO and CO adsorption compared to the monometallic sample. These peak intensities could be related to Ir active sites exposed to the surface, indicating that Ir active sites on the surface of the Ir-Au-DD sample are not significantly decreased by the presence of Au metal atoms. This is consistent with our XPS result for the Ir and Au surface analysis. However, in the presence of Au in the bimetallic sample, the peak positions were different from the monometallic sample, with blue shifts in the ν_{NO} and ν_{CO} bands listed in Table 4.2. Since it was confirmed that the Ir-Au-DD sample had a smaller particle size than Ir-DD sample by STEM data, the dispersion of the metal is not the reason for the peak shift. Thus, the possible explanation for the shift could be an electronic effect caused by net electron transfer from Ir to Au. For example, such a transfer would result in a decrease in back-donation of electrons into the antibonding molecular orbitals of CO, resulting in a blue shift in ν_{CO}. Also, the position of ν_{NO} band shifted to higher wavenumbers in the Ir-Au-DD sample, similar to what was observed

during the adsorption of CO on the same sample. This once again suggests that the electronic property of Ir was significantly affected by Au in the bimetallic sample.

4.3.3 Catalytic Reduction of NO with CO

In order to evaluate catalytic activity of the catalysts, the NO-CO reaction was tested. As a result, light-off curves showing the temperature dependence of NO conversion for the NO-CO reaction over conventional and dendrimer-derived Al_2O_3-supported Ir-Au catalysts are shown in Figure 4.5. As references, Ir and Au monometallic catalysts were also investigated. Since the CO is not labeled with ^{13}C isotope, we could not differentiate the N_2 formed and the CO consumed simultaneously, owing to the same mass numbers of N_2 and CO (*m/e* = 28). The same situation exists for CO_2 and N_2O (*m/e* = 44) and for NO and NO_2 (*m/e* = 30). In spite of this, we can still compare the de-NOx activity of the Ir-Au bimetallic with that of Ir or Au monometallic catalysts from the decrease in NO concentration by following m/e = 15. In general, similar NO conversion behaviors were observed with conventional Ir and dendrimer-derived Ir catalysts, except that Ir-DD showed slightly higher NO conversion than Ir-CD above 350 ℃. This indicates that the dendrimer templating approach does not play a significant role in this case. These catalytic performances were much better than that achieved over Au monometallic catalysts according to the higher NO conversion at the same reaction temperature for this NO-CO reaction (e.g., about 60 % for Ir and below 5 % for Au monometallic samples at around 300 ℃). However, they cannot be simply compared to each other because the catalytic activity is dependent on various factors such as nature of the material and support, kind of precursors or size of metal, etc. Thus, it should be noted

that Au monometalic samples have much larger particle size than the Ir monometallic samples, and such a poor control of the particle size may have led to low activity for the NO-CO reaction.

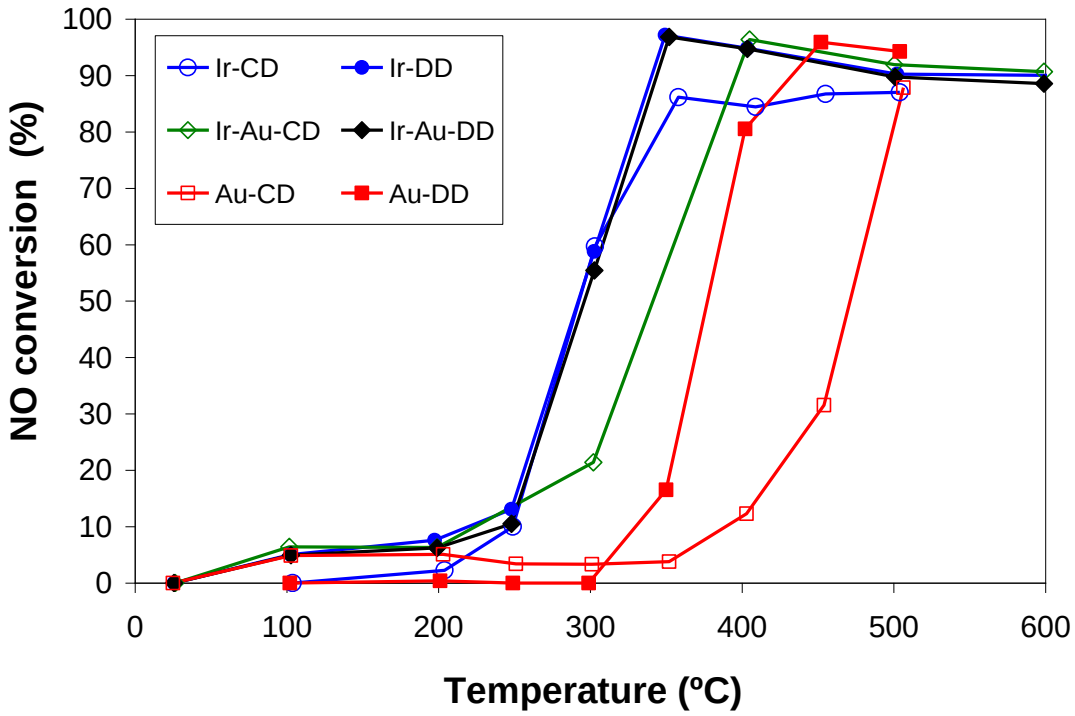

Figure 4.5. NO-CO light-off curves for CD and DD catalysts.

It has been reported that use of a secondary metal such as Au and Ag enhances activity for nitric oxide decomposition over supported Pt-group metals [151]. Furthermore, Qun and co-workers have demonstrated that Ir-based bifunctional catalyst can not only improve the catalytic performance but also enhance the stability under the strict conditions for direct and NO-assisted N_2O decomposition [152]. However, unlike our expectations, none of the bimetallic catalyst prepared in our work showed enhanced performance compared with the Ir monometallic catalyst. That is, almost the same catalytic performance was obtained on Ir-Au-DD as for Ir-DD, while the Ir-Au-CD

showed even lower NO conversion than Ir-CD catalyst at the same reaction temperature (i.e., about 60 % and 20 % for Ir-Au-DD and Ir-Au-CD sample, respectively, at around 300 ℃). On the other hand, the dendrimer-derived samples such as Ir-Au-DD or Au-DD showed better catalytic activity than conventional Ir-Au-CD or Au-CD samples, respectively. This indicates that the dendrimer approach is an effective way to control Au metal size of the catalyst and can result in the improvement in catalytic performance. Such a conclusion is consistent with the STEM data as well as metal dispersion data presented above (see Figure 4.1 and Table 4.1).

Figure 4.6 reveals the relationship between dispersion and average particle size of the catalysts, and catalytic activity for NO-CO reaction, represented as T_{50} (i.e., temperature at 50 % NO conversion) from the NO-CO light off curves. Previously, Davis and co-workers [153] have investigated the correlation between the Pd particle size and the catalytic activity toward the NO-CO reaction. In their work, it was found that Pd particles of 1 nm average diameter were more active for the NO-CO reaction than 4.5 nm Pd particles. In our work, although we are considering not just monometallic but bimetallic samples as well, it also seems that the catalysts with higher dispersion or with smaller particle size showed lower T_{50} values for the NO-CO reaction, as shown Figure in 4.6A and 6B.

4.3.4 Catalytic Direct NO Decomposition

Figure 4.7 shows light-off curves for direct NO decomposition with low gas hour space velocity of 5,000 h^{-1} over conventional and dendrimer-derived Al_2O_3-supported Ir-

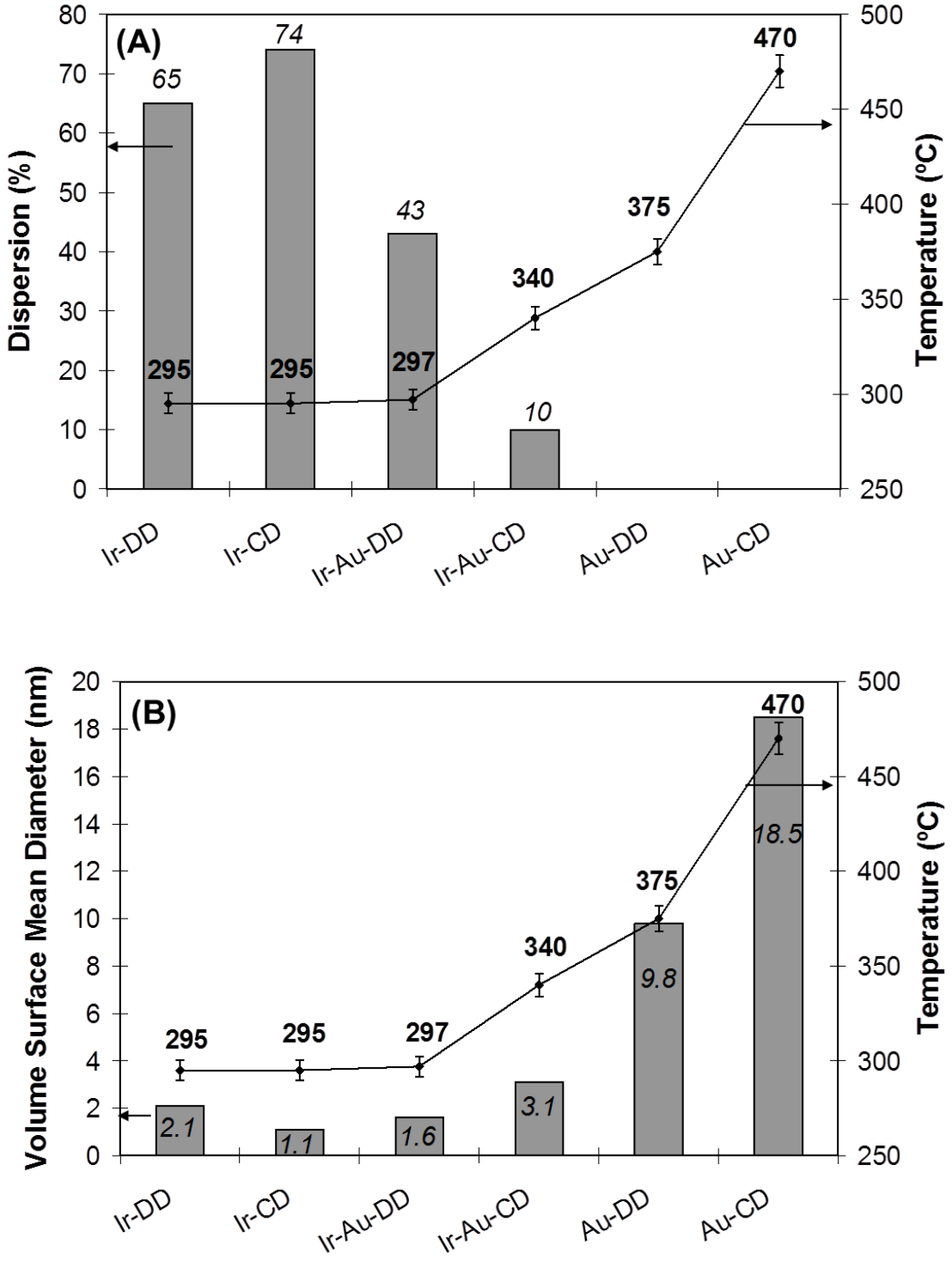

Figure 4.6. Effect of dispersion and particle size of catalysts on T_{50} for NO-CO reaction.

Au bimetallic catalysts, Ir and Au monometallic catalysts and Al_2O_3 support. All the NO conversions under these reaction conditions were lower than 30% up to 500 ℃. The general activity trend was similar to that obtained for the NO-CO reaction. That is, Ir monometallic catalysts showed the best catalytic activity over almost the entire reaction temperature range. Conventional and dendrimer-derived Ir-Au bimetallic catalysts followed, and then very low activities (i. e., below 5 % of NO conversion) were achieved over Au monometallic catalysts. Such a low NO conversion obtained on Au monometallic catalyst was almost the same as activity over support by itself, indicating that Au metal atoms were inactive for direct NO decomposition. The light-off curves characterizing both the conventional and dendrimer-derived Ir-Au catalysts were slightly

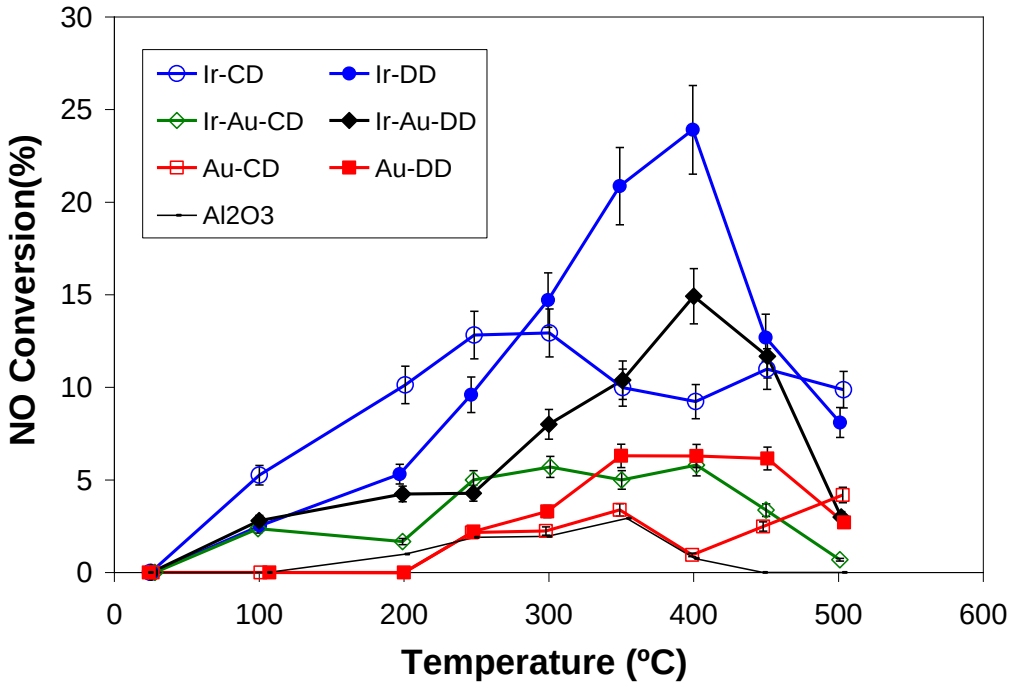

Figure 4.7. NO decomposition light-off curves for CD and DD catalysts.

better than that of Au monometallic and worse than that of Ir monometallic sample. This also indicates that the presence of Au in this sample has no substantial effect on Ir activity; Au rather remains as an inactive material.

In order to make clear the relationship between the catalytic performance and the adsorption behaviors of the Ir-Au bimetallic catalysts, we carried out TPD of NO over the bimetallic samples, and then made comparison with the TPD results over the Ir monometallic catalysts, as illustrated in Figure 4.8. It can be seen that the amounts of NO desorbed from the Ir-based catalysts (Fig. 4.8A-D), especially, Ir-Au bimetallic samples, are higher than that from the Au-DD (Fig. 4.8E) or Al_2O_3 (Fig. 4.8F), indicating that the Ir-based catalysts have stronger ability for NO adsorption than Au metal catalyst or alumina support. Although the amount of NO desorption from Ir-CD and Ir-Au-CD are similar to the Ir-DD and Ir-Au-DD, respectively, it seems that the desorption profiles of other molecules are different between them. When we compare the peaks of *m/e* = 44, which correspond to the amount of N_2O formed, it is clear that the N_2O formation peaks over the dendrimer-derived samples are sharp and high at around 325 °C, whereas, over conventional-derived samples, they are relatively broader and smaller. Moreover, accompanying N_2O formation, N_2 was also formed on these catalysts (indicated by the peaks of *m/e* = 28). However, the observed N_2 formation peaks were much smaller than N_2O formation peaks over these samples. It is known that the N_2 as well as N_2O formation in this case is via the following paths [154]:

$$NO + * \rightarrow NO* \quad [4.2]$$
$$NO* \rightarrow N* + O* \quad [4.3]$$
$$N* + N* \rightarrow N_2 + 2* \quad [4.4]$$
$$N* + NO* \rightarrow N_2O + 2* \quad [4.5]$$

$$O^* + O^* \rightarrow O_2 + 2^* \qquad [4.6]$$

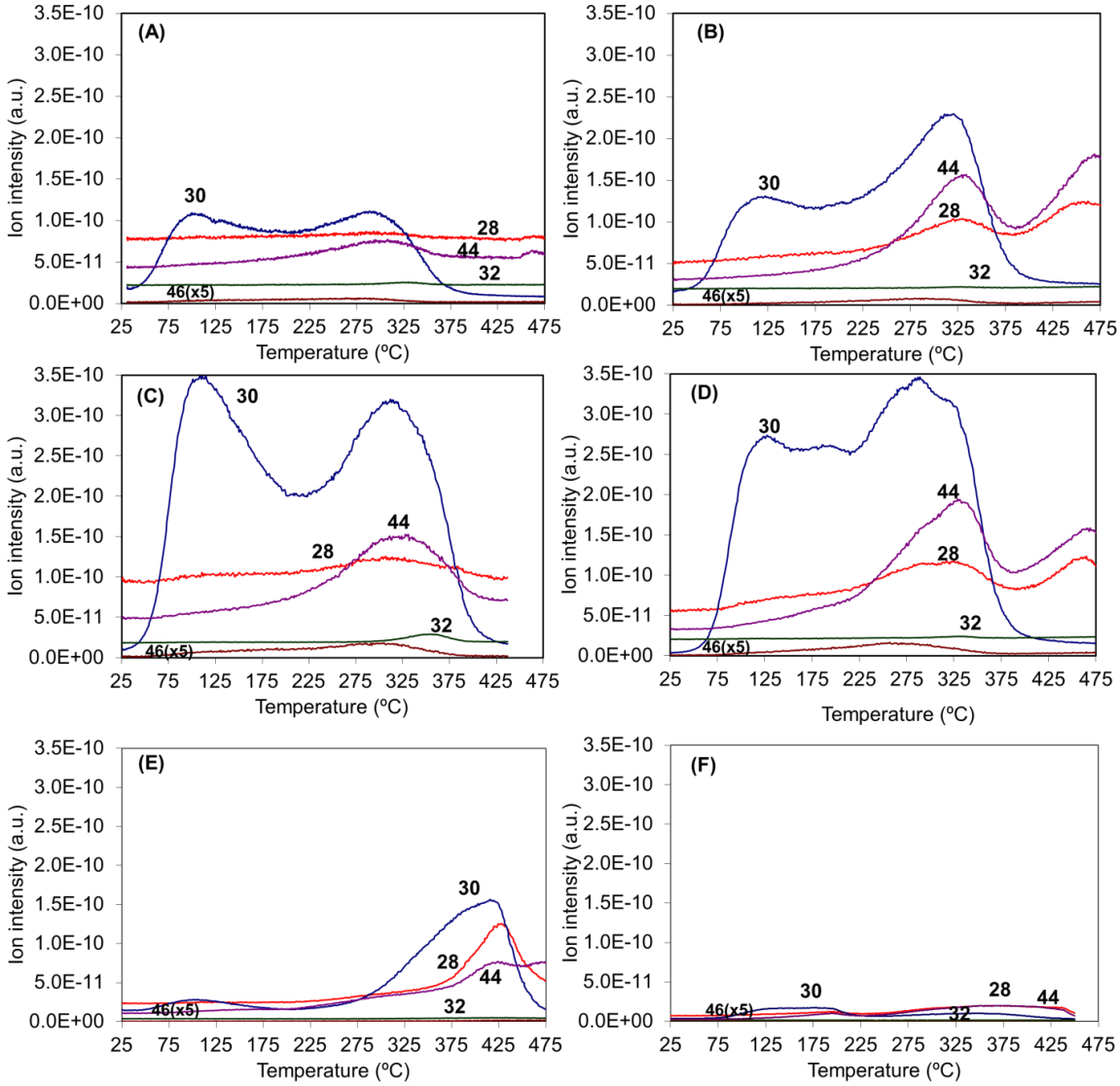

Figure 4.8. NO-TPD over A) Ir-CD, B) Ir-DD, C) Ir-Au-CD, D) Ir-Au-DD, E) Au-DD catalysts and F) Al_2O_3 support; *m/e*: 30 NO, 32 O_2, 28 N_2, 44 N_2O and 46 NO_2.

According to the above mechanism and NO-TPD results over the Ir-Au bimetallic catalysts, it can be concluded that NO dissociation on the surface of a catalyst is considered to be the key step.

It should be mentioned that, different from N_2 desorption, the desorption of O_2 (corresponding to *m/e* = 32) was not detected well in this case, probably because oxygen was more strongly bound on the catalyst surfaces than N_2. The same phenomena were also observed by Shi et al [155].

4.3.5 Catalytic Activity

In order to investigate the intrinsic activity of Ir and elucidate further the effect of Au on catalytic performance, the turnover frequencies (TOFs) were calculated as a function of different reaction temperature over the conventional and dendrimer-derived Ir-Au bimetallic catalysts and the Ir monometallic catalysts for both the NO-CO reaction (Figure 4.9A) and direct NO decomposition (Figure 4.9B), respectively. These TOFs were expressed as mole of NO reduced to N_2 and N_2O per mole of surface iridium atom and per minute, as listed in Table 4.3 and 4. Since NO conversions were higher than 30 % above 300 ℃, only the reaction temperature up to 250 ℃ was considered for TOFs of NO-CO reaction, whereas the entire reaction temperature region up to 500 ℃ was considered for direct NO decomposition.

For the NO-CO reaction, it was interesting that the TOF gradually increased with decreasing iridium dispersion, irrespective of the catalysts, at the same reaction temperature. The Ir-CD sample with the highest iridium dispersion, D_{Ir} = 74 %, showed

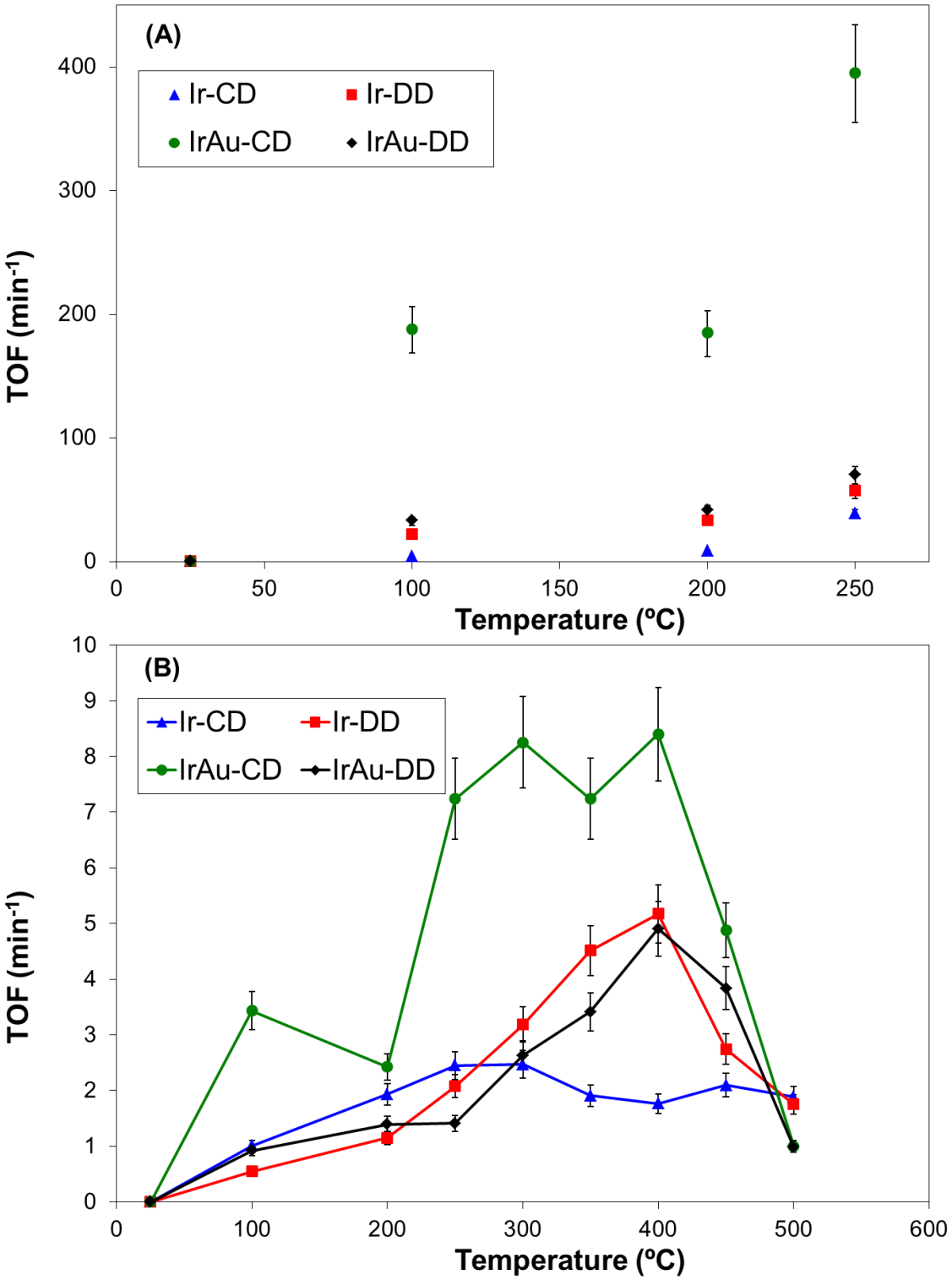

Figure 4.9. TOF of A) NO-CO reaction B) NO decomposition reaction over Ir monometallic and Ir-Au bimetallic catalysts.

Table 4.3. NO-CO reaction TOFs for all catalysts

Catalysts	Surface site amount (atoms/g cat) $\times 10^{-18}$	NO-CO TOFs (min^{-1}) at different temperature (℃)			
		25	100	200	250
Ir-CD	23.2±2.2	0	3.9	8.7	38.6
Ir-DD	20.5±2.7	0	22.1	33.2	57.2
Ir-Au-CD	3.1±0.3	0	187.5	184.6	395.0
Ir-Au-DD	13.5±1.1	0	33.0	41.5	69.9

Table 4. 4. NO reaction TOFs for all catalysts

Catalysts	Surface site amount (atoms/g cat) $\times 10^{-18}$	NO TOFs (min^{-1}) at different temperature (℃)								
		25	100	200	250	300	350	400	450	500
Ir-CD	23.2±2.2	0	1.0	1.9	2.4	2.5	1.9	1.8	2.1	1.9
Ir-DD	20.5±2.7	0	0.5	1.1	2.1	3.2	4.5	5.2	2.7	1.8
Ir-Au-CD	3.1±0.3	0	3.4	2.4	7.2	8.3	7.2	8.4	4.9	1.0
Ir-Au-DD	13.5±1.1	0	0.9	1.4	1.4	2.6	3.4	4.9	3.8	1.0

the lowest activity over the entire temperature range based on the calculated TOF values. The Ir-DD sample with iridium dispersion of 65 % exhibits slightly better activity, followed by Ir-Au-DD (D_{Ir} = 43 %). Finally, the maximum TOF of NO-CO reaction was attained over Ir-Au-CD with iridium dispersion of 10%. By comparing Ir-DD and Ir-Au-DD, there was no great difference in TOF, as can be seen in Figure 4.9A. This indicates that highly dispersed Au metal due to the dendrimer templating approach in this bimetallic sample does not affect to the activity of the catalyst, although there is electronic effect between Au and Ir observed in the sample based on the blue shift of IR peaks. In contrast, simply adding Au metal on Ir-Au-CD sample led to decrease Ir dispersion that is attributed to diluting surface Ir sites by Au and a concurrent change the intrinsic properties of the catalyst. Thus, with such a low dispersion, the TOF increased

dramatically due to the possible geometric effect of more weakly bound CO or NO on smaller Ir ensembles with presence of Au, as we observed red shift in FTIR spectrum. However, it should be noted that the increased activity per surface atom at low dispersion is offset by the decrease in the number of surface atoms. However, these results clearly indicate that NO reduction with CO over Ir-based catalysts seems to be a structure-sensitive reaction.

Similar results were obtained for direct NO decomposition as shown in Figure 4.9B. The Ir-Au-CD sample with the lowest iridium dispersion of 10 % showed the highest activity over the entire temperature range based on the calculated TOF values. Such an enhanced TOF was presumably attributed to altered surface structure by Au that changes the intrinsic catalytic activities for NO-CO and NO reactions by varying the surface structure. However, it eventually diminished the Ir surface active sites that are available for such reactions and led to poor catalytic performance with lower NO conversion compared with activity on Ir monometallic catalysts as shown in the Figures 4.5 and 7. On the other hand, both dendrimer-derived Ir monometallic and Ir-Au bimetallic catalysts exhibited similar TOF values over an entire reaction temperature region, suggesting that Au metal does not play a significant role in those materials in this reaction.

4.4 CONCLUSION

In this research, we prepared the Ir-Au bimetallic catalyst by using both dendrimer templating (Ir-Au-DD) and conventional incipient wetness (Ir-Au-CD)

methods. The dendrimer-derived sample showed highly dispersed particles with very narrow particle size distribution confirmed by STEM and H_2 chemisorption measurements, compared to the conventionally-derived sample. As a result, the Ir-Au-DD sample exhibited better catalytic performance in NO reduction by CO and NO decomposition reaction compared with Ir-Au-CD sample. NO-TPD results also illustrate sharper and larger N_2O formation peaks for the dendrimer-derived sample. In addition, the effect of Au in Ir-Au bimetallic catalysts was investigated by calculating TOFs. From these results, it was noticed that catalytic properties for the reduction of NO by CO and direct decomposition of NO over the Ir-Au bimetallic catalysts appear to be structure sensitive. For the case of dendrimer-derived Ir-Au catalyst, there was no great difference in TOF by comparison to an Ir monometallic catalyst, suggesting that highly dispersed Au metal does not affect to the activity of the catalyst. In contrast, higher TOF was obtained for the Ir-Au-CD sample than for Ir-CD, and this was most likely due to a geometric effect involving a dilution of Ir surface sites by Au.

CHAPTER 5

BIMETALLIC AG-IR/AL_2O_3 CATALYSTS PREPARED BY ELECTROLESS DEPOSITION: CHARACTERIZATION AND KINETIC EVALUATION

In this chapter, a series of alumina supported Ag-Ir bimetallic catalysts having controlled and incremental coverages of Ag, have been successfully prepared in an optimized electroless deposition bath. The starting monometallic Ir/γ-Al_2O_3 catalyst was highly dispersed (volume-surface mean diameter of 1.1 nm) with a narrow particle size distribution, as demonstrated by H_2 chemisorption and scanning transmission electron microscopy (STEM). While both catalytic (Ag on Ir) and autocatalytic (Ag on Ag) deposition were observed, coverages of Ag on Ir (measured by H_2 chemisorption) were successfully varied up to $\theta_{Ag} = 0.85$ by varying Ag weight loadings up to 0.81 wt%. In-situ transmission Fourier transform infrared spectroscopy (FTIR) of CO adsorption demonstrated that the Ag is indiscriminately deposited on all types of Ir surface sites during the ED process. Kinetic studies of CO oxidation revealed that higher coverages of Ag resulted in higher turnover frequencies. Comparison of reaction orders in CO and O_2 on monometallic Ir and the most active bimetallic catalyst ($\theta_{Ag} = 0.37$) suggests a bifunctional effect, where the Ag provides a non-competitive source of adsorbed oxygen for reaction with CO adsorbed on Ir.

5.1 INTRODUCTION

An increasing number of investigations have shown the advantage of employing bimetallic alloys in catalysis to provide enhanced selectivity, stability, and/or activity [114-117] for a variety of reactions. These bimetallic catalysts are typically prepared by either co-impregnation or successive impregnation of both metal salts onto the catalyst support [156]. However, these traditional methodologies often provide inadequate control over metal placement and accordingly yield catalysts containing both isolated, monometallic particles and bimetallic particles with varying compositions [1, 157]. This complex mixture results in poor control over the final catalyst performance, complicates catalyst characterization [158], and makes it very difficult to directly correlate the relationship between catalyst composition, characterization, and performance. Thus, new and reproducible methods are required for rational bimetallic catalyst design.

An alternate, industrially feasible method for the preparation bimetallic catalysts is electroless deposition (ED), where a controlled chemical reaction is used for selective deposition of reducible metal salts onto catalytic metal sites that have been activated by a reducing agent. Depending on the nature of the activated metal site, the process can involve deposition of the metal salt [A^+] from solution either onto the pre-existing metal [B^0] on the support (catalytic deposition) or onto the just reduced, deposited metal [A^0] (autocatalytic deposition) [159]. In principle, this ED method should result in the selective deposition of the secondary metal on the surface of a monometallic catalyst without formation of isolated crystallites of the secondary metal on the catalyst support. A more detailed description of this process has been published elsewhere [160].

The catalytic oxidation of carbon monoxide has been studied extensively due to its application for removing CO from waste gases of automotive combustion [161, 162], use in active filters of gas-masks [163], and for a variety of remote sensing applications [164-166]. The catalysts adopted consist mainly of oxides with variable oxidation state of the metal ions [167] and of supported noble metals on oxides [168, 169]. Especially, the oxidation of CO on platinum group metals has been studied extensively, and the reaction mechanism has also been thoroughly investigated over these catalysts [170-175]. A high activity for CO oxidation at higher reaction temperatures (150–250 °C) can be obtained on Pt catalysts; however, the competitive adsorption of CO and O_2 decreases their low temperature activity [176, 177]. On the other hand, more recently, oxide supported Au nanoparticles have attracted considerable attention for the reaction of CO oxidation[178, 179] due to their high catalytic activity at low temperatures [77]. Iridium, however, has not as often been considered as the catalyst for this reaction although it is situated among the same 5f orbital metals as Pt and Au. Therefore, this investigation explores the use of Ir-based bimetallic catalysts for the CO oxidation reaction. As the second metal, Ag was chosen due to the fact that silver metal has been extensively and successfully used for partial oxidation reactions, in which the silver–oxygen interaction is considered as a key step to explain the catalytic activity [180].

In this work, a series of Ag-Ir bimetallic catalysts has been synthesized to illustrate the effectiveness of the electroless deposition method to tune bimetallic surfaces for different catalytic purposes. The levels of Ag deposition have been intentionally limited to sub-monolayer coverages on the Ir surface, as verified by selective H_2 chemisorption and FTIR of CO adsorption on the Ir component of the Ag–Ir bimetallic

surface. Catalytic CO oxidation on the ED-derived Ag–Ir/Al_2O_3 bimetallic catalysts are compared to those obtained for Ir and Ag monometallic catalysts prepared using traditional incipient wetness methods. It was found that the difference in the structures of these series of bimetallic catalysts affected their catalytic performance, especially in terms of intrinsic activity of Ir metal. The targeted and efficient Ag placement on the Ir surface in the ED-derived Ag–Ir/Al_2O_3 bimetallic catalysts induces dramatic changes in intrinsic activity.

5.2 EXPERIMENTAL

The electroless deposition of Ag on Ir/Al_2O_3 was conducted using an aqueous bath of de-ionized (DI) water (made using Milli^{TM}-Q system), potassium silver cyanide, $KAg(CN)_2$ (54 wt.% Ag) supplied by Technic, Inc. as metal precursor, hydrazine (35 wt.% N_2H_4 solution, Sigma-Aldrich) as the reducing agent, and NaOH (EM pellets, 97% assay) to adjust pH. Metal salt/reducing agent molar ratios of 1:5 were used and the Ag deposition was conducted at room temperature (RT). Typically, the electroless bath volume was 100 ml for 0.5 grams of base Ir/Al_2O_3 catalyst (1.0 wt%; dispersion ~74% by H_2 chemisorption) prepared by the conventional incipient wetness (IW) method [181]. For this base Ir/Al_2O_3 catalyst, Ir metal ions were first impregnated onto a gamma-delta-theta phase alumina (specific surface area =104 m^2/g, pore volume = 0.9 mL/g, provided by Toyota). This material was then dried at 60 °C in a vacuum oven for overnight and then reduced at 400 °C in 100 cm^3/min (STP) of flowing H_2 for 1 h before storing at ambient conditions. The initial potassium silver cyanide concentration in the ED bath was varied depending on the targeted weight loadings of the Ag metal. All baths were

vigorously stirred to minimize any possible external mass transfer limitations and the solution pH was maintained at 11±0.5 by careful addition of concentrated NaOH solution. Small aliquots of ED solution (<2 ml) were collected and filtered using a 5μm mesh syringe filter at various time intervals of deposition to monitor the concentrations of Ag salts remaining in the bath during deposition. After the completion of ED (deposition times between 120 and 360 min), the slurry was filtered and washed repeatedly until all the remaining water soluble ligands (i.e., residual $Ag(CN)_2^-$ and CN^-) were removed. The wet sample cakes were dried under vacuum at room temperature and stored at ambient conditions. Thus, a series of the Ag–Ir/Al_2O_3 bimetallic catalysts with incremental Ag metal weight loadings and surface coverages on Ir was synthesized. A 1.0 wt% Ag/Al_2O_3 monometallic catalyst was also prepared by incipient wetness impregnation of $AgNO_3$ (≥ 99%, Sigma-Aldrich) for comparison, followed by drying and reduction at 250 °C for 1h under flowing H_2.

5.3 RESULT AND DISCUSSION

5.3.1 ED BATH DEVELOPMENT

Thermodynamically unstable, but kinetically stable electroless development baths are usually composed of a metal source, a reducing agent and solvent (typically water) [182, 183], and these conditions must be carefully controlled to avoid spontaneous metal reduction or precipitation in the deposition solution. Optionally, various chemical additives such as stabilizing agents, promoters, or inhibitors can be added to the ED bath for better stability, or to modify the deposition kinetics [184]. Unlike commercial uses such as electronic film or coating applications, which require a high rate of deposition

[185], preparation of bimetallic catalysts requires more precise control over the deposition kinetics to have fractional coverage of the second metal on the primary metal surface [160, 182, 186, 187].

Potassium silver cyanide, $KAg(CN)_2$, which is a CN^--coordinated Ag^+ salt, was chosen as the silver salt since it has a low standard reduction potential [$Ag(CN)_2^- + e^- \rightarrow +Ag + 2CN^-$, $E^0 = -0.31$ V] that provides high stability in the bath. This salt has also been well investigated for ED [187], where Rebelli et al. developed a series of electroless deposition baths using bis-cyano metal salts as sources for Cu, Ag, and Au deposition on silica-supported Pd surfaces. In this earlier work, according to the trend of catalytic activity for anodic oxidation, hydrazine was selected as the reducing agent for Ag deposition since hydrazine was preferably activated on Pd surfaces relative to the Ag metal that was being deposited [55]. Further, in order to reduce the stable $Cu(CN)_2^-$, $Ag(CN)_2^-$, and $Au(CN)_2^-$ species to their metallic states in a reasonable time period, a strong reducing agent such as N_2H_4 was needed. Thus, hydrazine as a reducing agent was also used for our study of Ag deposition on Ir/Al_2O_3 as well.

The formation of true bimetallic catalysts requires that ED occurs only on the catalytic Ir sites and not on the alumina support. To prevent unwanted electrostatic metal adsorption of bis-cyano metal anions onto Al_2O_3, the pH of the ED bath can play a key role. If the pH of the ED bath is kept above the point of zero charge (PZC) of the support, a negatively charged surface is maintained, which inhibits $Ag(CN)_2^-$-support interactions [1]. The PZC of the alumina support in this study was ~ pH 9; thus, the pH of the bath was maintained at 11±0.5.

5.3.2 Synthesis of Ag-Ir/Al_2O_3 Catalysts

The time-dependent metal deposition profiles are illustrated in Figure 5.1. The series of Ag–Ir/Al_2O_3 bimetallic catalysts were prepared with increasing coverages of Ag on the Ir surface, and approximately 0.5–1 gram of each Ag–Ir/Al_2O_3 bimetallic catalyst was prepared by varying bath volumes. Initial Ag concentrations were varied depending on the targeted, theoretical monolayers of the Ag metal to be deposited onto the Ir metal surface sites. It can be seen in Figure 5.1 that the rate of Ag deposition was very fast from 0 - 30 min, and then decreased. In addition, it was also found that samples using higher initial concentration take more time to complete the ED process. Thus, the sample with

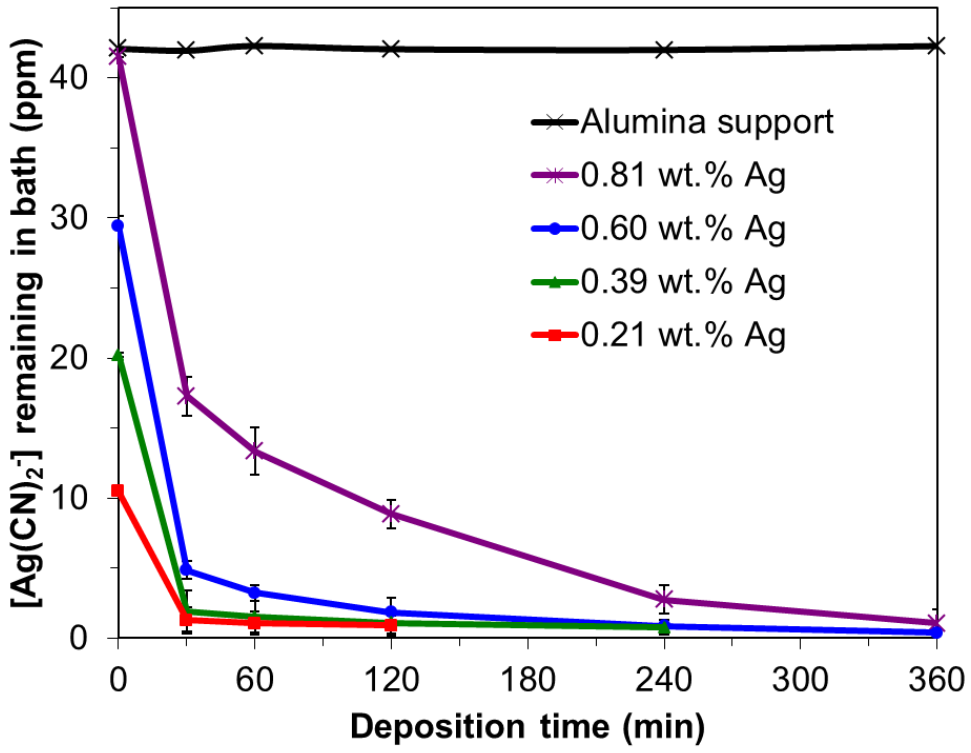

Figure 5.1. Time-dependent electroless deposition profiles for $Ag(CN)_2^-$ + N_2H_4 on 1.0 wt.% Ir/Al_2O_3. The legend denotes wt.% of Ag metal as determined by AA analysis of sample after deposition. The alumina support blank was the same as the support used for the 1.0 wt.% Ir/Al_2O_3 sample.

the highest initial Ag concentration required up to 360 min to complete the ED process, with deposited weight loadings up to 0.81 wt. % Ag being prepared. The most likely explanation for this is because hydrazine had been largely depleted at longer deposition times. Thus, it is limiting electroless deposition process.

On the other hand, the deposition of the Ag metal on Al_2O_3 support alone was negligible, indicating that there was no strong electrostatic adsorption (SEA) of $Ag(CN)_2^-$ on the oxide surface, as expected. This also confirms that alumina does not catalytically activate the reducing agent (N_2H_4) to facilitate electroless deposition (ED) under the given conditions. Therefore, Ir metal (or deposited Ag metal itself) is required for catalytic activation of the reducing agent.

5.3.3 Catalyst Surface Characterization

Hydrogen chemisorption was conducted on the series of Ag–Ir/Al_2O_3 catalysts to quantitatively determine the exposed Ir surface sites. Since Ag does not chemisorb H_2 at 40 °C [188, 189], Ag deposition on Ir should lead to a decrease in H_2 uptake. Thus, Ag coverage on Ir/Al_2O_3 or the fraction of the Ir surface covered by Ag for the bimetallic catalysts was determined in the following fashion. The number of surface Ir sites in the given bimetallic sample was subtracted from the number of surface Ir sites in the monometallic Ir/Al_2O_3 sample, and the resulting value was normalized to the latter. As a result, in Figure 5.2, the increase in Ag surface coverage for the bimetallic catalysts is evident with some scatter in the data. AA analysis of the ED baths and filtrates collected before, during, and after exposure of Ir/Al_2O_3 to pH 11 solutions detected no Ir or Al content. Further, the effect of hydrazine on sintering of Ir particles was non-existent and

this was confirmed by H_2 chemisorption. Recent work has shown that modest reducing agent-induced sintering of Pt or Pd particles can occur when contacted with specific reducing agents at ED conditions [81]. Hence, the lower hydrogen uptake with increase in Ag wt.% is due to electroless deposition of Ag metal on surface Ir sites or on previously-deposited Ag (see below).

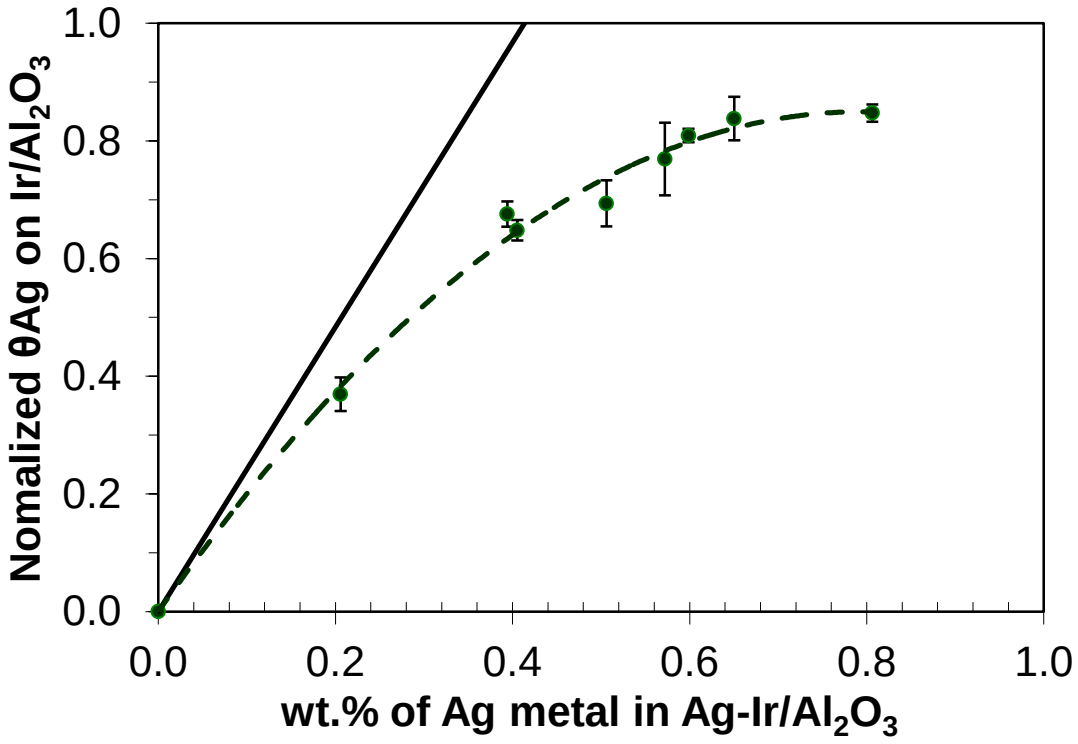

Figure 5.2. Normalized coverage of Ag on Ir for Ag-Ir/Al_2O_3 bimetallic catalysts derived from H_2 chemisorption data. The solid line is the theoretical plot assuming monodisperse coverage of the Ag metal on the Ir surface at a 1:1 deposition stoichiometry.

For a basis of comparison, the solid line in Figure 5.2 represents the theoretical values for monodisperse coverage of Ag metal on Ir at a 1:1 deposition stoichiometry. In this case, 0.41 wt.% of Ag is required for one theoretical monolayer. A complete summary of weight loadings of Ag metal deposited by ED is shown in Table 5.1. At higher Ag loadings there is a deviation of the experimental ED profile from the theoretical solid line,

indicating that autocatalytic deposition is also occurring. Specifically, autocatalytic (Ag^0-catalyzed) deposition predominates at higher weight loadings of deposition while catalytic (Ir^0-catalyzed) deposition prevails at lower ones. This is largely because ED is kinetically- controlled; thus, the concentration of available surface Ir sites decreases as the surface concentration of the second metal increases to give more autocatalytic deposition. Similar results have been reported for group 1B electroless deposition over Pd [187]. Although both catalytic and autocatalytic deposition processes occur, the great majority of the Ir surface (up to 85%) was covered by Ag metal. This suggests that hydrazine was indeed preferentially oxidized (i.e., activated) on Ir relative to Ag to favor catalytic deposition of Ag on Ir.

Table 5.1. Electrolessly deposited weight loadings and surface coverages of Ag metal on Ir/Al_2O_3. θ_{mono} refers to theoretical monodisperse layers of Ag metal on Ir and $\theta_{expt'l}$ denotes Ag coverage determined from chemisorption analysis.

Ag-Ir/Al_2O_3, from $Ag(CN)_2^-$		
wt.% Ag[a]	θ_{mono}, ML[a]	$\theta_{expt'l}$, ML[b]
0.81	1.95	0.85
0.60	1.45	0.81
0.39	0.96	0.68
0.21	0.49	0.37

[a]Obtained by elemental analysis.

[b]Based on metallic dispersion obtained from H_2 chemisorption data (H per Ir metal).

Spectra collected following the adsorption of CO at room temperature on monometallic Ir/Al_2O_3 and Ag/Al_2O_3, as well as the Ag-Ir/Al_2O_3 bimetallic samples, are

shown in Figure 5.3. A common absorbance scale was used to better illustrate the differences between the spectra. For both Ir/Al_2O_3 and $Ag\text{-}Ir/Al_2O_3$ catalysts, CO stretching bands were observed in 1950–2150 cm^{-1} region, whereas no characteristic ν_{CO} vibrations were observed in the spectra of the Ag/Al_2O_3 catalyst, in agreement with observations of Rodriguez et al. [190]. For the Ir/Al_2O_3 sample, the region between 1950 and 2150 cm^{-1} contains several overlapping features, which can be deconvoluted into five peaks centered at 2012, 2035, 2053, 2078 and 2092 cm^{-1}. These peaks are attributed to linearly adsorbed CO species on fully reduced Ir sites (2035, 2053cm^{-1}) or on partially oxidized Ir sites (2092cm^{-1}) or antisymmetric (2012cm^{-1}) or symmetric (2078 cm^{-1}) vibrations of adsorbed dicarbonyl species on Ir ions, respectively. The assignment of these peaks in this spectral region is based on our previous published work [191] and the available literature [95-97, 145].

In the case of bimetallic surfaces, the intensity of FTIR spectra decrease with increasing Ag content, indicating lower CO uptake due to electroless deposition of Ag on Ir. However, the relative intensity ratios of linear CO adsorption on Ir sites or vibrations of adsorbed dicarbonyl species were not significantly changed with Ag deposition, suggesting that Ag is indiscriminately deposited on all Ir surface sites. In such a situation, the intensities of all bands would be expected to decrease, but the shape of the spectra would remain roughly constant. Thus, the results suggest that Ag electroless deposition on Ir is not particularly favored on any of the various Ir surface planes or other sites that are exposed, which is in agreement with the recent literature [160, 187].

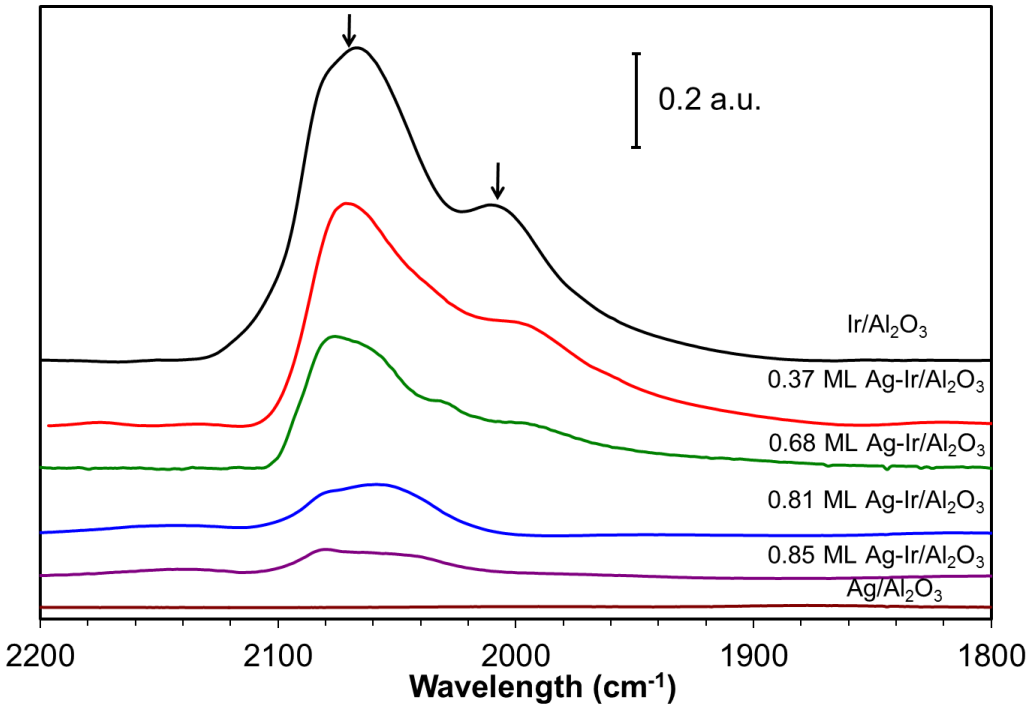

Figure 5.3. Transmission FTIR spectra of CO adsorption on Ir/Al_2O_3, Ag/Al_2O_3 and Ag-Ir/Al_2O_3 bimetallic catalysts. Arrows highlight peak intensity losses (↓) as Ag wt.% increases.

5.3.4 Catalytic Oxidation of CO

In order to evaluate the catalytic activity for the family of alumina supported Ag-Ir bimetallic catalysts, CO oxidation was chosen as a probe reaction. As expected, before the evaluation of catalysts, the activity of the Al_2O_3 support was found to be virtually inactive for CO oxidation at the reaction conditions used in this study.

The light-off curves showing the temperature dependence of CO oxidation over the Ag-Ir bimetallic samples along with Ir and Ag monometallic catalysts are shown in Figure 5.4. The Ag/Al_2O_3 shows low levels of activity for CO oxidation based on the lower CO conversion over the entire reaction temperature region compared with other Ir/Al_2O_3 and Ag-Ir bimetallic catalysts. On the other hand, the Ir/Al_2O_3 catalyst shows a

T_{50} (i.e., temperature at 50% CO conversion) of ~218 °C, while the lower Ag coverage bimetallic catalysts exhibit enhanced performance for CO oxidation reaction based on the lower T_{50} values. Specifically, the lowest T_{50} of ~195 °C is observed for the Ag-Ir/Al_2O_3 catalyst with $\theta_{Ag} = 0.37$. Further, catalytic CO oxidation activity declines for $\theta_{Ag} = 0.81$ and 0.85 due to Ag coverage of active, surface Ir sites. This is similar to a trend observed in previous work by our group [183] for the hydrogenation of 3,4-epoxy-1-butene over Ag-Pt bimetallic catalysts. A maximum in activity was observed at low Ag coverages for Ag-Pt/SiO_2, with the activity decreasing at higher Ag loadings. As in the case for the Ag-Pt catalysts, the apparent synergistic effect of Ag on Ir is interesting since Ag addition to Group VIII catalysts typically lowers activity for catalytic reactions [192, 193]. However, it sometimes improves catalyst stability and modifies product selectivity [194].

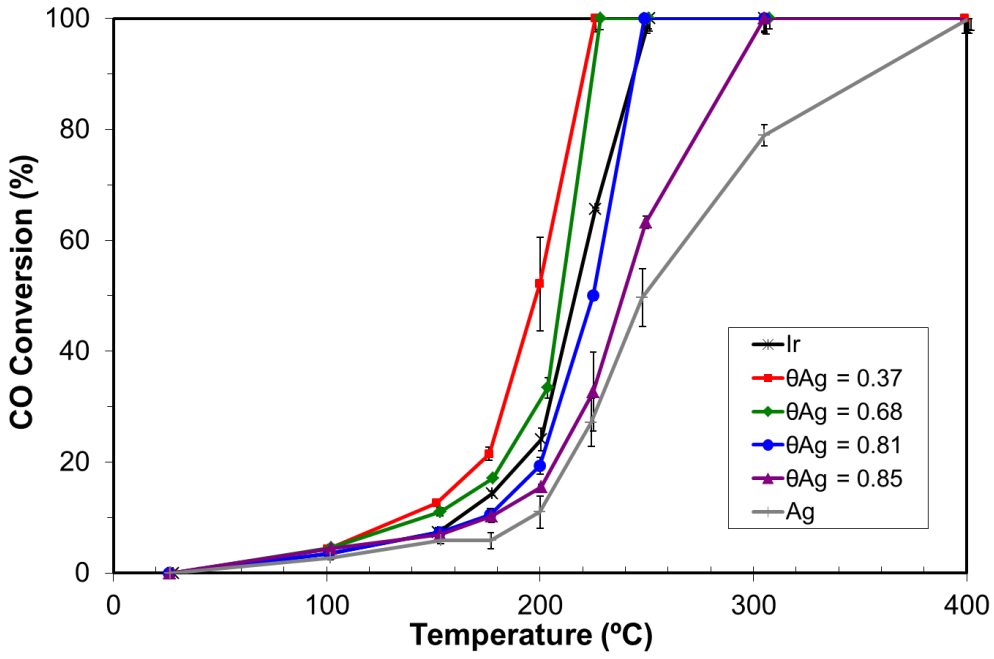

Figure 5.4. Light-off curves of catalytic CO oxidation over Ir/Al_2O_3, Ag/Al_2O_3 and Ag-Ir/Al_2O_3 bimetallic catalysts.

To study the role of Ag in the ED-derived Ag-Ir/Al_2O_3 catalysts regarding activity and for better comparison between the catalysts, the intrinsic activities expressed in terms of turnover frequencies (TOFs) were calculated at a reaction temperature of 175 ºC, as shown in Figure 5.5. This temperature was chosen for comparison since all of the CO conversions were pseudo-differential at ≤ 20%. It was also confirmed that there is no mass and heat transfer limitations in this kinetic regime by using the Weisz-Prater and the Mears criteria [195, 196] (see Appendix A for details). Detailed procedures were adopted from the literature [197, 198]. In the case of Ir-containing samples, the TOF values were calculated using the number of exposed Ir surface sites based on the H_2 chemisorption as we described in Section 5.3.3, whereas for the Ag monometallic catalyst the number of Ag sites determined by O_2 chemisorption using the method described by Vannice [199] was used. As references, Ir/Al_2O_3 and Ag/Al_2O_3 monometallic samples show TOF values of 1.8 and 0.8 s^{-1}, respectively. In the case of Ag-Ir/Al_2O_3 bimetallic samples, higher Ag coverages show higher intrinsic activities based on the higher TOF values. Thus, the bimetallic catalyst with the highest Ag coverage has a TOF value that is about a factor of five higher than for monometallic Ir, as shown in Figure 5.5 (a). This improvement in the catalytic activities for CO oxidation indicates that selectively deposited Ag metal on Ir plays a key role in changing the catalysis on Ir by varying the surface structure and morphology of the catalyst.

However, Figure 5.5 (a) likely overstimates the bimetallic effect, since it neglects the intrinsic activity of Ag in the samples.. In calculating the TOF values, only the number of exposed Ir surface sites was used, but not for the Ag sites or Ir-Ag sites that can be also active toward this reaction. It is difficult to measure the exact value of exposed Ag sites

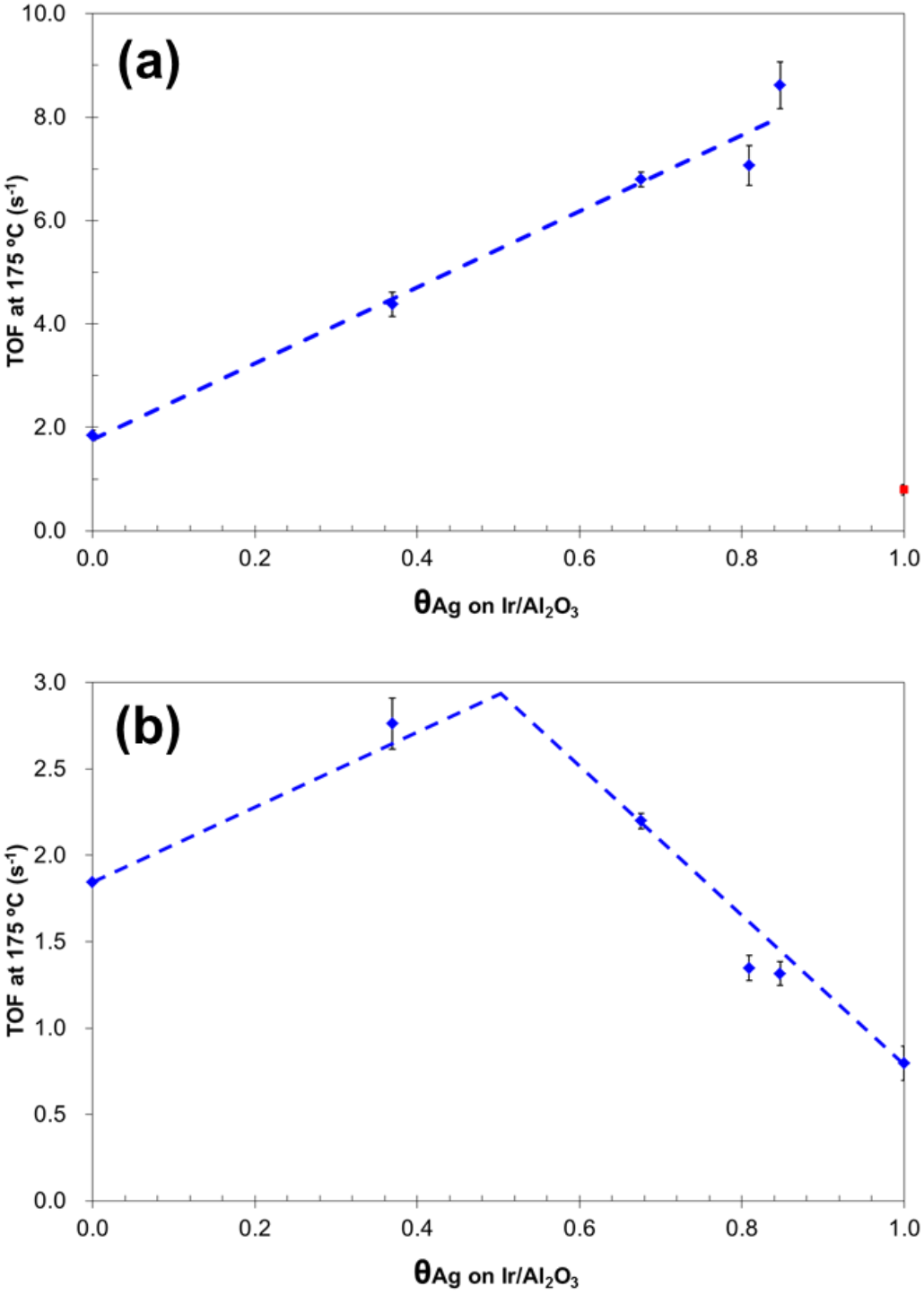

Figure 5.5. TOF of CO oxidation at 175 °C over Ir/Al_2O_3, Ag/Al_2O_3 and $Ag\text{-}Ir/Al_2O_3$ bimetallic catalysts. See text for details.

with direct chemisorption methods. However, the ED results show that Ag covers the Ir metal sites. Thus, it can be assumed that the total number of exposed metal (Ir + Ag) remains roughly constant and equal to the number of original surface Ir sites in the monometallic Ir/Al_2O_3 sample. In this case, the plot shown in Figure 5.5 (b) is obtained, which shows a typical volvano type behavior with a maximum at an Ag coverage of around 0.5. Given the relatively even deposition of Ag atoms on Ir based on the FTIR spectroscopic results for CO adsorption, this point is where there would be the most Ir-Ag site pairs on the surface.

The higher activity for the Ag-Ir bimetallic catalysts can result from: a) contribution of Ag metal sites to form bifunctional Ag-Ir sites that are catalytically more active by preferential adsorption of oxygen on Ag that reacts with CO adsorbed on Ir to form CO_2, b) bimetallic Ag-Ir surface that have higher intrinsic activity caused by geometric or electronic effects imposed on Ir by Ag, or c) a combination of the two hypotheses.

To determine whether the bifunctional active site hypothesis was operative, detailed kinetics were investigated. Two separate sets of $CO\text{-}O_2$ reaction experiments were done at 175 °C for both the monometallic Ir and the Ag-Ir bimetallic sample that gave the lowest T_{50} ($\theta_{Ag} = 0.37$) and is near the maximum of the plot in Figure 5.5 (b). In the first experiment, a high constant P_{CO} and variable P_{O2} from high to low values were used, while in the second experiment, a high constant P_{O2} and variable P_{CO} from high to low values were employed. Since the reaction rate of CO_2 formation can be expressed as the power rate law in Eq. (5.1), taking the logarithm of both sides permits determination of the reaction orders in O_2 for the first set of data [Eq (5.2)], where the O_2 reaction order

is the value of the slope y and the reaction order for CO [Eq. (5.3)] is the value of slope x.

$$r_{CO_2} = kP_{CO}{}^{x}\, P_{O_2}{}^{y} \tag{5.1}$$

$$lnr_{CO_2} = \ln(k * P_{CO}{}^{x}) + y \ln P_{O_2} \tag{5.2}$$

$$lnr_{CO_2} = ln(k * P_{O_2}{}^{y}) + x \ln P_{CO} \tag{5.3}$$

Figure 5.6 (a) and (b) show the lnr_{CO2} versus lnP_{CO} or lnP_{O2} plots for monometallic Ir and bimetallic Ag-Ir catalysts. From the slope values in Figure 5.6(a), the CO reaction order was -1 over Ir and approximately zero order over Ag-Ir. For O_2 (Fig 5.6b) the reaction orders were half order for Ir and lower fractional order for Ag-Ir.

Based on the Langmuir-Hinshelwood (L-H) formalism, the kinetic parameters for CO_2 formation over monometallic Ir can be expressed by equations 5.4-6 for competitive adsorption of CO and O_2 on Ir sites.

$$r_{CO_2} = k_1 \theta_{CO(Ir)} \theta_{O(Ir)} \tag{5.4}$$

$$\theta_{CO(Ir)} = \frac{K_{CO}P_{CO}}{1 + K_{CO}P_{CO} + (K_{O_2}P_{O_2})^{0.5}} \qquad where\ K = \frac{k_{ads}}{k_{des}} \tag{5.5}$$

$$\theta_{O(Ir)} = \frac{(K_{O_2}P_{O_2})^{0.5}}{1 + K_{CO}P_{CO} + (K_{O_2}P_{O_2})^{0.5}} \tag{5.6}$$

For strongly adsorbed CO on Ir, the $K_{CO}P_{CO}$ term is much larger than the sum of the other terms of the denominator in equation (5.5). In fact, reports show that K_{CO} is proportional to the heat of adsorption of CO which is much larger than for atomic O adsorbed on Ir metal [200, 201]. Thus, the coverage of CO and atomic O can be rewritten as follows.

$$\theta_{CO(Ir)} \cong \frac{K_{CO}P_{CO}}{K_{CO}P_{CO}} = 1 \tag{5.7}$$

$$\theta_{O(Ir)} \cong \frac{(K_{O_2}P_{O_2})^{0.5}}{K_{CO}P_{CO}} \quad (5.8)$$

After substitution of equations (5.7) and (5.8) into equation (5.4), the reaction rate is 0.5 in O_2 and -1.0 order in CO as shown in equation (5.9).

$$\therefore r_{CO_2} = k_1 \frac{(K_{O_2}P_{O_2})^{0.5}}{K_{CO}P_{CO}} = k' {P_{O_2}}^{0.5} {P_{CO}}^{-1} \quad (5.9)$$

Thus, the results shown in Figure 5.6 are consistent with competitive adsorption of CO and O_2 on Ir. For the case of the Ag-Ir bimetallic catalysts, the coverage of CO and atomic O on the both metals must be considered since Ag is active for dissociative adsorption at T > 150 °C [199, 202]; thus, the overall reaction rate of CO_2 formation may involve several surface reactions which can be written as follows:

$$r_{CO_2} = k_1[\theta_{CO(Ir)}\theta_{O(Ir)}] + k_2[\theta_{CO(Ir)}\theta_{O(Ag)}] + k_3[\theta_{CO(Ag)}\theta_{O(Ir)}] + k_4[\theta_{CO(Ag)}\theta_{O(Ag)}] \quad (5.10)$$

Since the coverage of CO on Ag is negligible due to weak adsorption (Figure 5.3), adsorption on Ag can be simplified to:

$$\theta_{O(Ag)} = \frac{(K'_{O_2}P_{O_2})^{0.5}}{1 + K'_{CO}P_{CO} + (K'_{O_2}P_{O_2})^{0.5}} \cong \frac{(K'_{O_2}P_{O_2})^{0.5}}{1 + (K'_{O_2}P_{O_2})^{0.5}} \quad (5.11)$$

Then, by substituting equations (5.7), (5.8) and (5.11) into Equation (5.10), equation (5.12) is obtained.

$$r_{CO_2} = k_1\left[\frac{(K_{O_2}P_{O_2})^{0.5}}{K_{CO}P_{CO}}\right] + k_2\left[\frac{(K'_{O_2}P_{O_2})^{0.5}}{1 + (K'_{O_2}P_{O_2})^{0.5}}\right] \quad (5.12)$$

If there is no participation of O adsorbed on Ag for CO_2 formation, then the second term

in eqn. (5.12) is negligible, and the reaction rate would be the same as for monometallic Ir (i.e., Equation 5.9). For high P_{CO}, the first term in eqn. (5.12) can be neglected and then

$$r_{CO_2} \cong k_2 \left[\frac{(K'_{O_2} P_{O_2})^{0.5}}{1 + (K'_{O_2} P_{O_2})^{0.5}} \right] = k' P_{CO}{}^{0} P_{O_2}{}^{y} \quad where \ 0 \leq y \leq 0.5 \qquad (5.13)$$

This analysis implies that if the reaction rate is governed by a bimetallic Ir-Ag interaction, the reaction rate should be zero order in CO and y order in O_2, where y is larger than 0 and smaller than 0.5 as shown in Equation (5.13). This is consistent with the kinetic results shown in Figure 5.6. Such a non-competitive adsorption of CO and O leads to increased formation rates of CO_2 over the bimetallic catalyst. This is largely because (a), on group VIII metals, CO usually has high heats of adsorption, which are approximately equal to the activation energy for CO desorption [203] and (b), the surface reaction between adsorbed CO and O is also very efficient for all platinum group metals [203]. Therefore, the kinetic result is likely to be associated with the adsorption of oxygen. If the metal particles formed in the Ag-Ir catalyst are bimetallic in nature (as is the case here) and these proximal Ag surface sites provide sites upon which O_2 can dissociatively adsorb, this will result in higher rates of CO_2 formation. According to the kinetic results, it is concluded that a bifunctional effect is operative. Consideration of an Eley-Rideal (E-R) mechanism (see E-R mechanism prediction in Appendix B) led to predicted reaction orders inconsistent with those observed here.

The presence of small electronic or geometric effects of Ag on Ir cannot be entirely excluded. However, an electronic effect appears unlikely since no binding energy

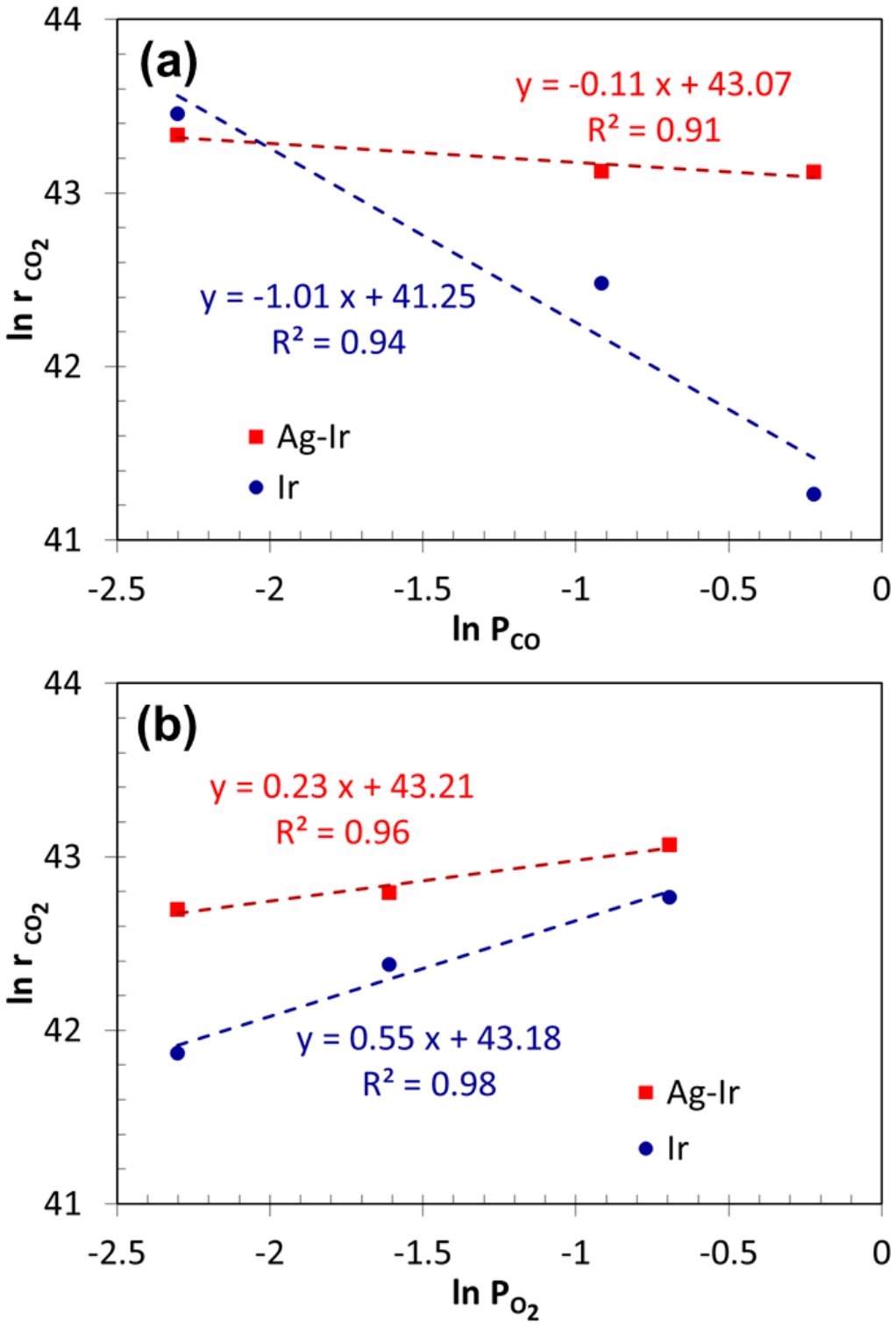

Figure 5.6. CO oxidation reaction order plots at 175 °C for Ir/Al_2O_3 and $Ag\text{-}Ir/Al_2O_3$ bimetallic (θ_{Ag} = 0.37) catalysts in a) CO and b) O_2. See text for details.

shift is observed for the Ir4f or Ag3d XPS peaks regardless of the Ag coverage on Ir (see Figure 5.7 for details). All the deconvolution of signals was assigned based on the literature [204-207]. A possible geometric effect is also not easy to rule out. This is largely because previous results for Ag-Pd [186, 187] and Ag-Pt [183] in our group have shown that small ensembles of Pd and Pt strongly favor the formation of more weakly-bound linear CO than the more strongly bound two-fold and three-fold adsorbed species. However, based on the lack of any evidence, such as a shift in FTIR peak positions, an ensemble effect in this work is unlikely. Clearly the Ag atoms need to be geometrically arranged on the Ir to cause the bifunctional effect. However, it this change in Ir ensemble size with increasing Ag coverage does not appear to significantly change the bond strength between CO and the Ir surface sites.

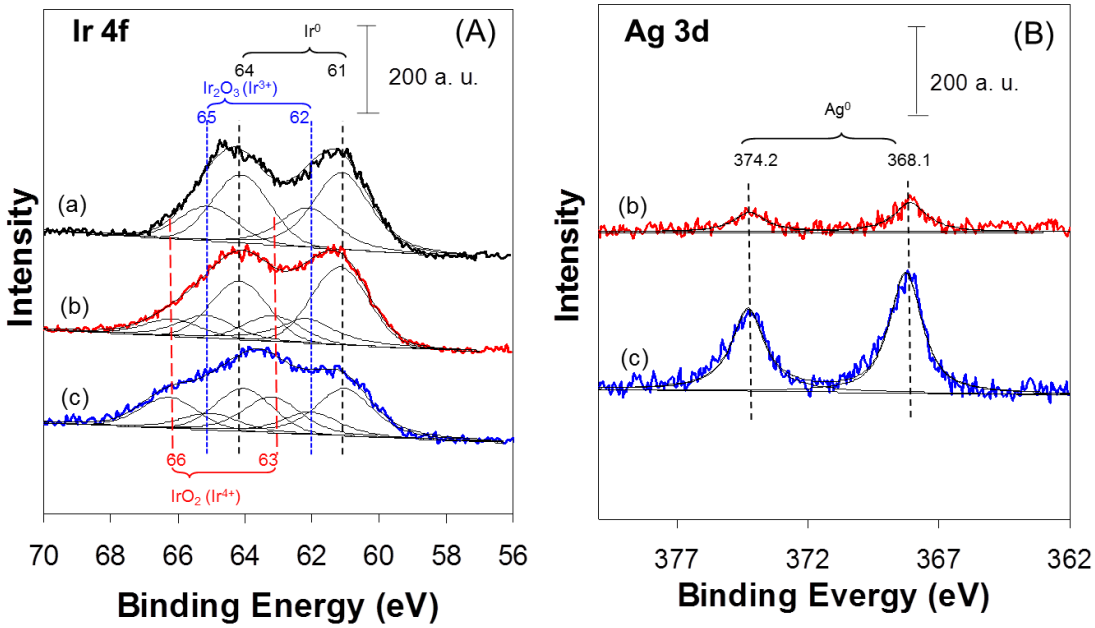

Figure 5.7. XPS data for oxidation state of A) Ir 4f and B) Ag 3d on a) Ir/Al_2O_3 and Ag-Ir/Al_2O_3 bimetallic catalysts with b) $\theta_{Ag} = 0.37$ and c) $\theta_{Ag} = 0.85$. See text for details.

5.4 CONCLUSION

A series of alumina-supported Ag-Ir bimetallic catalysts having controlled and incremental coverages of Ag, has been successfully prepared in an optimized electroless deposition bath. All characterization methods confirmed that the deposition of Ag metal occurred only on the Ir surface, and not the alumina support, to give true bimetallic catalysts. The extent of decrease in Ir surface sites with increased addition of second metal indicated that catalytic deposition predominates at lower level of Ag coverage, whereas autocatalytic electroless deposition (Ag^{+} deposition onto Ag^{0}) also occurs at higher Ag coverages. Furthermore, infrared studies showed that the deposited Ag is non-preferentially located on all Ir surface sites.

Bimetallic Ag-Ir catalysts prepared by electroless deposition method resulted in better catalytic activity for CO oxidation reaction compared with Ir monometallic catalyst. CO conversion over Ir/Al_2O_3 was greatly enhanced by the addition of small amounts of Ag, which is not very active for CO oxidation itself. Such an increased activity is clearly linked to the modification of the Ir surface by the addition of Ag. Higher intrinsic activities of Ir were obtained with increasing Ag coverage in the bimetallic catalysts, and the highest TOF was obtained at the half point where the Ir-Ag pair sites are maximized. Thus, this modification appears to involve almost purely a bifunctional effect of noncompetitive adsorption of O_2 on Ag sites contiguous to Ir sites where CO is strongly adsorbed.

CHAPTER 6

PREPARATION, CHARACTERIZATION AND EVALUATION OF ELECTROLESS DEPOSITED BIMETALLIC AU-IR/AL$_2$O$_3$ CATALYSTS

In this chapter, a series of Au–Ir/Al_2O_3 catalysts with controlled and incremental coverages of Au have been prepared by the electroless deposition. The structural and electronic properties of the catalysts were characterized using hydrogen chemisorption, atomic absorption spectroscopy, Fourier transform infrared spectroscopy, and X-ray photoelectron spectroscopy. The results suggest that Au was deposited on all types of Ir surface sites in a non-discriminatory fashion. Kinetic studies of CO oxidation revealed that higher coverages of Au resulted in lower turnover frequencies, indicating no bimetallic effect between Au and Ir for this reaction. In contrast, enhanced catalytic activities were found toward NO-CO reaction over ED-derived bimetallic Au-Ir as well as Ag-Ir catalysts. This can be explained by a probable bifunctional effect, but more kinetic studies need to be done to fully understand the mechanism for this.

6.1 INTRODUCTION

Nanocrystalline gold supported on oxides has been widely studied since the discovery in the late 1980s that gold can be catalytically active when it is dispersed as small particles (<5 nm) on an oxide support [142, 208, 209]. These most remarkable catalytic properties of supported gold were first obtained for the oxidation of CO at room

temperature by Haruta et al [210]. Gold can also be active in various other reactions, such as water gas shift [211], CO and CO_2 hydrogenation [212], selective hydrogenation [213, 214], reduction of NO with hydrocarbons [215], epoxidation of propylene[216], and oxidation of volatile organic compounds [217].

These gold catalysts, however, are not stable because their catalytic activity decreases gradually during the catalytic run [218, 219] due to either the sintering of gold particles [219, 220] or the adsorption of carbonates on catalytic active sites [221, 222]. This insufficient stability has hindered their wide use in commercial applications. Many investigations have been made to stabilize these gold catalysts by adding a second metal. The addition of a second metal could change the electronic properties of gold particles [223], or it could change their local atom distribution by rearranging surface structures between gold and the added metal [224]. Iridium is one of the metals that has been added to gold catalysts [76]. Density functional theory calculations of Liu et al. [85] in the Au/IrO_2-TiO_2 system show that the introduction of the iridium oxide allows the presence of an active Au/IrO_2 interface that could increase the resistance Au sites to sintering.

Recently, the catalytic activity and stability of a series of Ir and Au-Ir catalysts supported on titania during the CO oxidation was explored [76]. In that work, high catalytic activity of supported gold catalysts depended strongly on the preparation method. Thus, it was observed that the most active Au-Ir catalysts were those prepared by sequential deposition: first depositing iridium and then gold. These Au-Ir catalysts had a higher catalytic activity for the oxidation of CO than those containing only gold and were more stable.

Besides CO oxidation, supported Au-Ir catalysts have been used to catalyze other chemical reactions. For instance, Chimentao et al. have found that the addition of Au improved the chemisorptive and catalytic properties of bimetallic Ir-Au/γ-Al_2O_3 catalysts compared to the pure Ir sample for methylcyclopentane hydrogenolysis [83]. In these catalysts, some influence of the preparation method on the catalyst stability was also observed. Okumura et al. [225] reported that Au in combination with Ir shows high catalytic activity for the decomposition of dioxins at temperatures below 200 ℃. Akita et al. [86] deposited gold and iridium simultaneously on a rutile TiO_2 single crystal in an attempt to clarify any synergetic effects on the catalytic performance for the oxidative decomposition of dioxins.

In the present work, a series of Au-Ir supported on Al_2O_3 catalysts were prepared by electroless deposition (ED) to study the catalytic performance of these materials in the CO oxidation reaction. It is shown for the first time that ED method is able to deposit targeted Au wt.% on Ir metal selectively for rational bimetallic catalyst design. In addition, the activity and stability of the Au-Ir/Al_2O_3 catalyst is improved with respect to the Au/Al_2O_3 catalyst. Although, tt should be noticed that this Au monometallic catalyst was prepared by conventional IW method, thus the size of Au particles are not optimized. The effect of Au on Ir dispersion and H_2 adsorption properties of the catalyst was determined, which leads to relevant structure-function relationships for the investigated reaction.

6.2 EXPERIMENTAL

A similar procedure was used to prepare electrolessly deposited Au-Ir bimetallic samples as was used for Ag-Ir bimetallic samples (see Section 5.2 for details). Briefly, the electroless deposition of Au on Ir/Al_2O_3 was conducted using an aqueous ED bath containing potassium dicyanoaurate ($KAu(CN)_2$, (68 wt.% Au), Sigma-Aldrich), as metal precursor, hydrazine (35 wt.% N_2H_4 solution, Sigma-Aldrich) as the reducing agent, and NaOH (EM pellets, 97% assay) to adjust pH. Metal salt/reducing agent molar ratios of 1:20 were used and the Au deposition was conducted at room temperature (RT). The initial potassium dicyanoaurate concentration in the ED bath was varied depending on the targeted weight loadings of the Au metal. . The synthesis of the 1 wt% Ir/Al_2O_3 catalyst was described in Chapter 5. All baths were vigorously stirred to minimize any possible external mass transfer limitations and the solution pH was maintained at 9±0.5 by careful addition of concentrated NaOH solution. To accelerate the rate of gold deposition, small aliquots of concentrated hydrazine solution were added every 30 min during the complete ED process. The final slurry was filtered and washed repeatedly until all the remaining water soluble ligands (i.e., residual $Au(CN)_2^-$ and CN^-) were removed. The wet sample cakes were dried under vacuum at room temperature and stored at ambient conditions. Thus, a series of the $Au–Ir/Al_2O_3$ bimetallic catalysts with incremental Au metal weight loadings and surface coverages on Ir was synthesized. A 1.0 wt% Au/Al_2O_3 monometallic catalyst was also prepared by incipient wetness impregnation of $HAuCl_4$ for comparison, followed by drying and reduction at 200 °C for 1h under flowing H_2.

6.3 RESULT AND DISCUSSION

6.3.1 ED BATH DEVELOPMENT

A wide variety of gold electro-deposition and electroless-deposition baths are commercially available due to their extensive use in electronic or semiconductor coating applications [52, 57, 226]. For these baths, high rates of deposition are required to give continuous film. However, in the case of bimetallic catalyst synthesis, kinetically controlled deposition is essential to have fractional coverages of the second metal (i.e., Au) onto the primary metal (i.e., Ir) surface. The appropriate ED bath can be developed by tuning various ED bath parameters such as concentrations of metal ion source, reducing agent, pH and temperature. The present ED bath was configured using potassium dicyanoaurate, $KAu(CN)_2$, which is a CN^--coordinated Au^+ salt, as the gold source, since it has a low standard reduction potential [$Au(CN)_2^- + e^- \rightarrow Au + 2CN^-$, E^0 = -0.596 V] that provides high stability in the bath. This salt has also been well investigated for ED by Rebelli et al. [187], who developed a series of electroless deposition baths using bis-cyano metal salts as sources for Cu, Ag, and Au deposition on silica-supported Pd surfaces. In this earlier work, according to the trend of catalytic activity for anodic oxidation, hydrazine was selected as the reducing agent for Au deposition since hydrazine was preferably activated on Pd surfaces relative to the Au metal that was being deposited [55]. In addition, in order to reduce the stable $Cu(CN)_2^-$, $Ag(CN)_2^-$, and $Au(CN)_2^-$ species to their metallic states in a reasonable time period, a strong reducing agent such as N_2H_4 was needed. Thus, hydrazine as a reducing agent was also used in the present case for Au deposition on Ir/Al_2O_3. Furthermore, the successful ED of Ag on Ir/Al_2O_3 was demonstrated in Chapter 5 using hydrazine as a reducing agent. However, hydrazine was

found to be largely depleted at longer deposition times, limiting the Ag electroless deposition process (see Chapter 5 for details). This is largely because hydrazine consumes two electrons to form ammonia, while at the same time serving as a four electron donor in alkaline baths [227]. Therefore, an additional small aliquot of concentrated N_2H_4 solution ($\leq$ 1ml) was added every 30min during the ED process to accelerate the rate of Au deposition (see Figure 6.1 for detail).

For optimum ED kinetics, the choice of solution pH of the bath is also very important. At basic pH values, the activity of reducing agent is typically higher and the rate of deposition increases. In addition, the pH of the solution can determine the charge-based interaction between metal ions and support. If the pH of the ED bath is kept below the point of zero charge (PZC) of the alumina support (between 7 and 9), a positively charged surface is maintained, which leads to $Au(CN)_2^-$ and support interactions. Thus, to prevent unwanted electrostatic metal adsorption, the solution pH should be maintained above the PZC of the support. However, it should be noted that if the pH is too high, the bath becomes unstable even at short times, resulting in spontaneous metal reduction and precipitation.

6.3.2 Synthesis of Au-Ir/Al_2O_3 Catalysts

The series of Au–Ir/Al_2O_3 bimetallic catalysts was prepared with increasing coverages of Au on the Ir surface. The bath concentrations were chosen at kinetically stable conditions, but were thermodynamically unstable, such that complete deposition occurreds within 2 hr. The various Au-Ir/ Al_2O_3 bimetallic catalysts were synthesized at room temperature and pH 9 with the $Au(CN)_2^-$: N_2H_4 molar ratio chosen to be ~ 1:20.

Initial Au concentrations were varied depending on the targeted, theoretical monolayers of the Au metal to be deposited onto the Ir metal surface sites. The time-dependent metal deposition profiles are shown in Figure 6.1.

As explained above, the formation of true bimetallic catalysts requires that ED occurs only on the catalytic Ir sites and not on the alumina support. The deposition curves in Figure 6.1 indicate that alumina alone does not result in deposition of Au, but that Ir is required for catalytic deposition.

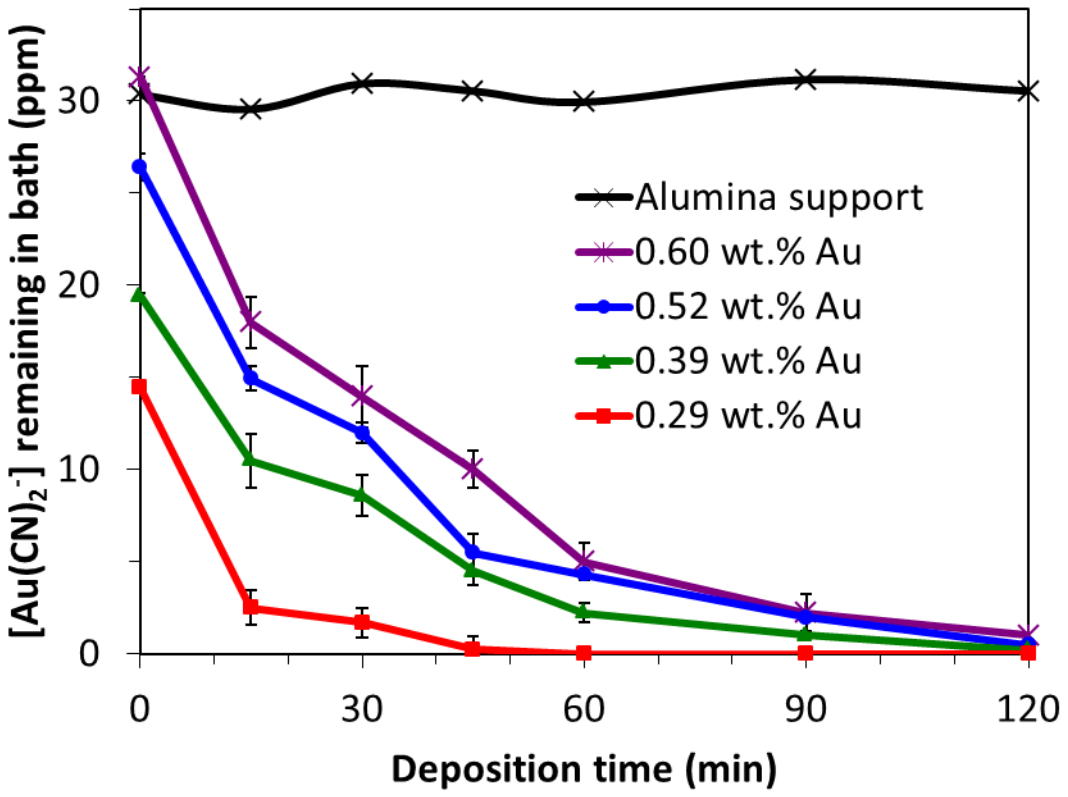

Figure 6.1. Time-dependent electroless deposition profiles for $Au(CN)_2^-$ + N_2H_4 on 1.0 wt.% Ir/Al_2O_3. The legend denotes wt.% of Au metal as determined by AA analysis of sample after deposition. The alumina support blank was the same as the support used for the 1.0 wt.% Ir/Al_2O_3 sample.

6.3.3 CATALYST SURFACE CHARACTERIZATION

Bimetallic samples were characterized by hydrogen chemisorption to determine the effectiveness of the ED process for deposition of Au on Ir. As Au weight % increases in Au–Ir/Al_2O_3 bimetallic samples, H_2 uptake would decrease because Au does not chemisorb H_2 at 40 °C [83, 228]. Thus, Au coverage on Ir/Al_2O_3 (i.e., the fraction of the Ir surface covered by Au) for the bimetallic catalysts can be determined in the following fashion. The number of surface Ir sites in the given bimetallic sample was subtracted from the number of surface Ir sites in the monometallic Ir/Al_2O_3 sample, and the resulting value was normalized to the latter. Figure 6.2 shows normalized Au coverages on Ir determined by chemisorption plotted as a function of Au weight loading as measured using AA spectroscopy. For a basis of comparison, the solid line represents the theoretical Au coverages that would arise, assuming only catalytic deposition of Au on Ir in a 1:1 Au:Ir surface atom ratio. A summary of weight loadings of Ag metal deposited by ED is shown in Table 6.1. Experimental Au coverages in Figure 6.2 increases linearly with increasing Au wt.% up to 0.6 wt.%, indicating that Au is being deposited on the Ir surface. However, even with higher Au loadings, the entire Ir surface is not covered by Au. This experimental ED profile is similar with the previous observation in Au ED deposition on Pd/SiO_2 [186], which showed that H_2 uptake decreased linearly up to 0.5 wt.% Au deposition and then only marginally decreased at higher Au wt.%. Thus, catalytic deposition (Au on Ir) prevails at the early stage of the process, while auto catalytic deposition (Au on Au) is favored at higher Au loadings due to the decrease in available surface Ir sites. It is also evident from Figure 6.2 that the experimental Au

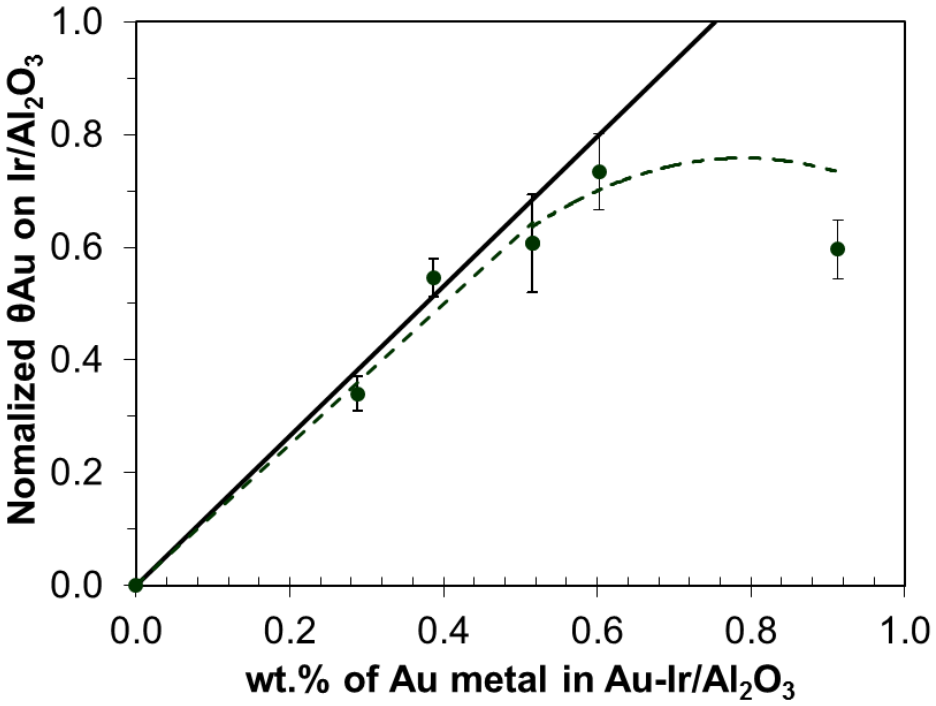

Figure 6.2. Normalized coverage of Au on Ir for Au-Ir/Al_2O_3 bimetallic catalysts derived from H_2 chemisorption data. The solid line is the theoretical plot assuming monodisperse coverage of the Au metal on the Ir surface at a 1:1 deposition stoichiometry.

Table 6.1. Electrolessly deposited weight loadings and surface coverages of Au metal on Ir/Al_2O_3. θ_{mono} refers to theoretical monodisperse layers of Au metal on Ir and $\theta_{expt'l}$ denotes Au coverage determined from chemisorption analysis.

Au-Ir/Al_2O_3, from $Ag(CN)_2^-$		
wt.% Au[a]	θ_{mono}, ML[a]	$\theta_{expt'l}$, ML[b]
0.60	0.80	0.73
0.52	0.68	0.61
0.39	0.51	0.55
0.29	0.38	0.34

[a]Obtained by elemental analysis.

[b]Based on metallic dispersion obtained from H_2 chemisorption data (H per Ir metal).

coverages increased very steeply in the initial stages with increased Au loading, suggesting that ED approach provides a targeted placement of Au on the Ir surface.

FTIR measurement of CO adsorption at room temperature was conducted on the series of Au-Ir/ Al_2O_3 catalysts. The procedure was the same as described in Chapter 5. The FTIR spectra attained after He purge to remove residual gas-phase and weakly asorbed CO are shown in Figure 6.3. Similar spectra for Ag-Ir/ Al_2O_3 have been obtained and discussed in Chapter 5. As expected for Au/ Al_2O_3 [186], CO adsorption is negligible under these conditions. On the other hand, for Ir/ Al_2O_3 and Au-Ir/ Al_2O_3 samples, strong CO stretching bands were observed in 1950-2150 cm^{-1} region, containing several overlapping features. This region can be resolved by curve fitting into peaks at 2012, 2035, 2053, 2078 and 2092 cm^{-1}. These peaks are associated with linearly adsorbed CO species on fully reduced Ir sites (2035, 2053cm^{-1}) or on partially oxidized Ir sites (2092cm^{-1}) or antisymmetric (2012cm^{-1}) or symmetric (2078 cm^{-1}) vibrations of adsorbed dicarbonyl species on Ir ions, respectively. The assignment of these peaks in this spectral region is based on our previous published work [191] and the available literature [95-97, 145].

In the case of bimetallic surfaces, the intensity of the FTIR bands decrease with increasing Au content, indicating lower CO uptake due to electroless deposition of Au on Ir. However, the relative intensity ratios of linear CO adsorption on Ir sites or vibrations of adsorbed dicarbonyl species were not significantly changed with Au deposition, suggesting that Au is indiscriminately deposited on all Ir surface sites. In such a situation, the intensities of all bands would be expected to decrease, but the shape of the spectra would remain roughly constant. Thus, the results suggest that Au electroless deposition

on Ir is not particularly favored on any of the various Ir surface planes or other sites that are exposed. These results are in agreement with the non-specific Ag deposition (using a pH 11 solution with N_2H_4 as the reducing agent) on all Ir sites in the Ag-Ir/Al_2O_3 case discussed in Chapter 5. Thus, the non-discriminatory nature of ED on Ir surfaces may be more due to the nature of Ir rather than the selection of solution pH or reducible metal ion.

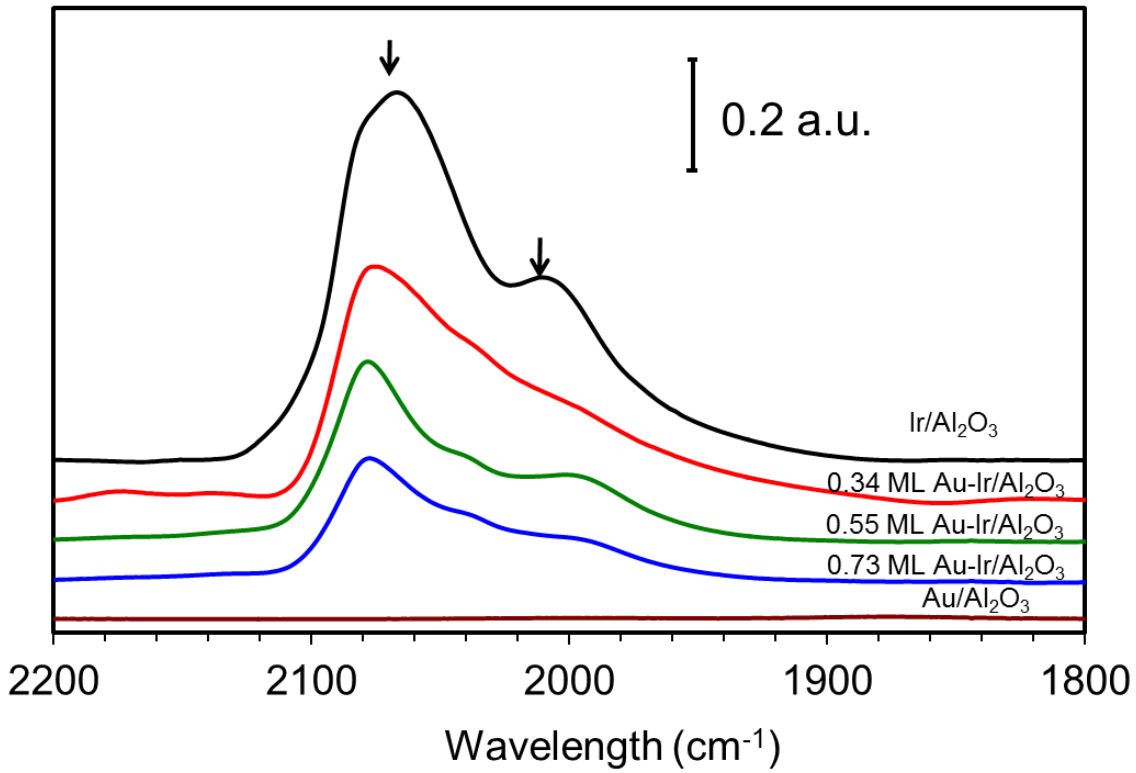

Figure 6.3. Transmission FTIR spectra of CO adsorption on Ir/Al_2O_3, Au/Al_2O_3 and Au-Ir/Al_2O_3 bimetallic catalysts. Arrows highlight peak intensity losses (↓) as Au wt.% increases.

6.3.4 Catalytic Oxidation of CO

In order to evaluate the catalytic activity for the family of alumina supported Au-Ir bimetallic catalysts, CO oxidation was chosen as a probe reaction. As expected, the

activity of the Al_2O_3 support was found to be virtually inactive for CO oxidation at the reaction conditions used in this study.

The conversion of CO as a function of Au weight loading is summarized in Figure 6.4. The Ir/Al_2O_3 catalyst shows a T_{50} (i.e., temperature at 50% CO conversion) of ~218 °C, while the Au/Al_2O_3 shows low levels of activity for CO oxidation based on the lower CO conversion over the entire reaction temperature region. For Au-Ir bimetallic catalysts, on the other hand, catalytic CO oxidation activity declines with increasing Au coverage based on the higher T_{50} values. This is largely because of the Au coverage of active, surface Ir sites. It is known that addition of second metal such as Ag or Au to Group VIII catalysts typically lowers activity for catalytic reactions [192, 193, 229].

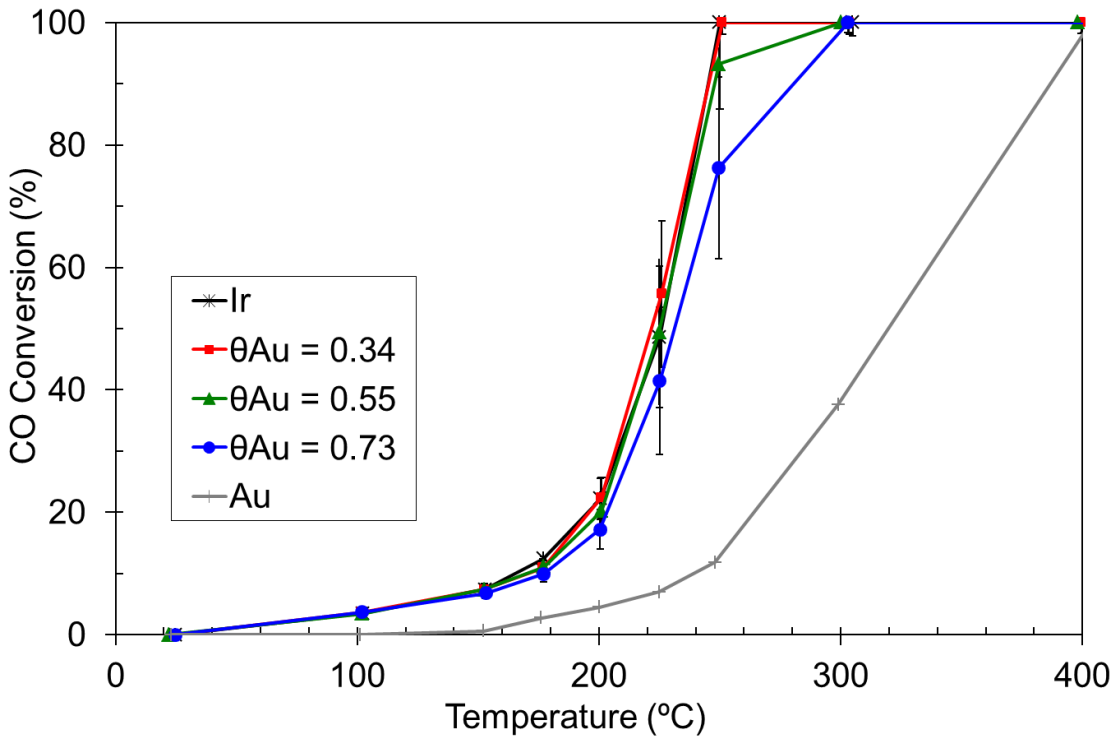

Figure 6.4. Light-off curves of catalytic CO oxidation over Ir/Al_2O_3, Au/Al_2O_3 and Au-Ir/Al_2O_3 bimetallic catalysts.

In order to examine the intrinsic activity of Ir with increasing Au loadings, turnover frequencies (TOFs) for CO conversion were calculated using the exposed Ir sites measured by chemisorption. A reaction temperature of 175 ℃ was chosen for comparison since all of the CO conversions were pseudo-differential at ≤ 20%. Figure 6.5 shows TOFs plotted versus coverage of Au on Ir. For TOF calculations, dispersion obtained by H_2 chemisorption data was converted to get the number of surface Ir sites. On the other hand, for the Au monometallic catalyst the number of Au sites determined based on VSMD of STEM data. As a result, Ir/Al_2O_3 and Au/Al_2O_3 monometallic samples show TOF values of 1.8 and 1.1 s^{-1}, respectively. In the case of $Au\text{-}Ir/Al_2O_3$ bimetallic samples, since it is hard to measure the Au sites that involve the CO oxidation reaction in Au-Ir bimetallic samples, TOF values can be calculated by using only the number of exposed Ir surface sites for bimetallic samples, as shown in Figure 6.5 (a). However, the Au sites in Au-Ir bimetallic samples may have their own TOF and they may contribute to the reaction. If it is assumed that the exposed metal sites (Ir +Au) are roughly constant and equal to the number of surface Ir sites in the monometallic Ir/Al_2O_3 sample, then Figure 6.5 (b) is obtained. These two plots represent how the bimetallic effect looks different based on different TOF analyses. In Figure 6.5 (a), higher Au coverages show higher intrinsic activities and therefore, the bimetallic catalyst with the highest Au coverage has a TOF value that is about a factor of three higher than for monometallic Ir. However, this plot probably makes the bimetallic effect look larger than it actually is. If there is contribution of Au to the activity as shown in this TOF plot, the enhanced performance should be observed over the bimetallic sample in light-off curve in Figure 6.4.

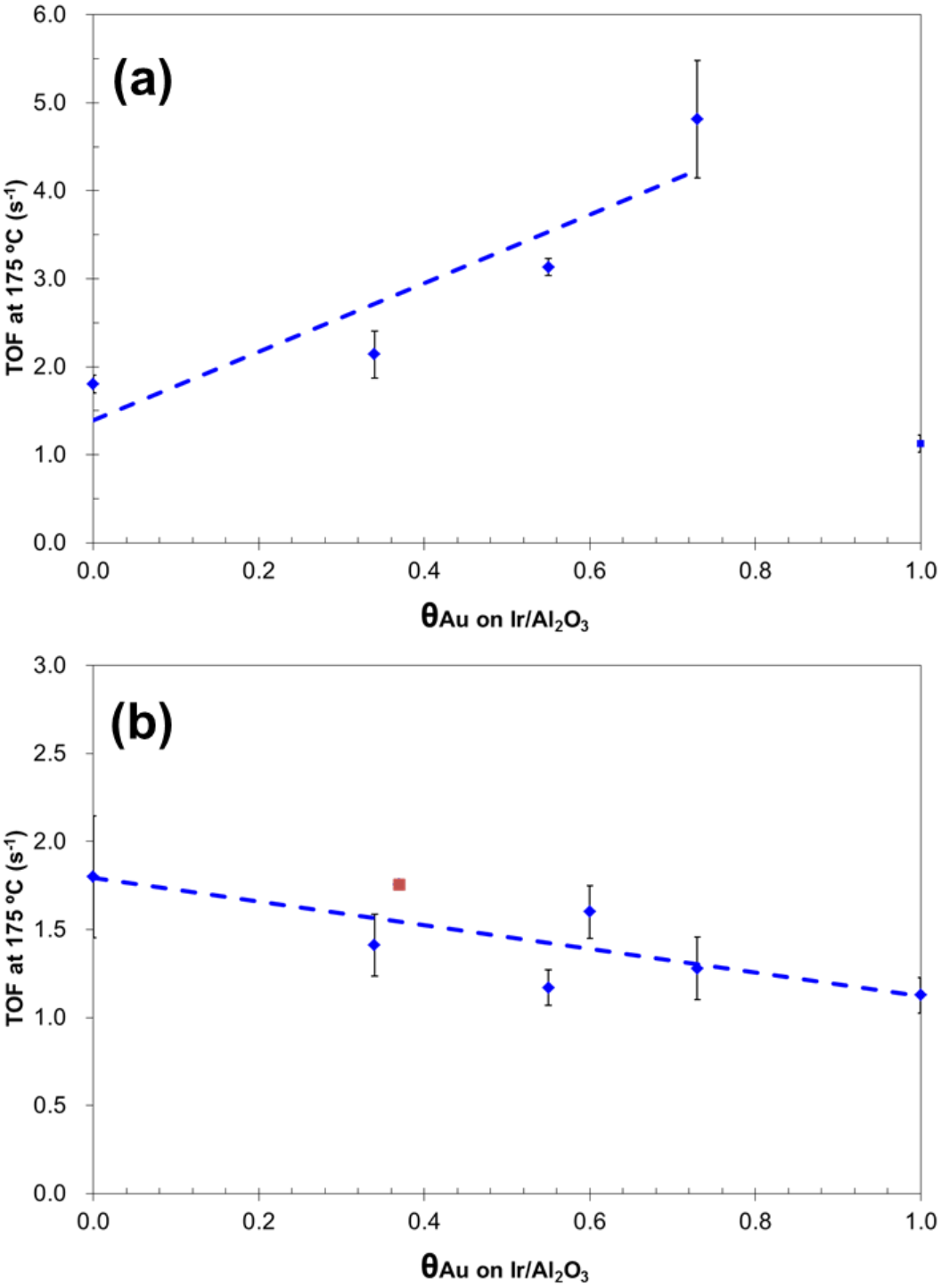

Figure 6.5. TOF of CO oxidation at 175 °C over Ir/Al_2O_3, Ag/Al_2O_3 and $Ag\text{-}Ir/Al_2O_3$ bimetallic catalysts. See text for details.

In contrast, all the Au-Ir bimetallic catalysts lie essectially on the same line with Ir monometallic catalyst. The TOF declines gradually starting from Ir to Au in Figure 6.5 (b), implying almost no bimetallic effect.

As in the case of Ag-Ir (see Chapter 5), any bimetallic effects would arise from a) bimetallic surface that have higher intrinsic activity caused by geometric or electronic effects imposed on primary metal by second metal, b) contribution of bifunctional sites that are catalytically more active than two individual sites. Thus, the presence of any bimetallic effect or not in this Au-Ir system can be further explored by checking these two hypotheses.

If there is an absence of a bimetallic effect in the family of bimetallic ED-derived Au-Ir catalysts, very little electronic interaction between the Ir and Au would be expected. Indeed, there is no binding energy shift is observed for the Ir4f or Au4f XPS peaks regardless of the Au coverage on Ir, as shown in Figure 6.6. In addition, a possible geometric effect for the formation of Au-induced Ir ensembles is also unlikely present based on the lack of any vibrational band shifts in FTIR spectrum with increasing Au coverage.

Bifunctional Au-Ir sites that are catalytically more active by non-competetive adsorption of oxygen and CO to form CO_2 is also implausible. This was confirmed with the related reaction order studies as shown in Figure 6.7. The procedure for detailed kinetics was the same as described in Chapter 5. Briefly, two separate sets of CO-O_2

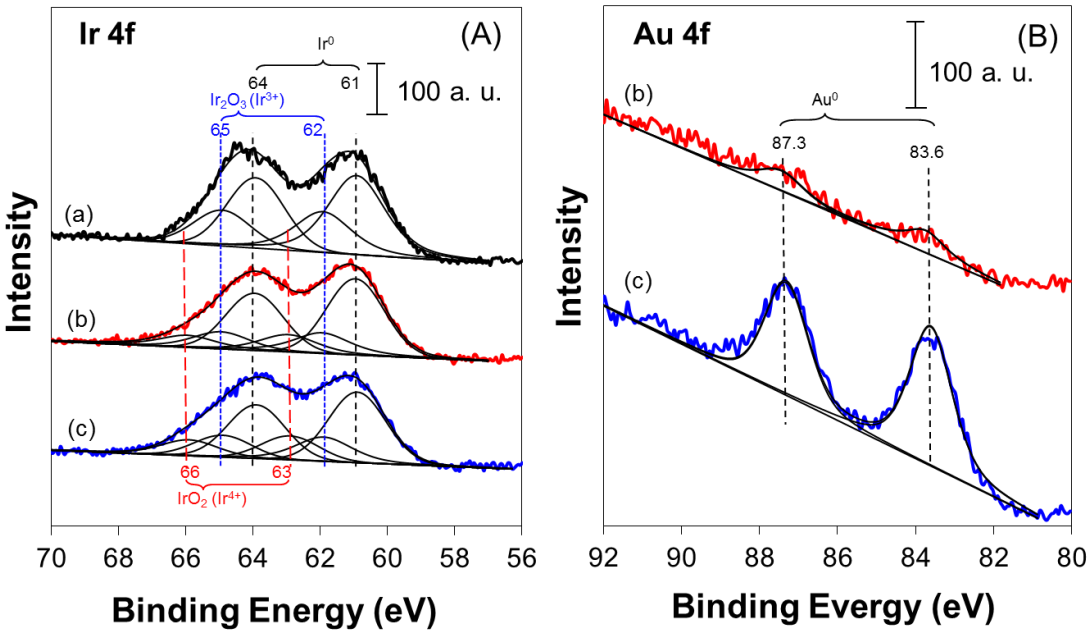

Figure 6.6 XPS data for oxidation state of A) Ir 4f and B) Au 4f on a) Ir/Al_2O_3 and Au-Ir/Al_2O_3 bimetallic catalysts with b) $\theta_{Au} = 0.34$ and c) $\theta_{Au} = 0.73$. See text for details.

reaction experiments were done at 175 °C (a high constant P_{CO} and variable P_{O2}, or a high constant P_{O2} and variable P_{CO}) for the most active Au-Ir bimetallic samples ($\theta_{Au} = 0.34$). When the logarithm of reaction rate of CO_2 formation is plotted with the logarithm of P_{CO} or P_{O2}, the values of the slope yield the reaction order in CO and O_2, respectively. The results are shown in Figure 6.7(a) and (b). As was discussed in Chapter 5, if the reaction rate is governed by a bimetallic Ir-Au interaction, the reaction rate should be zero order in CO and y order in O_2, where y is larger than 0 and smaller than 0.5 (eqn 5.13), like the case for bimetallic Ag-Ir catalyst. However, from the slope values, reaction orders were approximately -1 in CO (Fig 6.7a) and half order in O_2 (Fig 6.7b) over Au-Ir. These values are very similar to what we obtained over monometallic Ir, which showed

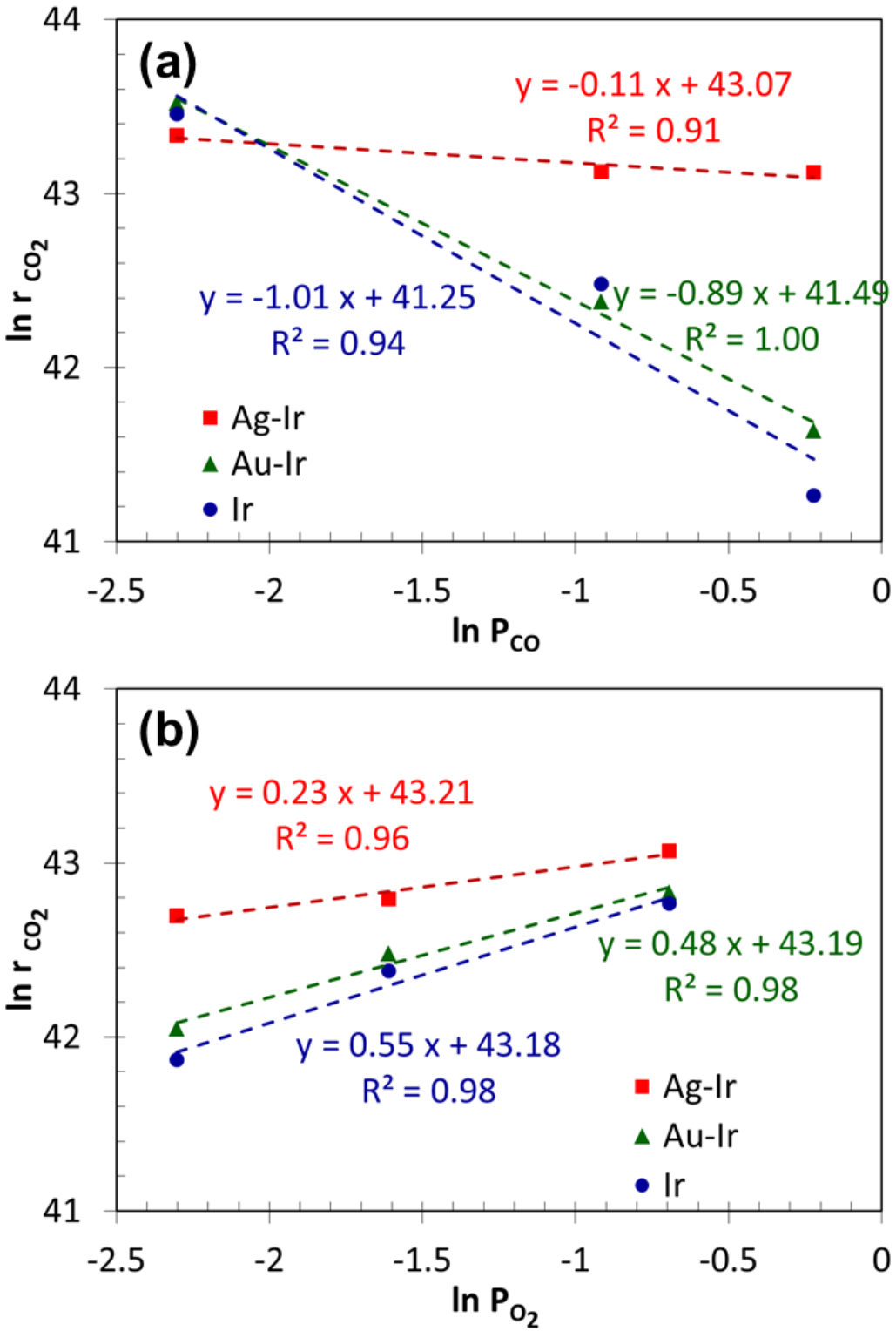

Figure 6.7 CO oxidation reaction order plots at 175 °C for ED-derived Ir/Al_2O_3, Au-Ir/Al_2O_3 (θ_{Au} = 0.34) and Ag-Ir/Al_2O_3 (θ_{Ag} = 0.37) bimetallic catalysts in a) CO and b) O_2.

competitive adsorption of CO and O_2. Thus, it is concluded that a bifunctional effect is not operative for this bimetallic Au-Ir system.

Given the apparent lack of a bimetallic effect in the family of bimetallic ED-derived Au-Ir catalysts, the calculated TOF values for bimetallic Au-Ir samples should appear to look like Figure 6.5 (b).

In our previous work, alumina supported Ir-Au bimetallic catalysts were prepared with different synthetic methods such as dendrimer templating approach (DD) or conventional incipient wetness (CD) and tested for CO oxidation as described in Chapter 3. It would thus be interesting to compare those catalysts with ED-derived Au-Ir catalysts. However, most of dendrimer-derived Ir-Au bimetallic samples (B1R, B2R1 and B2R2) and conventionally-derived Ir-Au-CD sample are not true bimetallic catalysts. They contain a combination of both isolated Ir and Au monometallic and bimetallic particles with varying compositions of the two components on their surface. It is thus not easy to compare or use the same analysis for their activity with ED-derived one. Thus, we decided to look at only Ir-Au-DD (B1NR), since this catalyst was shown to have a bimetallic surface for comparison. The same evaluation of CO oxidation was performed with the MS analyzer as described in Section 2.4.1, and the TOF was calculated in the same way as for the ED-derived samples. In this case, to estimate the coverage of Au on Ir in the B1NR sample, the dispersion estimated from STEM data (68%, Table 3.1) was compared with that estimated by H_2 chemisorption (43%, Table 3.1). Given the disparity, it can be assumed that the surface coverage of Au on Ir (or dilution of Ir sites by Au in a surface alloy) is about 37% **.** Figure 6.5 (b) shows the TOF value for B1NR as a red square. The data point falls on the trend line, indicating that the bimetallic effect is not so

obvious in the Ir-Au bimetallic system regardless of the preparation method. This contrasts the Ir-Ag bimetallic system, which showed a considerable bimetallic effect as a volcano shape curve (Fig 5.5b) due to a bifunctional effect.

The effect of both Au and Ag on activities for the NO-CO reaction was also explored. As shown in Figure 6.8, superior catalytic performance was observed for the entire family of ED-derived Au-Ir and a few of Ag-Ir bimetallic catalysts. This indicates that there is a bimetallic effect in these ED-derived bimetallic catalysts. Figure 6.9 (a) and (b) demonstrate the effect of Au or Ag on the TOFs as function of the second metal coverage for the NO-CO reaction. A very similar improvement of intrinsic activity was observed with some scatter regardless of the type of second metal (i.e., Au or Ag), as shown in Figure 6.9, implying that the Au and Ag seem to play a similar role in the process.

The considerably higher NO-CO reaction rate in bimetallic catalysts could be explained by electronic, ensemble and/or bifunctional effects. With respect to an electronic effect, the chemisorptive properties of a metal overlayer on a dissimilar metal can differ dramatically from those of the parent bulk overlayer metal [230]. For instance, the adsorption energies and dissociative reaction barriers of small molecules such as CO have been correlated with changes in the electronic properties of certain alloy overlayers [231]. However, for the Ir-Au bimetallic system, the work functions for Au and Ir are very similar (5.3 versus 5.7 eV, respectively [232]) and the electronegativities are also not so different (2.54 Au and 2.2 Ir). Furthermore, XPS data imply very limited charge transfer between Ir and Au in Au-Ir bimetallic system, with no peak shifts observed in

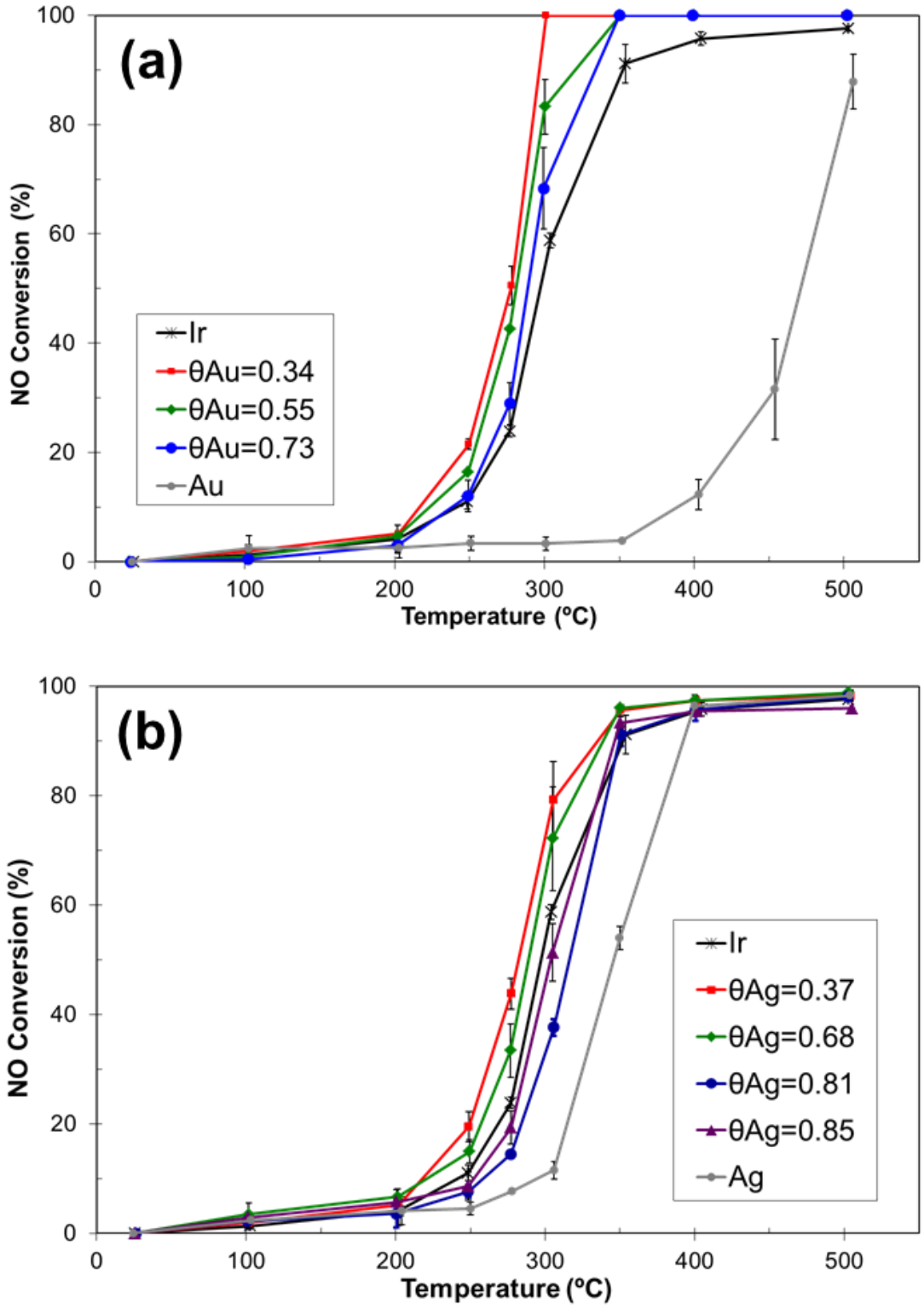

Figure 6.8. Light-off curves of catalytic NO-CO reaction over ED-derived a) Au-Ir/Al_2O_3 and b) Ag-Ir/Al_2O_3 bimetallic catalysts.

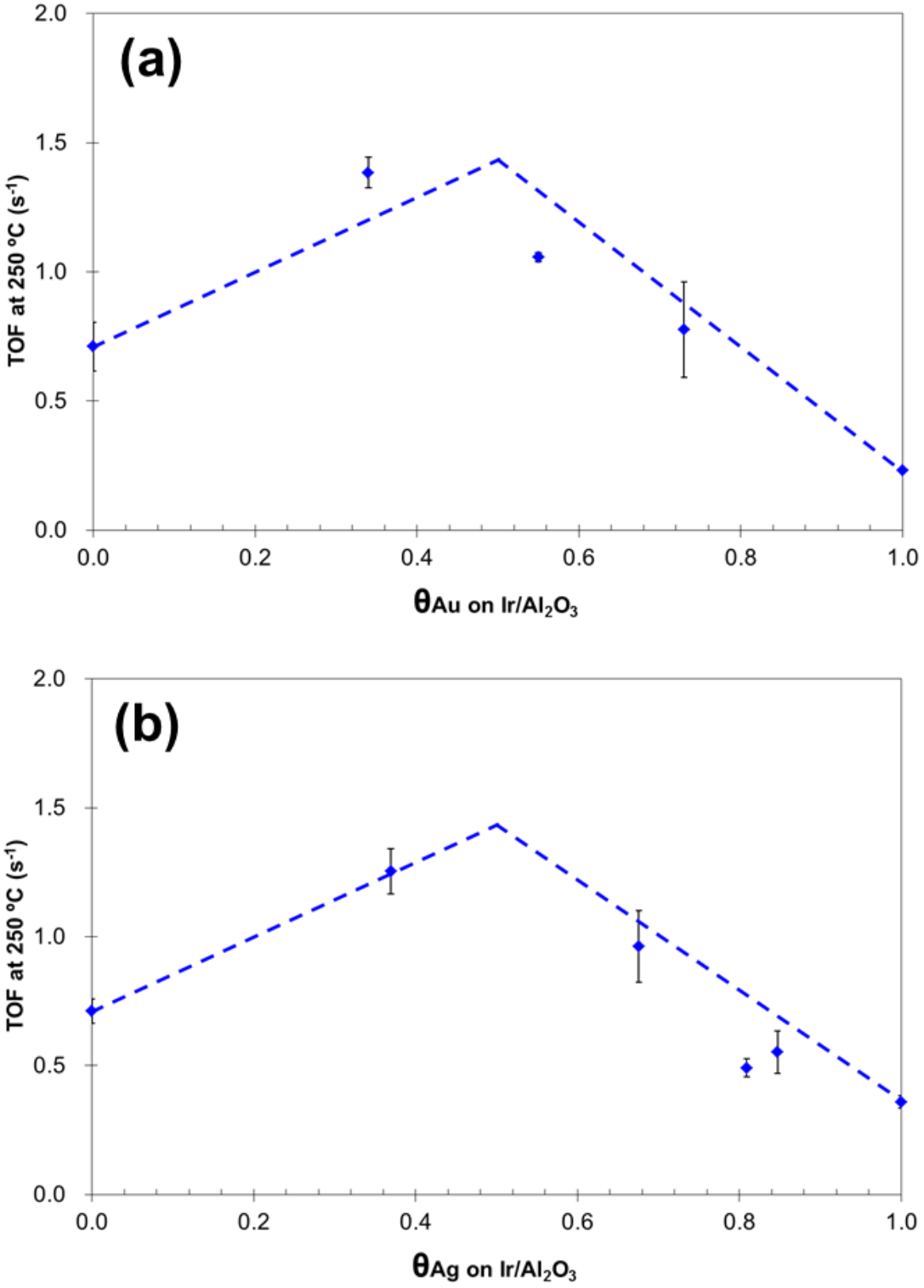

Figure 6.9. TOF of NO-CO reaction at 250 °C over ED-derived a) Au-Ir/Al_2O_3 and b) Ag-Ir/Al_2O_3 bimetallic catalysts.

Figure 6.6. Based on these data, the electronic effects in Au-Ir system seems to be minimal.Although there is some difference between Ag and Ir in terms of the work functions and the electronegativities, an electronic effect appears less probable for Ag-Ir bimetallic system as well, since no binding energy shift is observed for the Ir4f or Ag3d XPS peaks, as shown in Figure 5.7.

It is also unlikely that an ensemble effect is involved for the higher activity for NO-CO reaction over bimetallic catalysts; i.e., the formation of smaller ensembles of Ir surface sites with increasing Au or Ag coverage that strongly favor the formation of more weakly-bound linear CO than the more strongly bound multiful-fold adsorbed species.

It seems that the bifunctional effect is the most plausible explanation for the volcano type curve in the activity with extent of second metal loadings. Related kinetic studies need to be done to explain more details about the process. Nevertheless, TOFs in Figure 6.9 appear to indicate that bifunctional Au-Ir or Ag-Ir sites exist and that they can be maximized at the half coverage point.

6.4 CONCLUSION

A kinetically stable, electroless bath consisting of $Au(CN)_2^-$ and N_2H_4 was developed and optimized in order to selectively deposit the Au on Ir, as opposed to the Al_2O_3, while avoiding formation of undesired Au clusters in solution. A series of ED-derived Ag-Ir bimetallic catalysts have been characterized by using H_2 chemisorption, AA, FTIR, and XPS to reveal several features of the ED process and bimetallic catalyst structure. The extent of decrease in Ir surface sites with increased addition of second

metal indicated that catalytic deposition predominates at lower level of coverage of Au, whereas autocatalytic electroless deposition process (Au^{+} deposition onto Au^{0}) also occurs at higher Au coverages. In addition, the catalytically deposited Au was found to deposit on all types of Ir surface sites in a non-discriminatory fashion, as adjudged by the results of FTIR measurements.

The catalytic performance of these catalysts was evaluated for CO oxidation, and it was found that TOFs for this reaction declined gradually with the elevated fractional corveages of Au on Ir. Such behavior argues for almost no bimetallic effect in this Au-Ir bimetallic system. Furthermore, this is consistent with the result obtained over the dendrimer-derived Ir-Au (B1NR) sample. However, bimetallic Au-Ir catalysts prepared by electroless deposition method result in better catalytic activity for NO-CO reaction compared with Ir monometallic catalyst. NO conversion over Ir/Al_2O_3 was greatly enhanced by the addition of small amounts of Au, which is not very active for NO-CO reaction itself. Higher intrinsic activities were obtained with increasing Au coverage in the bimetallic catalysts, and the highest TOF was obtained at the half point where the Ir-Au pair sites are maximized. Thus, this modification seems to involve a possible bifunctional effect. Interestingly, a very similar improvement of intrinsic activity was observed over bimetallic Ag-Ir catalysts, implying that both Au and Ag appear to play positive role in this process.

Finally, the results reported here demonstrate that ED provides an approach to rationally prepare bimetallic catalysts with controlled composition. Certainly, the present interesting catalytic results for CO oxidation and for NO-CO reaction show the improved

fundamental insight that can be obtained by systematically preparing a wide range of bimetallic compositions with relatively small increments of surface coverage.

CHAPTER 7

CONCLUSION

In the present work, novel synthetic methods such as the dendrimer templating (DD) and electroless deposition (ED) were developed to prepare alumina supported Ir-Au and Ir-Ag bimetallic catalysts. Conventional incipient wetness (CD) was also used for comparison.

Dendrimer derived Ir-Au/Al_2O_3 catalysts showed different metallic dispersions with various particle sizes and distributions, depending on the preparation synthetic routes. Ir-Au-B1NR bimetallic catalyst, which was prepared thru complexation of Ir and Au metal ion sequentially with dendrimer solution, shows considerably uniform particle size distribution with higher dispersion compared to the others. This indicates that the PAMAM dendrimer probably not only acts as a stabilizer in solution but it also prevents growth metal particle size during the heat treatment. As a result, the Ir-Au-B1NR represented enhanced catalytic performance toward oxidation of CO compared with Ir monometallic catalyst and better activity for NO-CO reaction and NO decomposition then conventionally derived one.

On the other hand, a series of alumina supported Ag-Ir and Au-Ir bimetallic catalysts having controlled and incremental coverages of Ag or Au, have been successfully prepared via ED method using hydrazine as a reducing agent. STEM study

showed the highly dispersed Ir/γ-Al_2O_3 monometallic catalyst (volume-surface mean diameter of 1.1 nm) with narrow particle size distribution which makes this base catalyst to be a good starting material for Ag or Au deposition. Hydrogen chemisorption was investigated on bimetallic catalysts with different Ag (or Au) wt loading to determine the coverage of Ag (or Au) on Ir metal. Moreover, in situ FTIR of CO adsorption allowed for identification of exposed metal surface area in the bimetallic catalysts, suggesting that Ag and Au metal was similarly deposited on all types of Ir surface sites in a non-discriminatory fashion. In contrast, kinetic studies of CO oxidation revealed different result for Ag-Ir and Au-Ir bimetallic system. It was clear to see the bimetallic effect in Ag-Ir bimetallic system; thus, the highest TOF was obtained at the half point in Ag-Ir bimetallic catalysts where the Ir-Ag pair sites are maximized. In case of Au-Ir bimetallic catalysts, on the other hand, higher coverages of Au resulted in lower turnover frequencies (TOFs).

Among the several different techniques, ED method allowed the advanced fundamental studies possible by providing a systematic approach to prepare bimetallic catalysts with targeted compositions and surface coverage. It was found that the catalytic properties of metal strongly depend on the preparation methods, which bring about a great difference in the size of particles and the surface configuration of two metals. These differences result in enhanced catalytic results that can be explained by a combination of bifunctional, electronic, and geometric effects. In particular, for the ED catalysts a bifunctional effect is likely to be the governing factor in these systems.

REFERENCES

[1] G. Ertl, H. Knoezinger, J. Weitkamp, Handbook of heterogeneous catalysis, Wiley-VCH, Weinheim, 1997.
[2] R.A.v. Santen, J.W. Niemantsverdriet, Chemical kinetics and catalysis, Plenum Press, New York, 1995.
[3] H.H. Kung, M.C. Kung, Top. Catal. , 34 (2005) 77-83.
[4] G. Ertl, K. H., W. J., Preparation of solid catalysts, Wiley-VCH, Weinheim; New York, 1999.
[5] A. Roucoux, J. Schulz, H. Patin, Chem. Rev., 102 (2002) 3757-3778.
[6] B.C. Gates, L. Guczi, H. Knözinger, Metal clusters in catalysis, Elsevier ; Distributors for the U.S.A. and Canada, Elsevier Science Pub. Co., Amsterdam; New York; New York, NY, U.S.A., 1986.
[7] R.W.J. Scott, O.M. Wilson, S.K. Oh, E.A. Kenik, R.M. Crooks, J. Am. Chem. Soc. , 126 (2004) 15583-15591.
[8] T. Nakatsuji, Appl. Catal., B 25 (2000) 163-179.
[9] P. Reyes, H. Rojas, J.L.G. Fierro, Appl. Catal., A, 248 (2003) 59-65.
[10] H. Rojas, G. Borda, J.J. Martinez, J. Valencia, P. Reyes, J. Mol. Catal. A: Chem. , 286 (2008) 70-78.
[11] G.S. Fonseca, A.P. Umpierre, P.F.P. Fichtner, S.R. Teixeira, J. Dupont, Chem. Eur. J. , 9 (2003) 3263-3269.
[12] F.R. Hartley, Chemistry of the platinum group metals : recent developments, Elsevier, Amsterdam; New York, 1991.
[13] J.A. Rodriguez, Surf. Sci. Rep. , 24 (1996) 225-287.
[14] W.M.H. Sachtler, Appl. Surf. Sci., 19 (1984) 167-180.
[15] M. Kuhn, J.A. Rodriguez, J Catal, 154 (1995) 355-363.
[16] J.M. Frechet, Science, 263 (1994) 1710-1715.
[17] R.M. Crooks, B.I. Lemon, L. Sun, L.K. Yeung, M.Q. Zhao, Top. Curr. Chem. , 212 (2001) 81-135.
[18] R.M. Crooks, M.Q. Zhao, L. Sun, V. Chechik, L.K. Yeung, Acc. Chem. Res. , 34 (2001) 181-190.
[19] H.G. Lang, S. Maldonado, K.J. Stevenson, B.D. Chandler, J. Am. Chem. Soc. , 126 (2004) 12949-12956.
[20] H.F. Lang, R.A. May, B.L. Iversen, B.D. Chandler, J. Am. Chem. Soc. , 125 (2003) 14832-14836.
[21] D.X. Liu, J.X. Gao, C.J. Murphy, C.T. Williams, J. Phys. Chem. B, 108 (2004) 12911-12916.
[22] D.S. Deutsch, G. Lafaye, D.X. Liu, B. Chandler, C.T. Williams, M.D. Amiridis, Catal. Lett. , 97 (2004) 139-143.
[23] L.W. Beakley, S.E. Yost, R. Cheng, B.D. Chandler, Appl. Catal., A, 292 (2005) 124-129.

[24] A. Singh, B.D. Chandler, Langmuir, 21 (2005) 10776-10782.
[25] H.C. Ye, R.W.J. Scott, R.M. Crooks, Langmuir, 20 (2004) 2915-2920.
[26] R.W.J. Scott, C. Sivadinarayana, O.M. Wilson, Z. Yan, D.W. Goodman, R.M. Crooks, J. Am. Chem. Soc. , 127 (2005) 1380-1381.
[27] G. Lafaye, C.T. Williams, M.D. Amiridis, Catal. Lett. , 96 (2004) 43-47.
[28] G. Lafaye, A. Siani, P. Marecot, M.D. Amiridis, C.T. Williams, J. Phys. Chem. B, 110 (2006) 7725-7731.
[29] F.W. Zeng, S.C. Zimmerman, Chem. Rev., 97 (1997) 1681-1712.
[30] V. Chechik, M.Q. Zhao, R.M. Crooks, J. Am. Chem. Soc. , 121 (1999) 4910-4911.
[31] R.W.J. Scott, O.M. Wilson, R.M. Crooks, J. Phys. Chem. B, 109 (2005) 692-704.
[32] M. Maciejewski, E. Bednarek, J. Janiszewska, J. Janiszewski, G. Szczygiel, M. Zapora, J. Macromol. Sci., Pure Appl. Chem. , 37 (2000) 753-783.
[33] M.F. Ottaviani, F. Montalti, N.J. Turro, D.A. Tomalia, J. Phys. Chem. B, 101 (1997) 158-166.
[34] M.Q. Zhao, L. Sun, R.M. Crooks, J. Am. Chem. Soc. , 120 (1998) 4877-4878.
[35] M.Q. Zhao, R.M. Crooks, Adv. Mater., 11 (1999) 217-+.
[36] M.Q. Zhao, R.M. Crooks, Angew. Chem. Int. Edit., 38 (1999) 364-366.
[37] M.Q. Zhao, R.M. Crooks, Chem. Mater., 11 (1999) 3379-3385.
[38] L. Balogh, D.A. Tomalia, J. Am. Chem. Soc. , 120 (1998) 7355-7356.
[39] K. Esumi, R. Nakamura, A. Suzuki, K. Torigoe, Langmuir, 16 (2000) 7842-7846.
[40] K. Esumi, A. Suzuki, N. Aihara, K. Usui, K. Torigoe, Langmuir, 14 (1998) 3157-3159.
[41] A. Manna, T. Imae, K. Aoi, M. Okada, T. Yogo, Chem. Mater., 13 (2001) 1674-1681.
[42] R.W.J. Scott, A.K. Datye, R.M. Crooks, J. Am. Chem. Soc., 125 (2003) 3708-3709.
[43] Y.M. Chung, H.K. Rhee, J. Mol. Catal. A: Chem. , 206 (2003) 291-298.
[44] Y.M. Chung, H.K. Rhee, J. Colloid. Interf. Sci., 271 (2004) 131-135.
[45] Y.M. Chung, H.K. Rhee, Catal. Lett. , 85 (2003) 159-164.
[46] R.W.J. Scott, O.M. Wilson, R.M. Crooks, Chem. Mater., 16 (2004) 5682-5688.
[47] D.X. Liu, Y.M. Lopez-De Jesus, J.R. Monnier, C.T. Williams, J Catal, 269 (2010) 376-387.
[48] H. Xie, J.Y. Howe, V. Schwartz, J.R. Monnier, C.T. Williams, H.J. Ploehn, J Catal, 259 (2008) 111-122.
[49] O.J. Murphy, S. Srinivasan, B.E. Conway, Electrochemistry in transition : from the 20th to the 21st century, in: American Chemical Society Meeting, Plenum Press, New York, 1992.
[50] M.D. Maksimovic, S.S. Djokic, Surf. Coat. Tech., 31 (1987) 325-334.
[51] B.D. Barker, Surf. Technol., 12 (1981) 77-88.
[52] S.S. Djokic, N.S. Djokic, J. Electrochem. Soc., 158 (2011) D204-D209.
[53] C. Kerr, D. Barker, F. Walsh, Trans. IMF, 79 (2001) 41-46.
[54] W. Riedel, Electroless nickel plating, ASM International ; Finishing Publications, Metals Park, Ohio; Stevenage, England, 1991.
[55] I. Ohno, Mater. Sci. Eng., A 146 (1991) 33-49.
[56] D.C. Harris, Quantitative chemical analysis, W.H. Freeman, New York, 1999.
[57] G.O. Mallory, J.B. Hajdu, Electroless plating fundamentals and applications, AESF ; Noyes Publications/William Andrew Pub., Orlando, Fla.; New York, 1990.

[58] O.S. Alexeev, A. Siani, G. Lafaye, C.T. Williams, H.J. Ploehn, M.D. Amiridis, J. Phys. Chem. B, 110 (2006) 24903-24914.
[59] D.S. Deutsch, A. Siani, P.T. Fanson, H. Hirata, S. Matsumoto, C.T. Williams, M.D. Amiridis, J. Phys. Chem. C, 111 (2007) 4246-4255.
[60] D.S. Deutsch, C.T. Williams, M.D. Amiridis, Catalyst preparation : science and engineering, CRC Press/Taylor & Francis, Boca Raton, 2007.
[61] H. Xie, J.Y. Howe, V. Schwartz, J.R. Monnier, C.T. Williams, H.J. Ploehn, J Catal, 259 (2008) 111-122.
[62] Y.M. López-De Jesús, C.E. Johnson, J.R. Monnier, C.T. Williams, Top. Catal., 53 (2010) 1132-1137.
[63] I. Langmuir, T. Faraday Soc., 17 (1922) 0621-0654.
[64] R.P. Eischens, W.A. Pliskin, Adv. Catal., 9 (1957) 662-668.
[65] J.A. Rodriguez, D.W. Goodman, Surf. Sci. Rep., 14 (1991) 1-107.
[66] D.W. Goodman, Chem. Rev. , 95 (1995) 523-536.
[67] N.W. Cant, D.E. Angove, J Catal, 97 (1986) 36-42.
[68] J.T. Kummer, J. Phys. Chem. , 90 (1986) 4747-4752.
[69] J.N. Armor, Appl. Catal. A 176 (1999) 159-176.
[70] S.H. Oh, C.C. Eickel, J Catal, 112 (1988) 543-555.
[71] D.M. Haaland, F.L. Williams, J Catal, 76 (1982) 450-465.
[72] N.W. Cant, R.A. Donaldson, J Catal, 71 (1981) 320-330.
[73] D.J. Kaul, E.E. Wolf, J Catal, 89 (1984) 348-361.
[74] J. Szanyi, D.W. Goodman, J. Phys. Chem., 98 (1994) 2972-2977.
[75] S. Volkening, J. Wintterlin, J. Phys. Chem., 114 (2001) 6382-6395.
[76] A. Gomez-Cortes, G. Diaz, R. Zanella, H. Ramirez, P. Santiago, J.M. Saniger, J. Phys. Chem. C, 113 (2009) 9710-9720.
[77] R. Zanella, S. Giorgio, C.H. Shin, C.R. Henry, C. Louis, J Catal, 222 (2004) 357-367.
[78] M. Haruta, Catal. Today, 36 (1997) 153-166.
[79] X. Bokhimi, R. Zanella, A. Morales, J. phys. Chem. C, 112 (2008) 12463-12467.
[80] S. Biella, F. Porta, L. Prati, M. Rossi, Catal. Lett., 90 (2003) 23-29.
[81] M.T. Schaal, J. Rebelli, H.M. McKerrow, C.T. Williams, J.R. Monnier, Appl. Catal., A 382 (2010) 49-57.
[82] D.S. Deutsch, in, University of South Carolina, 2006.
[83] R.J. Chimentao, G.R. Valenca, F. Medina, J. Perez-Ramirez, Appl. Surf. Sci., 253 (2007) 5888-5893.
[84] J.R. Anderson, Structure of metallic catalysts, Academic Press, London; New York, 1975.
[85] Z.P. Liu, S.J. Jenkins, D.A. King, Phys. Rev. Lett., 93 (2004).
[86] T. Akita, M. Okumura, K. Tanaka, S. Tsubota, M. Haruta, J. Electron Microsc., 52 (2003) 119-124.
[87] M. Haruta, M. Date, Appl. Catal. A, 222 (2001) 427-437.
[88] Y. Iizuka, H. Fujiki, N. Yamauchi, T. Chijiiwa, S. Arai, S. Tsubota, M. Haruta, Catal. Today, 36 (1997) 115-123.
[89] Y.M. López-De Jesús, A. Vicente, G. Lafaye, P. Marecot, C.T. Williams, J. Phys. Chem. C, 112 (2008) 13837-13845.
[90] A. Bourane, M. Nawdali, D. Bianchi, J. Phys. Chem. B, 106 (2002) 2665-2671.
[91] P. Gelin, G. Coudurier, Y. Bentaarit, C. Naccache, J Catal, 70 (1981) 32-40.

[92] A. Erdohelyi, K. Fodor, G. Suru, Appl. Catal., A 139 (1996) 131-147.
[93] F. Solymosi, E. Novak, A. Molnar, J. Phys. Chem. , 94 (1990) 7250-7255.
[94] R.F. Howe, J Catal, 50 (1977) 196-199.
[95] L. Lynds, Spectrochim. Acta, 20 (1964) 1369-1372.
[96] F. Solymosi, J. Rasko, J Catal, 62 (1980) 253-263.
[97] T.I. Koranyi, J. Mihaly, E. Pfeifer, C. Nemeth, T. Yuzhakova, J. Mink, J. Phys. Chem. A, 110 (2006) 1817-1823.
[98] A. Erdohelyi, K. Fodor, G. Suru, Appl. Catal., A, 139 (1996) 131-147.
[99] W.S. Zhang, A.Q. Wang, L. Li, X.D. Wang, T. Zhang, Catal. Lett., 121 (2008) 319-323.
[100] M. Okumura, N. Masuyama, E. Konishi, S. Ichikawa, T. Akita, J Catal, 208 (2002) 485-489.
[101] Y. Huang, A. Wang, L. Li, X. Wang, D. Su, T. Zhang, J Catal, 255 (2008) 144-152.
[102] W.S. Zhang, A.Q. Wang, L. Li, X.D. Wang, T. Zhang, Catal. Today, 131 (2008) 457-463.
[103] S. Nojima, S. Yasutake, S. Watanabe, M. Yonemura, in: J. Patent (Ed.), Japan, 2002.
[104] F. Maroun, F. Ozanam, O.M. Magnussen, R.J. Behm, Science, 293 (2001) 1811-1814.
[105] X. Bokhimi, R. Zanella, C. Angeles-Chavez, J. Phys. Chem. C, 114 (2010) 14101-14109.
[106] A. Fritz, V. Pitchon, Appl. Catal., B, 13 (1997) 1-25.
[107] H.S. Glick, J.J. Klein, W. Squire, J. Chem. Phys. , 27 (1957) 850-857.
[108] J.W. Hightower, D.A.V. Leirsburg, The catalytic chemistry of nitrogen oxides, in: R.L. Klimisch, J.G. Larson (Eds.), Plenum Press, New York, 1975, pp. 63.
[109] F. Garin, Appl. Catal., A, 222 (2001) 183-219.
[110] A. Gervasini, P. Carniti, V. Ragaini, Appl. Catal., B, 22 (1999) 201-213.
[111] R. Burch, T.C. Watling, Catal. Lett. , 37 (1996) 51-55.
[112] S.J. Tauster, L.L. Murrell, J Catal, 41 (1976) 192-195.
[113] K.C. Taylor, J.C. Schlatter, J Catal, 63 (1980) 53-71.
[114] P. Biloen, F.M. Dautzenberg, W.M.H. Sachtler, J Catal, 50 (1977) 77-86.
[115] V. Ponec, G.C. Bond, Stud. Surf. Sci. Catal. , 95 (1995) 1-5.
[116] M. Kuhn, J.A. Rodriguez, J Catal, 154 (1995) 355-363.
[117] W.M.H. Sachtler, Appl. Surf. Sci. , 19 (1984) 167-180.
[118] S.-L. Peng, L.-Y. Gan, R.-Y. Tian, Y.-J. Zhao, Comput. Theor. Chem., 977 (2011) 62-68.
[119] J.-a. Wang, G. Aguilar-Rios, R. Wang, Appl. Surf. Sci. , 147 (1999) 44-51.
[120] T. Yoshinari, K. Sato, M. Haneda, Y. Kintaichi, H. Hamada, Catal. Commun. , 2 (2001) 155-158.
[121] T. Yoshinari, K. Sato, M. Haneda, Y. Kintaichi, H. Hamada, Appl. Catal., B, 41 (2003) 157-169.
[122] M. Nawdali, E. Iojoiu, P. Gelin, H. Praliaud, M. Primet, Appl. Catal., A, 220 (2001) 129-139.
[123] M. Nawdali, H. Praliaud, M. Primet, Top. Catal. , 16 (2001) 199-204.
[124] T. Nakatsuji, Appl. Catal., B, 25 (2000) 163-179.

[125] C. Wogerbauer, M. Maciejewski, A. Baiker, U. Gobel, Top. Catal. , 16 (2001) 181-186.
[126] E. Iojoiu, P. Gelin, H. Praliaud, M. Primet, Appl. Catal., A, 263 (2004) 39-48.
[127] C. Wogerbauer, M. Maciejewski, A. Baiker, Appl. Catal., B, 34 (2001) 11-27.
[128] C. Wogerbauer, M. Maciejewski, A. Baiker, U. Gobel, J Catal, 201 (2001) 113-127.
[129] C. Wogerbauer, M. Maciejewski, A. Baiker, J Catal, 205 (2002) 157-167.
[130] A.Q. Wang, L. Ma, Y. Cong, T. Zhang, D.B. Liang, Appl. Catal., B, 40 (2003) 319-329.
[131] A.Q. Wang, D.B. Liang, C.H. Xu, X.Y. Sun, T. Zhang, Appl. Catal., B, 32 (2001) 205-212.
[132] D.A. Tomalia, A.M. Naylor, W.A.I. Goddard, Angew. Chem. Int. Ed. , 29 (1990) 138-175.
[133] D.S. Deutsch, G. Lafaye, D.X. Liu, B. Chandler, C.T. Williams, M.D. Amiridis, Catal. Lett. , 97 (2004) 139-143.
[134] H.F. Lang, R.A. May, B.L. Iversen, B.D. Chandler, J. Am. Chem. Soc. , 125 (2003) 14832-14836.
[135] Y.-J. Song, Y.M. López-De Jesús, P.T. Fanson, C.T. Williams, J. Phys. Chem. C, 117 (2013) 10999-11007.
[136] Y.M. López-De Jesús, A. Vicente, G. Lafaye, P. Marecot, C.T. Williams, J. Phys. Chem. C, 112 (2008) 13837-13845.
[137] G. Lafaye, C.T. Williams, M.D. Amiridis, Catal. Lett. , 96 (2004) 43-47.
[138] M. Nemanashi, R. Meijboom, J. Colloid Interface Sci. , 389 (2013) 260-267.
[139] G. Lafaye, C.T. Williams, M.D. Amiridis, Catal. Lett., 96 (2004) 43-47.
[140] M. Haruta, Catal. Today 36 (1997) 153-166.
[141] Y. Iizuka, H. Fujiki, N. Yamauchi, T. Chijiiwa, S. Arai, S. Tsubota, M. Haruta, Catal. Today 36 (1997) 115-123.
[142] M. Haruta, M. Date, Appl. Catal., A, 222 (2001) 427-437.
[143] F. Solymosi, J. Rasko, J Catal, 62 (1980) 253-263.
[144] J.B. Lefers, P.J. Van den Berg, Anal. Chem. , 52 (1980) 1424-1426.
[145] A. Bourane, M. Nawdali, D. Bianchi, J. Phys. Chem. B, 106 (2002) 2665-2671.
[146] P. Gelin, G. Coudurier, Y. Bentaarit, C. Naccache, J Catal, 70 (1981) 32-40.
[147] C.R. Guerra, J.H. Schulman, Surf. Sci., 7 (1967) 229-249.
[148] L. Lynds, Spectrochim. Acta 20 (1964) 1369-1372.
[149] F.J.C.M. Toolenaar, A.G.T.M. Bastein, V. Ponec, J Catal, 82 (1983) 35-44.
[150] A.A. Davydov, Infrared spectroscopy of adsorbed species on the surface of transition metal oxides, Wiley, Chichester; New York, 1990.
[151] R.J. Wu, T.Y. Chou, C.T. Yeh, Appl. Catal., B, 6 (1995) 105-116.
[152] S. Qun, L. Landong, H. Zhengping, X. Zhi Ping, Appl. Catal., B, 84 (2008) 734-741.
[153] J.H. Holles, R.J. Davis, T.M. Murray, J.M. Howe, J Catal, 195 (2000) 193-206.
[154] H. Permana, K.Y. Simon Ng, C.H.F. Peden, S.J. Schmieg, D.K. Lambert, D.N. Belton, Catal. Lett. , 47 (1997) 5-15.
[155] C. Shi, M. Cheng, Z. Qu, X. Yang, X. Bao, Appl. Catal., B, 36 (2002) 173-182.
[156] J.T. Wrobleski, M. Boudart, Catal. Today, 15 (1992) 349-360.
[157] B.D. Chandler, L.H. Pignolet, Catal. Today, 65 (2001) 39-50.

[158] J.H. Sinfelt, Bimetallic catalysts : discoveries, concepts, and applications, Wiley, New York, 1983.
[159] S.S. Djokic, Electroless Deposition of Metals and Alloys, in: B. Conway, R. White (Eds.) Mod. Aspect. Electroc., Springer US, 2002, pp. 51-133.
[160] M.T. Schaal, A.Y. Metcalf, J.H. Montoya, J.P. Wilkinson, C.C. Stork, C.T. Williams, J.R. Monnier, Catal. Today, 123 (2007) 142-150.
[161] G. Elshobak, P.C. Gravelle, S.J. Teichner, J Catal, 14 (1969) 4-22.
[162] L.F. Razon, R.A. Schmitz, Cat. Rev. - Sci. Eng. , 28 (1986) 89-164.
[163] E. Gulari, C. Guldur, S. Srivannavit, S. Osuwan, Appl. Catal., A 182 (1999) 147-163.
[164] S.D. Gardner, G.B. Hoflund, D.R. Schryer, J. Schryer, B.T. Upchurch, E.J. Kielin, Langmuir, 7 (1991) 2135-2139.
[165] S.D. Gardner, G.B. Hoflund, B.T. Upchurch, D.R. Schryer, E.J. Kielin, J. Schryer, J Catal, 129 (1991) 114-120.
[166] P.A. Wright, S. Natarajan, J.M. Thomas, P.L. Gaiboyes, Chem. Mater. , 4 (1992) 1053-1065.
[167] L.G. Tejuca, J.L.G. Fierro, J.M.D. Tascon, Adv. Catal., 36 (1989) 237-328.
[168] M.M. Gadgil, R. Sasikala, S.K. Kulshreshtha, J. Mol. Catal. , 87 (1994) 297-309.
[169] R.K. Herz, S.P. Marin, J Catal, 65 (1980) 281-296.
[170] N.W. Cant, R.A. Donaldson, J Catal, 71 (1981) 320-330.
[171] D.M. Haaland, F.L. Williams, J Catal, 76 (1982) 450-465.
[172] D.J. Kaul, E.E. Wolf, J Catal, 89 (1984) 348-361.
[173] S.H. Oh, C.C. Eickel, J Catal, 112 (1988) 543-555.
[174] J. Szanyi, D.W. Goodman, J. Phys. Chem., 98 (1994) 2972-2977.
[175] S. Volkening, J. Wintterlin, J. Chem. Phys. , 114 (2001) 6382-6395.
[176] M.J. Kahlich, H.A. Gasteiger, R.J. Behm, J Catal, 171 (1997) 93-105.
[177] M.M. Schubert, M.J. Kahlich, H.A. Gasteiger, R.J. Behm, J. Power Sources 84 (1999) 175-182.
[178] A. Gomez-Cortes, G. Diaz, R. Zanella, H. Ramirez, P. Santiago, J.M. Saniger, J. Phys. Chem. C, 113 (2009) 9710-9720.
[179] L.M. Molina, M.D. Rasmussen, B. Hammer, J. Chem. Phys. , 120 (2004) 7673-7680.
[180] A. Nagy, G. Mestl, Appl. Catal., A 188 (1999) 337-353.
[181] J.A. Schwarz, C. Contescu, A. Contescu, Chem. Rev. , 95 (1995) 477-510.
[182] K.D. Beard, J.W. Van Zee, J.R. Monnier, Appl. Catal., B, 88 (2009) 185-193.
[183] M. Schaal, A. Pickerell, C. Williams, J. Monnier, J Catal, 254 (2008) 131-143.
[184] Y. Okinaka, T. Osaka, Electroless Deposition Processes: Fundamentals and Applications, in: Advances in Electrochemical Science and Engineering, Wiley-VCH Verlag GmbH, 2008, pp. 55-116.
[185] G.O. Mallory, J.B. Hajdu, Electroless plating fundamentals and applications, in, AESF ; Noyes Publications/William Andrew Pub., Orlando, Fl; New York, 1990.
[186] J. Rebelli, M. Detwiler, S. Ma, C.T. Williams, J.R. Monnier, J Catal, 270 (2010) 224-233.
[187] J. Rebelli, A.A. Rodriguez, S. Ma, C.T. Williams, J.R. Monnier, Catal. Today, 160 (2011) 170-178.
[188] C. Mijoule, V. Russier, Surf. Sci., 254 (1991) 329-340.

[189] S. Yuvaraj, S.C. Chow, C.T. Yeh, J Catal, 198 (2001) 187-194.
[190] J.A. Rodriguez, C.M. Truong, D.W. Goodman, Surf. Sci., 271 (1992) L331-L337.
[191] Y.-J. Song, Y.M. López-De Jesús, P.T. Fanson, C.T. Williams, J. Phys. Chem. C, 117 (2013) 10999-11007.
[192] F.H.B. Lima, C.D. Sanches, E.A. Ticianelli, J. Electrochem. Soc. , 152 (2005) A1466-A1473.
[193] R. Ryoo, C. Pak, S.J. Cho, Jpn. J. Appl. Phys., 32 (1993) 475-477.
[194] M. Chatenet, M. Aurousseau, R. Durand, F. Andolfatto, J. Electrochem. Soc. , 150 (2003) D47-D55.
[195] D.E. Mears, Ind. Eng. Chem. Process. Des. Dev., 10 (1971) 541-&.
[196] P.B. Weisz, C.D. Prater, Adv. Catal., 6 (1954) 143-196.
[197] A. Pachulski, R. Schodel, P. Claus, Appl. Catal. A, 445 (2012) 107-120.
[198] S.T. Oyama, X.M. Zhang, J.Q. Lu, Y.F. Gu, T. Fujitani, J Catal, 257 (2008) 1-4.
[199] S.R. Seyedmonir, D.E. Strohmayer, G.J. Guskey, G.L. Geoffroy, M.A. Vannice, J Catal, 93 (1985) 288-302.
[200] A.B. Dongil, B. Bachiller-Baeza, I. Rodriguez-Ramos, A. Guerrero-Ruiz, C. Mondelli, A. Baiker, Appl. Catal., A, 451 (2013) 14-20.
[201] J.M. Guil, J.E.H. Garcia, A.R. Paniego, J.M.T. Menayo, Top. Catal. , 19 (2002) 313-321.
[202] W.W. Smeltzer, E.L. Tollefson, A. Cambron, Can. J. Chem. , 34 (1956) 1046-1060.
[203] J.Y. Park, Y. Zhang, M. Grass, T. Zhang, G.A. Somorjai, Nano Lett., 8 (2008) 673-677.
[204] S. Thanawala, D.G. Georgiev, R.J. Baird, G. Auner, Thin Solid Films, 515 (2007) 7059-7065.
[205] S. Hüfner, G.K. Wertheim, Phys. Rev. B, 11 (1975) 678-683.
[206] F.F. Huang, Y. Jin, L. Wen, D.B. Mu, M.M. Cui, J. Electrochem. Soc., 160 (2013) B184-B191.
[207] A.M. Cruz, L. Abad, N.M. Carretero, J. Moral-Vico, J. Fraxedas, P. Lozano, G. Subias, V. Padial, M. Carballo, J.E. Collazos-Castro, N. Casan-Pastor, J. Phys. Chem. C, 116 (2012) 5156-5169.
[208] R. Zanella, S. Giorgio, C.R. Henry, C. Louis, J. Phys. Chem. B, 106 (2002) 7634-7642.
[209] D. Andreeva, T. Tabakova, V. Idakiev, P. Christov, R. Giovanoli, Appl. Catal., A, 169 (1998) 9-14.
[210] M. Haruta, T. Kobayashi, H. Sano, N. Yamada, Chem. Lett., (1987) 405-408.
[211] D. Andreeva, V. Idakiev, T. Tabakova, A. Andreev, R. Giovanoli, Appl. Catal., A, 134 (1996) 275-283.
[212] H. Sakurai, M. Haruta, Appl. Catal., A, 127 (1995) 93-105.
[213] R. Zanella, C. Louis, S. Giorgio, R. Touroude, J Catal, 223 (2004) 328-339.
[214] P. Claus, A. Bruckner, C. Mohr, H. Hofmeister, J. Am. Chem. Soc., 122 (2000) 11430-11439.
[215] A. Ueda, M. Haruta, Gold Bull., 32 (1999) 3-+.
[216] T. Hayashi, K. Tanaka, M. Haruta, J Catal, 178 (1998) 566-575.
[217] S. Minico, S. Scire, C. Crisafulli, R. Maggiore, S. Galvagno, Appl. Catal., B, 28 (2000) 245-251.
[218] T.V. Choudhary, D.W. Goodman, Top. Catal., 21 (2002) 25-34.

[219] D. Andreeva, Gold Bull., 35 (2002) 82-88.
[220] P. Konova, A. Naydenov, C. Venkov, D. Mehandjiev, D. Andreeva, T. Tabakova, J. Mol. Catal. A: Chem. , 213 (2004) 235-240.
[221] M.M. Schubert, A. Venugopal, M.J. Kahlich, V. Plzak, R.J. Behm, J Catal, 222 (2004) 32-40.
[222] G.Y. Wang, H.L. Lian, W.X. Zhang, D.Z. Jiang, T.H. Wu, Kinet. Catal., 43 (2002) 433-442.
[223] B. Coq, F. Figueras, J. Mol. Catal. A: Chem. , 173 (2001) 117-134.
[224] H.B. Liu, U. Pal, J.A. Ascencio, J. Phys. Chem. C, 112 (2008) 19173-19177.
[225] M. Okumura, T. Akita, M. Haruta, X. Wang, O. Kajikawa, O. Okada, Appl. Catal., B, 41 (2003) 43-52.
[226] C.W. Huang, Y.J. Li, C. Muangphat, Y.W. Hao, Electrochim. Acta, 56 (2011) 8319-8324.
[227] C.R.K. Rao, D.C. Trivedi, Coord.Chem. Rev., 249 (2005) 613-631.
[228] G.C. Bond, C.T. Louis, D. T., Catalysis by gold, Imperial College Press ; Distributed by World Scientific, London; Singapore, 2006.
[229] A.M. Venezia, L.F. Liotta, G. Pantaleo, V. La Parola, G. Deganello, A. Beck, Z. Koppany, K. Frey, D. Horvath, L. Guczi, Appl. Catal., A, 251 (2003) 359-368.
[230] J.A. Rodriguez, D.W. Goodman, Science, 257 (1992) 897-903.
[231] B. Hammer, Y. Morikawa, J.K. Norskov, Phys. Rev. Lett., 76 (1996) 2141-2144.
[232] M. Kaack, D. Fick, Surf. Sci., 342 (1995) 111-118.

APPENDIX A – MASS AND HEAT TRANSFER CALCULATIONS FOR OXIDATION OF CO

Mass and Heat Transfer Calculations for Oxidation of CO on Ir/Al_2O_3

Mears Criterion for External Diffusion [196]

If $\frac{-r_A'\rho_b Rn}{k_c C_{Ab}} < 0.15$, then external mass transfer effects can be neglected.

$-r_A'$ = reaction rate, kmol/kg-cat · s

n = reaction order

R = catalyst particle radius, m

ρ_b = bulk density of catalyst bed, kg/m^3

ρ_c = solid catalyst density, kg/m^3

C_{Ab} = bulk gas concentration of A, $kmol/m^3$

k_c = mass transfer coefficient, m/s

$\frac{-r_A'\rho_b Rn}{k_c C_{Ab}}$ =[4.3 x 10^{-6} kmol-CO/kg-cat . s] [710 kg/m^3][0.7 x 10^{-6} m][1]/([1.92 m/s]*[0.0032 $kmol/m^3$])**=3.5x10^{-7} <0.15 {Mears for External Diffusion}**

Weisz-Prater Criterion for Internal Diffusion [195]

If $C_{WP} = \frac{-r'_{A(obs)}\,\rho_c R^2}{D_e C_{As}} < 1$, then internal mass transfer effects can be neglected.

$-r'_{A(obs)}$ = observed reaction rate, kmol/kg-cat · s

R = catalyst particle radius, m

ρ_c = solid catalyst density, kg/m^3; [$\rho_{c,\,alumina}$ = 3950 kg/m^3]

D_e = effective gas-phase diffusivity, m^2/s

$= \frac{D_{AB}\phi_p\sigma_c}{\tau}$ where

D_{AB} = gas-phase diffusivity m^2/s; ϕ_p = pellet porosity; σ_c =constriction factor; τ =tortuosity.

C_{As} = gas concentration of A at the catalyst surface, kmol-A/m^3

$C_{WP} = \frac{-r'_{A(obs)}\,\rho_c R^2}{D_e C_{As}}$ =[4.3 x 10^{-6} kmol-CO /kg-cat . s] × [3×10^5 kg-cat/m^3] × [0.7 x 10^{-6} m]^2 / ([4.87 x 10^{-6} m^2/s] × [0.0032 kmol-CO/m^3]) = **4.0 x 10^{-5} < 1**

{Weisz-Prater Criterion for Internal Diffusion}

Mears Criterion for External (Interphase) Heat Transfer [196]

$$\left|\frac{-\Delta H_r(-r_A')\rho_b RE}{h_t T_b{}^2 R_g}\right| < 0.15$$

[210.58 kJ/mol× 4.3 x 10^{-3} mol/kg-cat . s × 710 kg-cat/m^3 ×1.4 x 10^{-6} m× 103 kJ/mol] / [6.5 kJ/m^2.K.s × 448^2 K^2× 8.314 ×10^{-3} kJ/mol.K]=**$8.5x10^{-6} < 0.15$**

{Mears Criterion for External (Interphase) Heat Transfer}

Mears Criterion for Combined Interphase and Intraparticle Heat and Mass Transport [196]

$$\frac{-r'_A R^2}{C_{Ab} D_e} < \frac{1+0.33\gamma\chi}{|n-\gamma_b\beta_b|(1+0.33n\omega)}$$

$$\gamma = \frac{E}{R_g T_s};\ \gamma_b = \frac{E}{R_g T_b};\ \beta_b = \frac{(-\Delta H_r) D_e C_{Ab}}{\lambda T_b};\ \chi = \frac{(-\Delta H_r) - r'_A R}{h_t T_b};\ \omega = \frac{-r'_A R}{k_c C_{Ab}}$$

γ = Arrhenius number; β_b = heat generation function;

λ = catalyst thermal conductivity, W/m.K;

χ = Damköhler number for interphase heat transport

ω = Damköhler number for interphase mass transport

$\frac{-r'_A R^2}{C_{Ab} D_e}$ =[4.3x10^{-6} kmol/kg-cat.s× 710 kg-cat/m^3× (0.7x10^{-6})^2 m^2]/[0.0032 kmol/m^3×4.87x10^{-6} m^2/s]=**$9.5x10^{-8} < 3$**

{Mears Criterion for Interphase and Intraparticle Heat and Mass Transport }

Mass and Heat Transfer Calculations for Oxidation of CO on Ag-Ir/Al_2O_3 (0.2 wt% Ag)

Mears Criterion for External Diffusion [196]

If $\frac{-r_A' \rho_b Rn}{k_c C_{Ab}} < 0.15$, then external mass transfer effects can be neglected.

$-r_A'$ = reaction rate, kmol/kg-cat · s

n = reaction order

R = catalyst particle radius, m

ρ_b = bulk density of catalyst bed, kg/m^3

ρ_c = solid catalyst density, kg/m^3

C_{Ab} = bulk gas concentration of A, $kmol/m^3$

k_c = mass transfer coefficient, m/s

$\frac{-r_A' \rho_b Rn}{k_c C_{Ab}}$ =[6.4 x 10^{-6} kmol-CO/kg-cat . s] [710 kg/m^3][0.7 x 10^{-6} m][0.11]/([1.92 m/s]*[0.0032 $kmol/m^3$])**=5.7x10^{-8} <0.15 {Mears for External Diffusion}**

Weisz-Prater Criterion for Internal Diffusion [195]

If $C_{WP} = \frac{-r'_{A(obs)} \rho_c R^2}{D_e C_{As}} < 1$, then internal mass transfer effects can be neglected.

-r'$_{A(obs)}$ = observed reaction rate, kmol/kg-cat · s

R = catalyst particle radius, m

ρ_c = solid catalyst density, kg/m^3; [$\rho_{c,\ alumina}$ = 3950 kg/m^3]

D_e = effective gas-phase diffusivity, m^2/s

$$= \frac{D_{AB}\phi_p\sigma_c}{\tau} \text{ where}$$

D_{AB} = gas-phase diffusivity m^2/s; ϕ_p = pellet porosity; σ_c =constriction factor; τ =tortuosity.

C_{As} = gas concentration of A at the catalyst surface, kmol-A/m^3

$$C_{WP} = \frac{-r'_{A(obs)}\rho_c R^2}{D_e C_{As}}$$ =[6.4 x 10^{-6} kmol-CO /kg-cat . s] × [3×10^5 kg-cat/m^3] × [0.7 x 10^{-6} m]^2 / ([4.87 x 10^{-6} m^2/s] × [0.0032 kmol-CO/m^3]) = **6.0 x 10^{-5} < 1**

{Weisz-Prater Criterion for Internal Diffusion}

Mears Criterion for External (Interphase) Heat Transfer [196]

$$\left|\frac{-\Delta H_r(-r_A')\rho_b RE}{h_t T_b{}^2 R_g}\right| < 0.15$$

[210.58 kJ/mol× 6.4 x 10^{-3} mol/kg-cat . s × 710 kg-cat/m^3 ×1.4 x 10^{-6} m× 103 kJ/mol] / [6.5 kJ/m^2.K.s × 448^2 K^2× 8.314 ×10^{-3} kJ/mol.K]=**1.3x10^{-5} < 0.15**

{Mears Criterion for External (Interphase) Heat Transfer}

Mears Criterion for Combined Interphase and Intraparticle Heat and Mass Transport [196]

$$\frac{-r'_A R^2}{C_{Ab} D_e} < \frac{1+0.33\gamma\chi}{|n-\gamma_b\beta_b|(1+0.33n\omega)}$$

$$\gamma = \frac{E}{R_g T_s};\ \gamma_b = \frac{E}{R_g T_b};\ \beta_b = \frac{(-\Delta H_r) D_e C_{Ab}}{\lambda T_b};\ \chi = \frac{(-\Delta H_r) - r'_A R}{h_t T_b};\ \omega = \frac{-r'_A R}{k_c C_{Ab}}$$

γ = Arrhenius number; β_b = heat generation function;

λ = catalyst thermal conductivity, W/m.K;

χ = Damköhler number for interphase heat transport

ω = Damköhler number for interphase mass transport

$\frac{-r'_A R^2}{C_{Ab} D_e}$ =[6.4x10^{-6} kmol/kg-cat.s× 710 kg-cat/m^3× (0.7x10^{-6})^2 m^2]/[0.0032 kmol/m^3×4.87x10^{-6} m^2/s]**=1.4x10^{-7} < 3**

{Mears Criterion for Interphase and Intraparticle Heat and Mass Transport }

APPENDIX B – ELEY-RIDEAL (E-R) MECHANISM PREDICTION

The reactions for the Eley-Rideal (E-R) mechanism can be written as

$$A(g) + S(s) \leftrightarrow AS(s) \quad (1)$$

$$AS(s) + B(g) \rightarrow P(g) + S(s) \quad (2)$$

Assuming that $k_{-1} >> k_1$, we can apply a steady-state approximation to species AS:

$$\frac{d[AS]}{dt} = 0 = k_1[A][S] - k_{-1}[AS]_{ss} - k_2[AS]_{ss}[B] \quad (3)$$

As in the case of unimolecular catalyzed reactions, we can express the concentrations of AS and S in terms of a fraction of the total number of active sites, S_0 and rewrite the above equation as

$$0 = k_1[A](1-\theta)[S]_0 - k_{-1}\theta[S]_0 - k_2\theta[S]_0[B] \quad (4)$$

Solving for θ yields

$$\theta = \frac{k_1[A]}{k_1[A] + k_{-1} + k_2[B]} \quad (5)$$

Furthermore, if $k_2 << k_1$ and k_{-1}, we can simplify θ to

$$\theta = \frac{k_1[A]}{k_1[A] + k_{-1}} \qquad (6)$$

The rate of production of P can be expressed as

$$\frac{d[P]}{dt} = k_2[AS]_{ss}[B] = k_2\theta[S]_0[B] \ = \frac{k_1 k_2[A][S]_0[B]}{k_1[A] + k_{-1}} \qquad (7)$$

We can also write the above expression in terms of the equilibrium constant, K, which is equal to k_1/ k_{-1}

$$\frac{d[P]}{dt} = \frac{Kk_2[A][S]_0[B]}{K[A] + 1} \qquad (8)$$

Based on the E-R formalism, the kinetic parameters for CO_2 formation over monometallic Ir can be expressed by equations 9-10, where oxygen adsorbs onto the catalytic surface and then it reacts with CO molecules in the gas phase.

$$r_{CO_2} = k_2\theta_{O(Ir)}[S]_0 P_{CO} \qquad (9)$$

$$\theta_{O(Ir)} = \frac{(K_{O_2}P_{O_2})^{0.5}}{1 + (K_{O_2}P_{O_2})^{0.5}} \qquad where\ K = \frac{k_{ads}}{k_{des}} \quad (10)$$

After substitution of equations (10) into equation (9), equation (11) is obtained.

$$\therefore r_{CO_2} = \frac{k_2 (K_{O_2}P_{O_2})^{0.5}}{1 + (K_{O_2}P_{O_2})^{0.5}}[S]_0 P_{CO}$$

$$= k' P_{O_2}{}^{y} P_{CO}{}^{1} \quad where\ 0 \leq y \leq 0.5 \qquad (11)$$

This analysis implies that if the Eley Rideal mechanism is occurring, the reaction rate should be first order in CO and y order in O_2, where y is larger than 0 and smaller than 0.5 as shown in Equation (11). This is inconsistent with the kinetic results shown in Figure 6.

For the case of the Ag-Ir bimetallic catalysts, the coverage of atomic O on the both metals must be considered; thus, the overall reaction rate of CO_2 formation may involve several surface reactions which can be written as follows:

$$r_{CO_2} = k_2[\theta_{O(Ir)}][S]_0 P_{CO} + k'_2[\theta_{O(Ag)}][S]_0 P_{CO} \qquad (12)$$

$$\theta_{O(Ag)} = \frac{(K'_{O_2} P_{O_2})^{0.5}}{1 + (K'_{O_2} P_{O_2})^{0.5}} \qquad (13)$$

By substituting equations (10) and (13) into Equation (12), equation (14) is obtained.

$$r_{CO_2} = \left\{ k_2 \left[\frac{(K_{O_2} P_{O_2})^{0.5}}{1 + (K_{O_2} P_{O_2})^{0.5}} \right] + k'_2 \left[\frac{(K'_{O_2} P_{O_2})^{0.5}}{1 + (K'_{O_2} P_{O_2})^{0.5}} \right] \right\} [S]_0 P_{CO} \qquad (14)$$

This analysis again predicts that the reaction rate is first order in CO and y order in O_2, where y is larger than 0 and smaller than 0.5, which is inconsistent with our kinetic results. Therefore, it is concluded that the observed kinetic results do not followed the E-R mechanism.